NUMERICAL MODELING OF SUCTION CAISSONS IN DENSE SAND FOR GENERAL CONDITIONS OF DRAINAGE

A Thesis

by

RAGINI GOGOI

Submitted to the Office of Graduate and Professional Studies of
Texas A&M University
in partial fulfillment of the requirements for the degree of

MASTER OF SCIENCE

Chair of Committee,	Charles Aubeny
Committee Members,	Zenon Medina-Cetina
	Alan Palazzolo
Head of Department,	Robin Autenrieth

May 2020

Major Subject: Civil Engineering

ABSTRACT

Suction caissons have been widely used in the offshore oil and gas industry for over 30 years, but to date have not being extensively used for offshore renewables. They represent a viable solution for the foundations of offshore windfarms, which are gaining momentum as an alternate energy source worldwide. Due to the complex interactions with saturated soils, the behavior of a suction caisson for an offshore wind farm installed in dense sand is currently under vigorous numerical and experimental investigation.

This study concentrates on using finite element analysis to simulate the behavior of the trailing suction caisson in a multi-bucket jacket in dense sands subjected to monotonic tensile loading. A two-dimensional, axisymmetric hydro-mechanical numerical model is developed to explore the effect of different drainage conditions on the vertical resistance. The suction pressure developed in response to different tensile loading speeds is also examined.

For verification of the model, the outputs of the numerical analysis are validated against simple-hand calculations and findings of previous studies. Testing conditions adopted in Centrifuge tests by Senders and Bienne have been recreated for a comparative and parametric study. A complex soil model developed by Whyte is also studied along with Wolfersdorff's hypoplastic model and the ABAQUS in-built soil model – Mohr Coulomb, in order to determine the most efficient soil failure model to capture the complex undrained behavior of dense sand.

ACKNOWLEDGEMENTS

The work presented in this thesis is the result of my close association with many people during my tenure as a student at Texas A&M University. I would like to take this opportunity to extend my gratitude and appreciation to all those who made this thesis possible.

First and foremost, I would like to extend my sincere gratitude to my advisor Dr. Aubeny for introducing me to this field of study. I have learnt extensively from him and am grateful for his dedicated help, advice and encouragement throughout these two years.

I would also like to thank Dr. Phillip Watson, from the University of Western Australia for agreeing to be a part of my thesis committee as a Special Appointment. He has always evinced a keen interest in my work and I am grateful for his continuing guidance. I am thankful to him and Dr. Fraser Bransby for supervising my work while at the University of Western Australia and for creating a supportive working environment.

My sincere thanks also go to my other committee members, Dr. Medina and Dr. Palazzolo, for their patience, guidance and for kindly agreeing to be a part of my committee.

Also, a warm note of gratitude to my fellow graduate students in the department. I believe to have benefitted immensely from working in close association with them. Finally, I wish to thank my parents, and my sister, for their constant encouragement and support throughout my time in Texas.

CONTRIBUTORS AND FUNDING SOURCES

Contributors

This work was supervised by a thesis committee consisting of Professor Charles Aubeny of the Department of Civil Engineering, and Dr. Phillip Watson from the University of Western Australia; and Dr. Zenon Medina-Cetina of the Department of Civil Engineering and Dr. Alan Palazzolo of the Department of Mechanical Engineering.

All work conducted for the thesis was completed by the student independently.

Funding Sources

Graduate study was partially supported by a fellowship from Texas A&M University and an assistantship under Professor Charles Aubeny.

This work was also made possible by an internship in the Center for Offshore Foundation Systems at UWA, sponsored by Woodside, Perth.

The contents of this work are solely the responsibility of the author and do not necessarily represent the official views of the sponsors.

NOMENCLATURE

CHAPTER 2: Theory and Background

σ'	Effective normal stress
σ	Normal stress
u	Pore water pressure
γ_w	Unit weight of water
d	Depth below ground level
T	Time factor
k	Coefficient of permeability
E	Young's Modulus of elasticity
τ_f	Shear stress at failure
c'	Cohesion
σ'_{nf}	Normal stress at failure
φ'	Effective friction angle
σ'_1	Major principle stress
σ'_3	Minor principle stress
V'	Vertical uplift capacity
γ'	Effective unit weight
Z_0	Caisson skirt length
h	Depth of penetration
K	Coefficient of earth pressure at rest
δ	Interface friction angle
D_o	Outer caisson diameter
D_i	Inner caisson diameter
s	Suction
A	Cross-sectional area of top-cap

CHAPTER 3: Finite Element Modelling

τ_{crit}	Critical shear stress
μ	Coefficient of friction
p	Effective normal pressure

φ_{in}	Interface friction angle
δ	Delta
φ	Friction angle
c	Cohesion
ρ	Bulk density
γ	Unit weight
g	Acceleration due to gravity
E	Young's modulus of Elasticity
I_r	Rigidity index
υ	Poisson's ratio
σ_v	Vertical stress
D_r	Relative density
σ'_c	Effective confining stress
φ_{rel}	Relative friction angle
k_{K-C}	Kozney-Carmen coefficient of permeability
e	Void ratio
C_{K-C}	Kozney-Carmen empirical constant
S_0	Specific surface area per unit volume
φ'_{max}	Peak effective friction angle
φ'_{crit}	Critical state effective friction angle
ψ_{max}	Peak dilation angle
p_s'	Effective mean stress
k_0	Coefficient of earth pressure at rest
D	Mean particle diameter
K	Bulk Modulus
h_s	Granular hardness
e_{do}	Minimum void ratio at zero pressure
e_{co}	Critical void ratio at zero pressure
e_{io}	Maximum void ratio at zero pressure
n	Hypoplasticity soil model exponential parameter
α	Hypoplasticity soil model exponential parameter
β	Hypoplasticity soil model exponential parameter

CHAPTER 4: Results

U_y	Vertical displacement

V	Vertical capacity
T	Normalised time factor
c_v	Coefficient of consolidation
t	Loading time
D	Drainage path
k	Coefficient of consolidation
E	Young's modulus of elasticity
ϑ	Poisson's ratio
γ_w	Unit weight of water
A	Cross-sectional area of caisson top cap

TABLE OF CONTENTS

Page

LIST OF FIGURES

Page

LIST OF TABLES

Page

1. INTRODUCTION

1.1. Overview

In the current context of global warming and rapid depletion of traditional resources, research in renewable energy sources is fast becoming the overarching need of the hour. Renewable energy sources provide electricity without giving rise to carbon dioxide emissions. Out of the different forms of renewable energy available, wind energy has proven to be the most promising. [Senders, 2008] However, densely populated countries are unable to set up the huge wind farms which are needed to produce such clean energy on a competitive scale. Thus, the need arises for offshore renewables.

1.2. Offshore wind farms

Offshore wind farms are a means to harvest wind energy by constructing wind turbines in bodies of water, usually in the ocean or on the continental shelves. They offer the benefit of more sustained and stronger winds at lower heights over the onshore kind. [Saavedra, 2017] Moreover, offshore wind has huge potential in many regions, as the world looks for competitive, zero carbon energy sources that can be deployed at scale and in relatively fast time frames. Their construction requires less than 2.5% of the energy they produce in their lifetime, making them one of the cleanest forms of energy generating technologies available today. [Senders, 2008] Thus, offshore wind as a form of renewable energy provides a sustainable solution to the increasing demand for energy worldwide.

Recent years have seen a sudden rise in the construction and development of offshore wind farms worldwide, and it is expected that this trend will continue. The offshore market will become a truly global market over the next five years. The Global Wind Report

predicts this market to rise by 2.7% each year. In North America, this growth can be particularly seen in the north-eastern states. Currently, 8% of the new wind farm installations are offshore, and by 2023, this share is expected to increase to 22%. [Global Wind Report, 2018]

1.2.1. **Offshore load conditions**

An offshore structure must be designed to sustain the loads imposed by nature in such extreme environmental conditions. Over the design life of the turbine, it is exposed to over a hundred million loading cycles from various sources. [Green, 2019] The main sources of these loads are the waves and currents acting on the foundation underwater and the wind drag on the turbine. In addition, the foundation must also be able to withstand the self-weight of the turbine, tower and the supporting structure.

The foundation is acted on by a wave profile in the form of hydrodynamic drag. Its magnitude depends on the wave height and the wave period, and acts in a horizontal variable direction. [Senders, 2008] The hydrodynamic drag can be quantified by site-specific wave measurement or hydraulic numerical modelling. [Green, 2019]

Considerable aerodynamic drag, due to the forces of wind, acts on the tower owing to its tall structure. The unevenly distributed horizontal load causes random turbulence on the structure. This random turbulence, when transferred to the rotating blades, causes a vibration in the frequencies of 1P and 3P. 1P is the frequency generated as the first blade undergoes the turbulence and 3P is the frequency of each successive blade subjected to the same turbulence. The supporting structure must be designed to ensure its natural

frequency doesn't overlap with the 1P and 3P frequencies, to avoid complete structural failure due to resonant response. [Temple, 2002]

The self-weight of an Offshore Wind Turbine (OWT) consists of the weight of the blades, the nacelle, the tower, the supporting structure and the foundation. They act in the vertically downward direction and contribute to the resistance to the overturning moment generated due to the hydrodynamic and aerodynamic drags on the structure.

The environmental loading conditions considered and tested for in the current thesis are further described in Section 4.2.1 and Section 4.4.

1.2.2. **Types of offshore foundations**

The foundation of an OWT is designed to withstand all the loads acting on the structure. There are currently various options available for the type of foundation for an offshore structure, depending on the soil conditions, water depth and the type of superstructure.

The most commonly used type of offshore foundations are pile foundations. Currently, more than 82% of all global offshore wind turbines are supported by monopiles. [Andersen, 2016] These are steel piles with large diameters (4m to 6m) installed in waters up to 40m deep. [Senders, 2008] They are driven into the subsurface with the use of a large and expensive hammer, barge or a jack-up rig. Such installations generate extremely loud vibrations, negatively impacting the local marine life. [Andersen, 2016] This poses as a major drawback for pile foundations for offshore structures.

A favourable alternative is the use of suction caissons. Suction caissons are hollow, opened ended pile foundations, installed in the sea bed partially by its own self-weight

and partially by the creation of a suction between the top cap and the soil surface. The lack of requirement for a hammer in their installation process leads to a considerably less disturbance to marine life. They are employed either as single caissons (mono-pods) or as a group of multiple caissons (multi-pods). Multi-pod systems are preferred in deeper waters since the diameter for a mono-pod will have to be uneconomically high to sustain the moments generated at greater water depths. This type of foundation is cheaper, in terms of the amount of steel used with respect to conventional pile foundations. This creates a more competitive price for offshore wind energy in comparison with other renewable energy sources. Thus, the current thesis focuses solely on the application of suction caissons as part of a tripod-jacked system to support offshore wind turbines (OWT).

1.3. Suction Caissons

Suction caissons are large cylindrical steel foundations, resembling the geometry of an inverted bucket, closed at the top and open at the base. They are designed with relatively thin walls, with diameter to wall thickness ratio of 125-160, and length to diameter ratio of less than 1.5 for dense sands. [Aubeny, 2018] They are well-suited for a range of soil profiles, including complex dense sands, along with stiff and soft clays.

A key motivation behind their utilization is their relatively simple installation process. Their penetration into the seabed occurs partially due to their self-weight and partially due to the application of a differential pressure (suction) across the foundation top-cap which is achieved by pumping out water via a valve present on it. Their installation in clays is dictated by the amount of underpressure required to overcome the soil resistance, while in their installations in sands, additional consideration is required for the

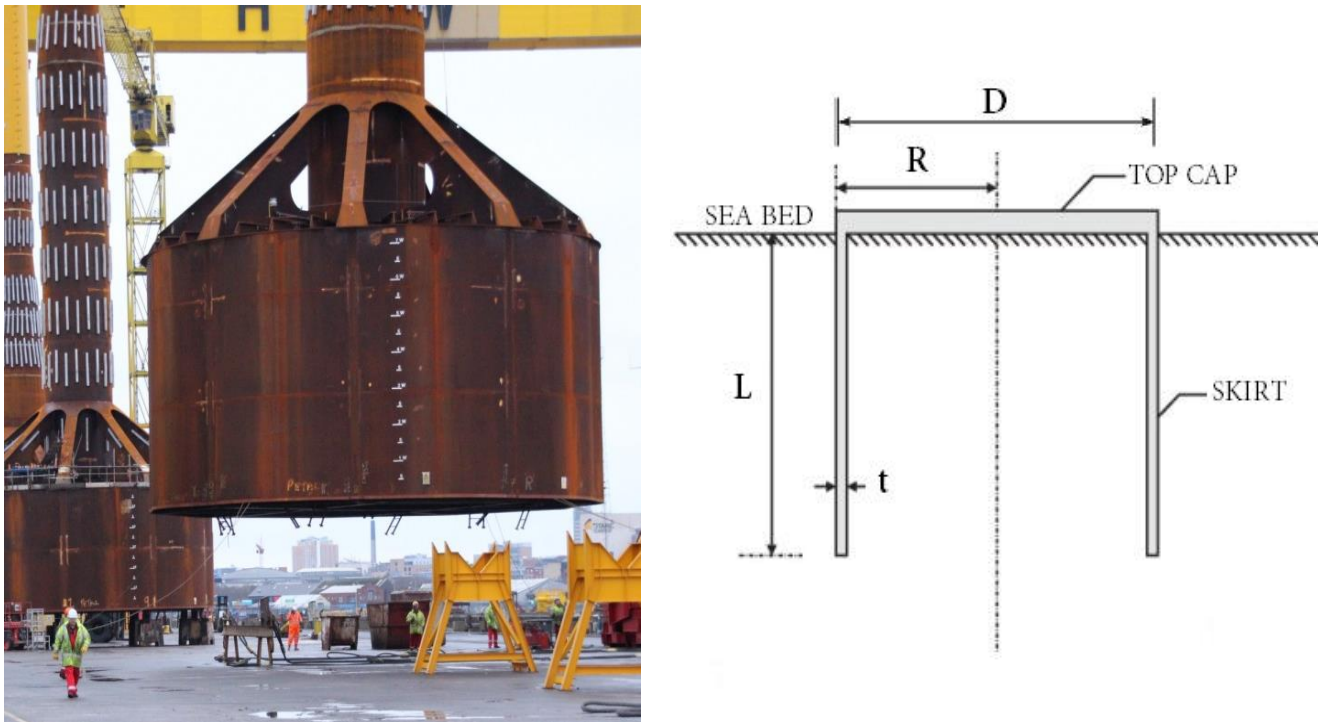

Figure 1-1 a) Mono-suction caisson. Reprinted from [Universal Foundation] b) 2D geometry of a suction caisson

upward seepage flow instigated inside the caisson by the underpressure, which reduces the penetration resistance of the soil dramatically. [Aubeny, 2018]

Suction caissons can be designed to resist the large overturning moments acting on the OWT due to the significant horizontal forces on it, which result in a push-pull resistance mechanism in the foundation system. This mechanism, in severe storm conditions, causes failure due to significant decrease in the upward vertical force of the bucket, or the trailing bucket in multi-pod systems. Thus, for an OWT to be successful, accurate standards for their tensile capacity under severe pull-out conditions must be known.

Hence, the focus of the current thesis project is to develop a finite element model to simulate the behavior of an OWT under various loading rates, in dense sands.

1.4. Problem statement

The primary goal of this thesis is to investigate the performance of a suction caisson as a viable option to support offshore wind farms in dense sand, with a focus on UWA Superfine Silica Sand. The behavior of the caisson is analyzed under different offshore environmental loading conditions an offshore wind turbine is subjected to during its operational lifespan.

A typical offshore wind turbine will be exposed to horizontal loads due to the motion of the ocean waves and the wind, with a greater contribution from the aerodynamic loads due to the large height of the structures. The resulting overturning moment must be resisted by the vertical loads on the individual caissons of a multipod foundation system, which develop a push-pull mechanism – caissons in the leeward side develop a compressive axial force whereas the caissons on the windward side develop a tensile axial force. Under extreme offshore storm conditions, the overturning moment is significantly large, though only for a short duration of time with a long return period. This results in the development of a net tension in the windward caisson, which dominates the foundation design. Thus, the critical loading of each caisson requires the consideration of only the tensile loading condition or the uplift.

A numerical study is carried out to simulate this response of the trailing suction caisson in a tripod jacket system subjected to a monotonic, purely vertical pull-out under a range of drainage conditions. The different drainage conditions, expressed as a function

of the loading rate, are used to represent the different offshore loading conditions, which in turn are dependent on the permeability of the soil and the time period of the loading.

An axisymmetric finite element (FE) model has been developed to predict the pore-pressure and load-displacement behavior of the single suction caisson, using the numerical formulation available in the software package ABAQUS-6.12.1. The thesis is categorized into two phases. The first phase adopts the built-in elastic-perfectly plastic soil failure model, Mohr-Coulomb to achieve the objectives set forth. The second phase, in an attempt to better capture the dilation behavior of dense sand, employs a non-linear hypoplastic material law as presented in the form by von Wolfersdorff [Wolfersdorff, 1996]. This soil model was implemented in ABAQUS via a material subroutine written in FORTRAN.

The current study tests three different soil types – a generic medium-dense sand, UWA Super-fine Silica Sand and the IGtH dense sand, with a specific focus on the UWA Superfine Silica Sand. Their behavior, in terms of drainage conditions, depends on the combination of geometry and pull-out rate of the bucket, and the permeability of the soil. Thus, in order to explore a wide range of drainage conditions, the analysis is performed at different pull-out rates – rapid pull-out for an undrained condition (or an extreme storm condition) and slow pull-out for a drained condition (or a normal offshore environmental state) on different caisson geometries.

The applicability of this study is validated by comparing obtained results against published data. Centrifuge tests conducted at the University of Western Australia by Bienne [Bienen, 2018] and Senders [Senders, 2008], are used as the primary tool for comparison. The current FE model is also assessed against the predictions by a numerical

study by Whyte [Whyte], using a complex bounding surface soil failure model. Thus, three different soil failure models were compared to determine an efficient method of predicting the tensile behavior of a suction caisson supporting an OWT in dense sand.

The objectives, thus set forth for this thesis are:

1. To develop a hydro-mechanical FE model to simulate the monotonic pull-out response of the trailing suction caisson in a multi-bucket jacket wished in place in dense sand.
2. To investigate soil response under different offshore environmental loading conditions, represented in terms of the drainage condition of the soil; and to define a transition curve of the ultimate capacity from a fully undrained to a fully drained condition.
3. To validate the FE model by comparing predicted results against available centrifuge test results; and to recommend an efficient soil failure model capable of capturing the tensile behavior of the caisson under different environmental conditions.
4. To analyze the capability of a suction caisson to successfully support an OWT, under operational conditions.

1.5. Outline of thesis

The thesis has been categorized into five chapters. A brief outline of each is provided below:

Chapter 2: Theory and Background

This chapter presents the theoretical background relevant to this thesis. It's first section describes the typical response of dense sand under different loading conditions, and brief introductions on the three different types of soils analyzed: generic medium-dense sand, UWA Superfine Silica Sand and dense IGtH sand. It also contains a section on the constitutive modeling of soil, with descriptions of the three models studied, along with the methods to determine the model parameters. The three soil constitutive models are Mohr Coulomb soil model, Hypoplastic soil failure model and a bounding surface sand model proposed by Whyte. A few relevant previous works – numerical studies as well as experimental tests – have been described, along with the methodologies used and the outcomes achieved.

Chapter 3: Finite Element Model

This chapter focuses on the finite element model developed for the current thesis. The model was developed using the numerical formulation available in ABAQUS, and contains all the required inputs for it. A section contains a description of the mesh developed and the definition of the different loading conditions it is subjected to. Another section contains the soil properties and the model parameter values adopted for the study, and their justification. The final section in this chapter describes the single element test done using the Hypoplastic soil model and the Mohr Coulomb soil model on Hochstetten sand, with its outcome compared to similar tests conducted by Wolfersdorff.

Chapter 4: Results

This section describes the predictions by the FE model developed and described in the previous chapter. The chapter is subdivided into four sections. The first section

(Section 4.1) adopts the Mohr Coulomb soil failure model, and is tested on the generic medium dense sand (Section 4.1.1) and UWA Superfine Silica Sand (Section 4.1.2). It also contains various model verification tests conducted for the tests on the generic medium dense sand; while the predictions for UWA Superfine Silica Sand are compared with similar previously conducted studies. The second section (Section 4.2) of this chapter employs the Hypoplasticity soil failure model and is tested first on the dense IGtH sand, and then on UWA Superfine Silica Sand. The outcomes from the tests conducted on the dense IGtH sand are compared with similar numerical studies conducted by Thieken [Thieken, 2014]. The predictions for UWA Superfine Silica Sand are compared with the same studies used for the comparison in the previous section. The third section, Section 4.3, is a comparative study between the three soil failure models – Mohr Coulomb, Hypoplastic model and Whyte's bounding surface sand model. The final section (Section 4.4) presents the outcomes of the current thesis in terms of the practical relevance for an OWT. The loading conditions and the displacements studied are limited by the operational allowances. This section also contains a justification of the viability of a suction caisson foundation system to support an offshore wind farm.

Chapter 5: Conclusion

This chapter summarizes the work presented in this thesis, and provides a list of the conclusions drawn.

2. THEORY AND BACKGROUND

2.1. Soil Behavior

2.1.1. Soil Mechanics

Soil mechanics deals with the study of soil properties and soil behavior. Soil is considered to be a multi-phase media, with the soil-skeleton, water and gas particles all governed by their own physical laws. This leads to the formulation of a complex interactive nature.

The understanding of the transfer of stresses within the continuum and the resulting strains play a crucial role in characterizing soil behavior. The effective stress principle [Terzaghi, 1925] states that the stresses transmitted through the soil skeleton, at the points of contact of the grains, are the ones responsible for the deformation of the soil, and in turn controls the strength of the soil. It can be defined as the normal stress undertaken by the soil skeleton [Briaud, 2013] and is formulated as the difference between the total stress and the pore water pressure of the soil.

$$\sigma' = \sigma - \eta \cdot u$$

where, η depends on the compressibility of the soil; generally taken as unity. [Lade, 2005]

The pore water pressure is the pressure of the water held within the voids of the soil skeleton, and is a function of the water depth and unit weight, and the hydraulic boundary conditions. [Ridley] In the absence of flow, [Wood, 2004] it is given by:

$$u = \gamma_w \cdot d$$

where d is the depth below the water level. This water pressure, when subjected to only the forces of gravity, is present below the water table and considered to be in compression (represented as positive pore pressure). [Briaud, 2013, Ridley] When subjected to other forces, such as various molecular, chemical-physical forces, acting at the soil-water boundary, the pore water is drawn above the water table and considered to be in tension (represented as negative pore pressure). This negative pore water pressure is also called soil suction, [Ridley] and is formally defined as the potential water has to achieve a certain water tension. [Briaud, 2013]

2.1.2. **Drained vs. undrained behavior**

When a saturated soil mass is subjected to loading, the increase in stress is taken up directly by the pore water, due to the incompressible nature of water compared to the soil-skeleton. The applied stress is then gradually transferred to the soil skeleton, decreasing the excess pore water pressure generated. The rate of pore water dissipation is governed by the coefficient of consolidation of the soil. [Aubeny, 2018] This concept is explained by Terzaghi's 1D Consolidation Theory.

When the pore water pressure is allowed to dissipate, accompanied by a change in the volume of the soil mass, it is a drained analysis. The rate of loading is very slow relative to the rate of dissipation of the pore water pressure for such an analysis, causing an insignificant amount of pore water pressure to be generated, and is termed as drained loading. When a significant excess pore water pressure is generated and is not allowed to dissipate, but held entrapped in the soil voids, an undrained condition arises. [Helwany, 2007] Such a case occurs when the rate of loading exceeds the rate of pore water pressure

dissipation to a sufficient degree. [Aubeny, 2018] No change in the volume of the soil mass is observed in such a case and the soil expansion must be balanced by the contraction.

Coarse grained soils (such as sand and gravel) experience faster rates of dissipation of the excess pore water pressure due to their higher permeability compared to finer grained soils (silt and clay) and generally exhibit drained loading. But it is incorrect to adopt this as a universal law. This was observed in 1995, when a 'monster wave' hit the Draupner E platform in the North Sea. Though installed in sand, the pore pressure dissipation during the rogue wave (with a wave period of 11.2seconds) was very low, indicating the adoption of a partial drainage instead of a full undrained analysis at best. [Vaitkunaite, 2016]

For most practical cases, if the degree of consolidation, U exceeds 70% or the time factor, T given by:

$$T = \frac{kE_{oed}}{\gamma_w d^2} t$$

is more than 0.4, a drained analysis might be adopted and an undrained analysis for U<10% or T<0.1. [Lees, 2016]

Compressive loading conditions generate positive excess pore pressure, the dissipation of which leads to an increase in the shearing resistance of the soil. Thus, as the soil transitions from an undrained condition to a drained condition, the soil strength will increase whereas tensile loading conditions lead to the creation of suction pressure (or negative pore water pressure), and its dissipation with increase in drainage causes a decrease in the soil strength. [Aubeny, 2018] Fig 4.28 represents a transition curve for the uplift capacity of a caisson as the soil progresses from a completely undrained state to a

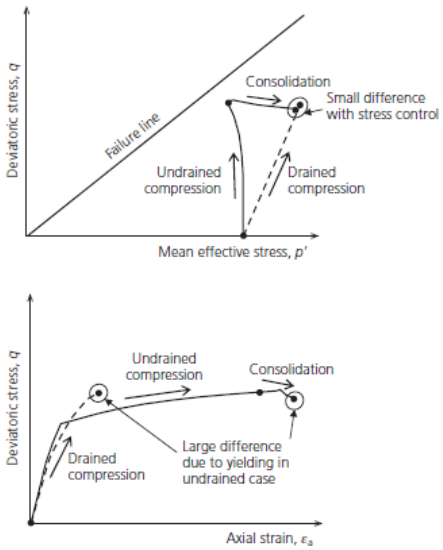

Figure 2-1 Stress path for low-permeability soil. Reprinted from [Lees, 2016]

completely drained state. This illustrates the reduction in the soil strength over time as drainage occurs for a tensile loading condition.

Fig 2.1 represents the behavior of a fine-grained soil (clay) under drained and undrained compressive loading. It can be observed from the figure that the shear strength of the soil in the drained compression case is much higher than the undrained case. The soil behavior of coarse-grained soil (sand) is described in detail in the following section.

2.1.3. **Sand Behavior**

Shearing response in sand tends to differ with its density. Fig 2.2 (a) exhibits a loosely packed sand undergoing shearing. The sand particles are represented by two dimensional circular discs. When sheared, the particles tend to slide over each other and occupy the significant amount of void space available between them. This leads to a reduction in the soil volume. Triaxial test results in Fig 2.3 (b) [Andersen,2013] represents this concept in the form of a volumetric strain vs axial strain plot. For both drained and undrained responses, loose sand will undergo contraction as shearing continues. The corresponding

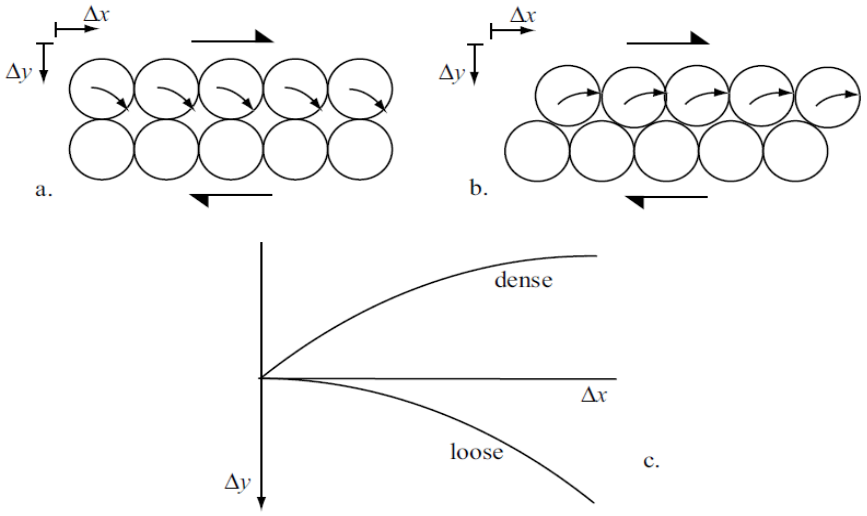

Figure 2-2 a) Shearing of initially loose sand b) Shearing of initially dense sand c) Volumetric response of dense and loose sand. Reprinted from [Wood, 2004]

shearing resistance will increase monotonically to an ultimate value representing failure, as represented in Fig. 2.3 (a and d). [Aubeny, 2018] The initial response of the stress path however, differs for a drained and undrained case. (Fig 2.3. c and f) For a drained condition, the stress path attained is a straight line, whereas for an undrained condition, the stress path initially bends to the left, indicating contracting behavior, which manifests itself in positive pore water pressure. (Fig 2.3 e) [Wood, 2004]

The response of dense sand undergoing shearing is illustrated in two-dimensional form in Fig 2.2 (b). As they are sheared, due to the unavailability of void space between them, the particles climb over each other, expanding the volume occupied by the soil. The volumetric response with respect to shearing plot in Fig 2.3 (b) shows this trend. Though the initial soil response is of contraction, as shearing progresses the soil tends to exhibit expansive behavior till the critical state condition is reached. This tendency to increase in volume is dilatancy. [Wood, 2004] In undrained analysis, this expansion in volume is

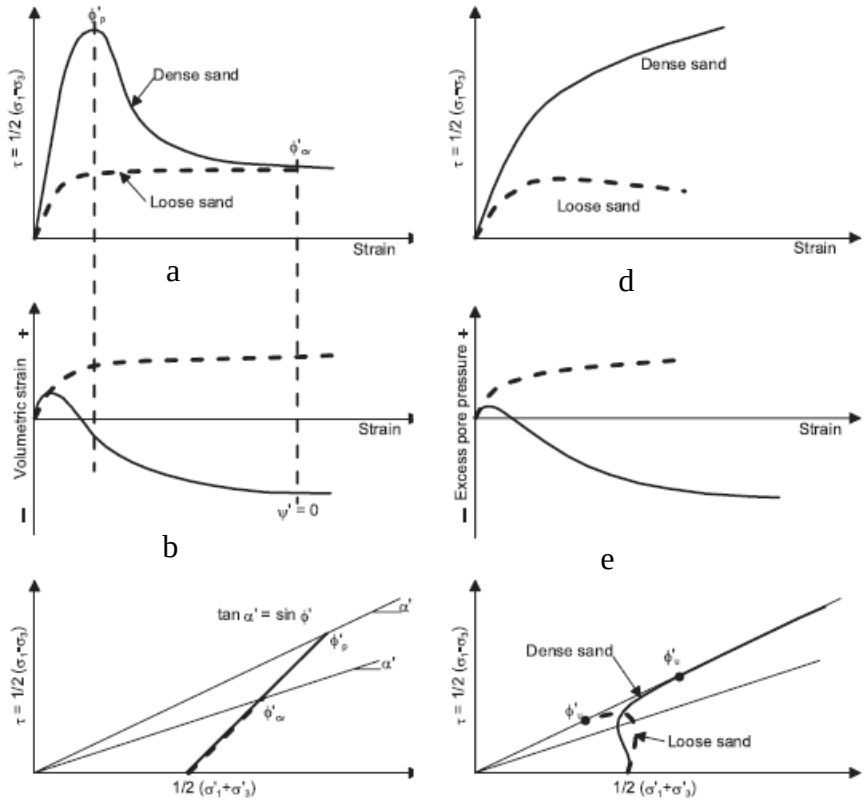

Figure 2-3 Drained and undrained response of sand. Reprinted from [Andersen, 2013]

accompanied by a decrease in pore water pressure. This decrease will increase the effective stress and therefore the resistance against failure. [Breusers, 1974] This is captured in the stress-strain curve, Fig. 2.3 (d), where the deviatoric stress continues to rise, with no ultimate value attained, as opposed to the drained curve (Fig. 2.3 (a)), where the deviatoric stress achieves a peak value at low strains and then continues to soften, till the critical state condition is reached. The undrained stress path for dense sand further illustrates this trend, where after an initial contractive behavior, follows a dilative tendency represented by a right turn in the path. (Fig. 2.3 (f)).

2.1.4. **Types of sand studied**

The thesis uses three different types of sand – a generic medium dense sand, University of Western Australia (UWA) Superfine Silica Sand and IGtH sand.

2.1.4.1. UWA Superfine Silica Sand

UWA Superfine Silica Sand is a poorly graded (SP), sub-rounded to sub-angular soil type. It has a mean size, $d_{50,}$ of 0.17mm with a specific gravity of 2.67. The maximum and minimum dry densities are 1497 kg/cm^3 and 1774 kg/cm^3 respectively. [Chow, 2019] This particular soil type is also considered to be a broad representative of North Sea sands, which are a prime location for the installation of OWT. [Whyte]

2.1.4.2. IGtH Sand

IGtH sand refers to the Leibniz University of Hannover's Institute for Geotechnical Engineering's sand. IGtH sand is a narrowly graded, medium-grain, rounded quartz sand. [tom Wörden, 2010]. Its 50% sieve passing diameter, d_{50} is 0.52mm and coefficient of curvature, C_c, 0.9. The soil studied in the current study had a soil density of 2.63 g/cm^3, with minimum and maximum void ratios of 0.499 and 0.789, respectively.

2.2. Constitutive Modelling

Constitutive models are mathematical equations that provide a relationship between stress and strain. They are formulated on the basis of principles of mechanics, theoretical principles and experimental evidence. [Lade, 2005] A successful soil constitutive model should be capable of reproducing the important stress-strain behavioral aspects of the soil under all loading conditions. A bonus feature of such models is the easy determination, and a low number of the required parameters.

Three soil constitutive models are described in the following sections. The Mohr Coulomb failure model is a popular model due to its simplicity and requirement of only 5, easily derivable parameters. The second model is a rate dependent Hypoplastic model, in the form presented by Wolf, whose eight required parameters are related to the granulometric properties of the grain assemblies. [Herle, 1999]. The final model is a bounding surface plasticity model developed by Whyte [Whyte], based on the Manzari-Dafalias model architecture with 19 parameters.

2.2.1. **Mohr Coulomb Failure model**

The Mohr-Coulomb failure criteria is a classical pressure dependent soil failure model, widely accepted due to its mathematical simplicity and clear physical meaning of its parameters. It is based on the assumption that macroscopic plastic yielding occurs because of frictional sliding between the material particles. [Neto, 2008] According to this law, a critical combination of the normal stress and the shear stress on a plane in a body marks the onset of yielding. This relationship, between the normal and shear stresses on a failure plane, is approximated to be linear and can be expressed as: [Coulomb, 1776]

$$\tau_f = c' + \sigma'_{nf} \tan(\varphi') \qquad \text{Eq. 2.1}$$

where the shear stress at failure, τ_f, for cohesionless ($c' = 0$) soil such as dense sand, becomes a function of the normal stress at failure, σ'_{nf}, and the peak friction angle, φ', only. Fig. 2.4 presents an idealized geometrical depiction of the failure envelope, described by Equation 2.1, which serves as a boundary in stress space for elastic behavior. If the soil reaches yield, the stresses have to lie on this line, that is, all plastic stresses are

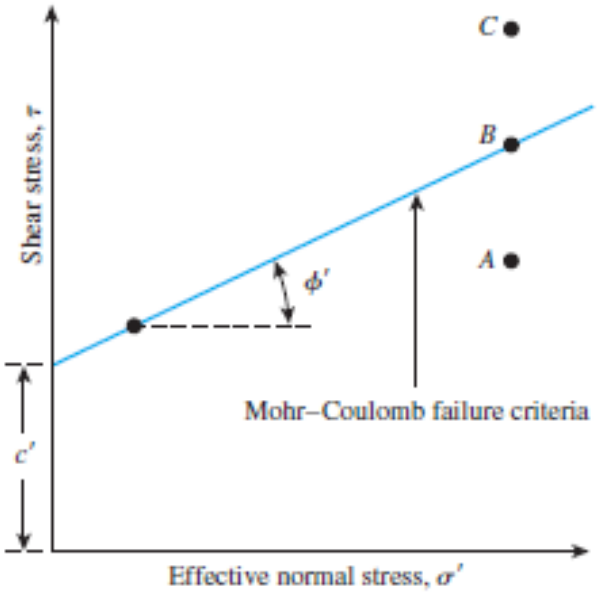

Figure 2-4 Mohr Coulomb failure envelope. Reprinted from [Das, 1997]

confined to this fixed failure envelop. [Wood, 2004] This depicts the elasto-perfectly plastic nature of the Mohr Coulomb failure model.

The yield criteria of the model can thus be presented as a function of the current stress state, by rewriting Equation 2.1 in terms of the principle stresses, as: [Potts, 1999]

$$F(\{\sigma'\},\{k\}) = \sigma'_1 - \sigma'_3 - 2c'\cos(\varphi') - (\sigma'_1 + \sigma'_3)\sin(\varphi')$$

where k represents the model state parameters, described in Section 2.2.1.1.

The post yield deformation in the model is governed by a non-associative flow rule. The flow rule provides a mechanism to describe the plastic deformation response of the soil, by depicting the direction of the plastic strain increment vector in respect to the plastic yield surface, when superimposed in stress space. [Lade, 2005] This direction is determined from the derivative of the plastic potential function. In the case of an associated flow rule, the plastic strain increment is assumed to be normal to the yield surface, making the plastic potential function equal to the yield function. Though mathematically

convenient, such an assumption fails to capture the real soil response of frictional material such as dense sand.

Fig. 2.5 shows the plastic strain increment vector produced normal to the yield surface, indicating negative plastic strains (dilation). This demonstrates that the linear nature of the Mohr Coulomb yield surface will always produce a dilatant plastic strain increment, under the normality condition. The magnitude of the plastic dilation is controlled by the angle of dilation, which is equal to the internal friction angle for an associative flow rule ($\varphi' = \psi$). For frictional materials with high effective friction angles, this leads to the prediction of unrealistically high plastic volumetric expansion, and thus inaccurate high soil strength. Therefore, in an attempt to better capture dilatant response of frictional materials, a non-associative flow rule is employed. This restricts the excessive prediction by specifying a dilatancy angle, inputed as a model parameter, which is much smaller than the angle of internal friction ($\varphi' > \psi$) . [Neto, 2008] This paves the way for improved strength predictions. This is also supported by experimentally determined

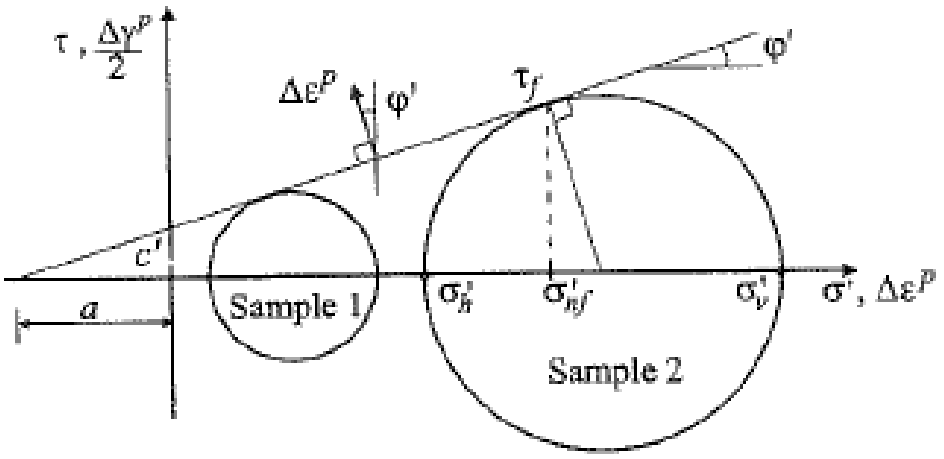

Figure 2-5 Mohr's circle of effective stresss. Reprinted from [Potts, 1999]

plastic strain increment vectors, which are not perpendicular to the yield surface. [Lade, 2005]

Despite the reduction in the magnitude of plastic dilation, the Mohr Coulomb model maintains a constant dilation angle throughout the loading. This implies that the soil will continue to dilate indefinitely as shearing progresses. [Wood, 2004] This is due to the absence of a means to cap the dilation generated by the model. This is in strict violation of real soil behavior, which at significant shearing will continue to deform at a constant volume once the critical state condition is reached. The recommended course to overcome the specified deficiencies of the model is the employment of complex constitutive models, better equipped to capture the dilatant soil response.

2.2.1.1. Parameters

The model requires a total of five parameters. For an isotropic model, the elastic behavior is defined by the Young's modulus and the Poisson's ratio. They can be determined from the other two elastic quantities, shear modulus and the bulk modulus, or as functions of stress, etc. Section 3.3.2 provides an expression for the determination of the Young's modulus as a function of the rigidity index of the soil. The plastic behavior is defined by the remaining three parameters- soil cohesion, angle of internal friction and the angle of dilation. They are easily derivable from simple laboratory tests such as triaxial, direct shear, simple shear, etc. For non-cohesive materials (c=0), Bolton's equations [Bolton, 1986] have proven to be a popular analytical alternative. Section 3.3.4.1 illustrates their use to derive the plastic parameters of a generic medium-dense sand.

2.2.2. **Hypoplastic Soil Model**

A hypoplastic soil model is a rate dependent constitutive model, which relates the strain rate to the stress rate. [Felin, 2002] It is described by a non-linear tensorial equation, which accounts for the dilatancy, barotropy and the pyknotropy of the soil. [Thieken, 2014] The model parameters are related to the granulometric behavior of the soil, making it a preferred material law for modelling granular soil.

Hypoplasticity theory does not require the soil deformation to be separated into elastic and plastic behavior. [Herle, 1999] It models soil behavior without the features of plasticity theory such as yield surface, plastic potential and the flow rule. The absence of these mathematical notions serve as an advantage for hypoplastic models over the widely used elastoplastic models.

Kolymbus [Kolymbus, 1977] proposed the first hypoplastic model in 1977; since then it has been subjected to various modifications. [Stutz, 2018] A tensorial relationship between the objective stress rate and the Eulerian stretching rate was proposed by Wu and Bauer (1994), with the Cauchy stress and void ratio as the state variables. Barotropy and pyknotropy factors were later incorporated into the formulation to take into account the influence of pressure and soil density, respectively. [Gudehus, 1996] von Wolf [Wolffersdorff, 1996] proposed the inclusion of Matsuko and Nakai's limit state surface into formulation, with the aim of obtaining more realistic values for the critical states, and limit states with peak. His is the standard form of the model used for the non-linear modelling of sand behavior. [Stutz, 2018]

The proposed hypoplastic constitutive equation is written as: [Wolffersdorff, 1996]

$$\dot{\boldsymbol{T}} = \mathcal{L}(\boldsymbol{T}, e) : \boldsymbol{D} + \boldsymbol{N}(\boldsymbol{T}, e)||\boldsymbol{D}||$$

where the objective stress rate, $\dot{\boldsymbol{T}}$, is a tensorial function of the Cauchy stress, $\boldsymbol{T}$, stretching rate, $\boldsymbol{D}$, and void ratio, e. The $\mathcal{L}$ and $\boldsymbol{N}$ terms represent a second order linear and fourth order non-linear constitutive tensor, given as:

$$\mathcal{L} = f_s \frac{1}{tr(\hat{\boldsymbol{T}}^2)} (F^2 \boldsymbol{I} + a^2 \hat{\boldsymbol{T}}^2)$$

$$\boldsymbol{N} = f_s f_d \frac{aF}{tr(\hat{\boldsymbol{T}}^2)} (\hat{\boldsymbol{T}} + \hat{\boldsymbol{T}}^*)$$

where, the state variables are described as, $\hat{\boldsymbol{T}} = \frac{\boldsymbol{T}}{tr\boldsymbol{T}}$ and $\hat{\boldsymbol{T}}^* = \hat{\boldsymbol{T}} - \frac{1}{3}\boldsymbol{I}$. [Felin, 2002] The barotropy function, f_s, and the pyknotropy function, f_d, are given by:

$$f_s = \frac{h_s}{n}\left(\frac{e_i}{e}\right)\frac{1+e_i}{e_i}\left(\frac{-tr\boldsymbol{T}}{h_s}\right)^{1-n}\left[3 + a^2 - a\sqrt{3}\left(\frac{e_{i0} - e_{d0}}{e_{c0} - e_{d0}}\right)^{\alpha}\right]^{-1}$$

$$f_d = \left(\frac{e - e_d}{e_c - e_d}\right)^{\alpha}$$

and e is limited by the pressure dependent e_d, e_c and e_i, further described in Section 2.2.2.1. The stress factor, F representing the Matsuoka-Nakai surface is:

$$F = \sqrt{\frac{1}{8}tan^2\psi + \frac{2 - tan^2\psi}{2 + \sqrt{2}tan\psi cos3\theta}} - \frac{1}{2\sqrt{2}}tan\psi$$

where the Lode angle, θ, is:

$$cos3\theta = -\sqrt{6}\frac{tr(\hat{\boldsymbol{T}}^3)}{\left[tr(\hat{\boldsymbol{T}}^2)\right]^{\frac{3}{2}}}$$

with, $tan\psi = \sqrt{3}\left\|\hat{\boldsymbol{T}}^*\right\|$. The constitutive coefficient, a, is given by:

$$a = \frac{\sqrt{3}(3 - sin\varphi_c)}{2\sqrt{2}sin\varphi_c}$$

The state variable void ratio, e, used in the model is described as a function of the strain rate as [Felin, 2002]:

$$\dot{e} = (1 + e)tr\boldsymbol{D}$$

2.2.2.1. Parameters

The hypoplastic soil model as presented by Wolf, requires eight parameters. The critical state friction angle, φ_c, is the only material constant required. [Wolffersdorff, 1996] The granulate hardness, h_s, and exponent, n, take into account the influence of compression. h_s is used as a pressure reference and n takes into account the pressure sensitivity of the grain assembly. They can be determined by conducting a compression test, and reflect the slope and curvature of the compression curve, respectively. [Herle, 1999] n can be mathematically determined in terms of the non-uniformity coefficient, C_u, and the mean grain size, d_{50}, as: [Herle, 1999],

$$n = 0.366 - 0.0341\left[\frac{C_u}{\left(\frac{d_{50}}{d_0}\right)^{0.33}}\right] \qquad \text{Eq. 2.2}$$

where, $d_0 = 1mm$; and

$$h_s = 3p_s\left(\frac{ne}{C_c}\right)^{1/n} \qquad \text{Eq. 2.3}$$

where p_s is the mean skeleton pressure and C_c is the coefficient of curvature.

The maximum, e_{i0}, minimum, e_{d0}, and critical, e_{c0}, void ratios at zero pressure are the fourth, fifth and sixth parameters, dependent on the maximum, minimum, and critical void ratio in terms of: [Wolffersdorff, 1996]

$$\frac{e_i}{e_{i0}} = \frac{e_d}{e_{d0}} = \frac{e_c}{e_{c0}} = exp\left[-\left(\frac{-tr\boldsymbol{T}}{h_s}\right)^n\right] \quad \text{Eq. 2.4}$$

The void ratio parameters can also be approximated as: [Herle, 1999] Eq. 2.5

$$e_i \approx 1.2 * e_{max} \quad \text{Eq. 2.6}$$

$$e_d \approx e_{min} \quad \text{Eq. 2.7}$$

$$e_c \approx e_{max}$$

where e_{max} and e_{min} are the maximum and minimum void ratios, attainable from laboratory soil tests.

The exponent, α, controls the dependency of the peak friction angle on the void ratio. [Stutz, 2018] It can be mathematically determined by using:

$$\alpha = \frac{ln\left[6\frac{(2+K_p)^2 + a^2K_p(K_p - 1 - tan\vartheta_p)}{a(2+K_p)(5K_p-2)\sqrt{4+2(1+tan\vartheta_p)^2}}\right]}{\ln\left[\frac{e-e_d}{e_c-e_d}\right]} \quad \text{Eq. 2.8}$$

where, the peak ratio, K_p can be from:

$$K_p = \frac{1+sin\varphi_p}{1-sin\varphi_p} \quad \text{Eq. 2.9}$$

with a crude first estimation of $\varphi_p = \varphi_c + 12°$, for dense sand. [Cornforth, 1973]

and,

$$tan\vartheta_p = 2\frac{K_p - 4 + 5AK_p{}^2 - 2AK_p}{(5K_p-2)(1+2A)} - 1 \quad \text{Eq. 2.10}$$

with,

$$A = \frac{a^2}{\left(2 + K_p\right)^2}\left[1 - \frac{K_p\left(4 - K_p\right)}{5K_p - 2}\right] \qquad \text{Eq. 2.11}$$

The last parameter, β, controls the relative density to the soil stiffness, [Stutz, 2018] and plays a crucial role for dense sand. It can be mathematically determined by: [Herle, 1999]

$$\beta = \frac{ln\left[E\,\frac{3 + a^2 - f_{do}a\sqrt{3}}{3 + a^2 - f_d a\sqrt{3}}\,\frac{e_i}{1 + e_i}\,\frac{n}{h_s}\left(\frac{3p_s}{h_s}\right)^{n-1}\right]}{ln\left[\frac{e_i}{e}\right]} \qquad \text{Eq. 2.12}$$

where,

$$f_{do} = \frac{e_{i0} - e_{d0}}{e_{c0} - e_{d0}} \qquad \text{Eq. 2.13}$$

2.2.3. **Whyte's bounding surface soil model**

A bounding surface constitutive model formulated to predict the response of suction caissons subjected to tensile loading in sand, was proposed by Whyte [Whyte], based on the Manzari-Dafalias model architecture. The form presented by Whyte, takes into account the inherent anisotropy within the constitutive model and introduces an anisotropic fabric scaling factor to determine the anisotropic state parameter. A very brief description of the model is included below.

The bounding surface model is based on critical state soil mechanics. The yield surface, which defines the onset of plasticity, is a circle in a normalized deviatoric stress space. It is controlled by the critical state surface, the bounding surface and the dilatancy

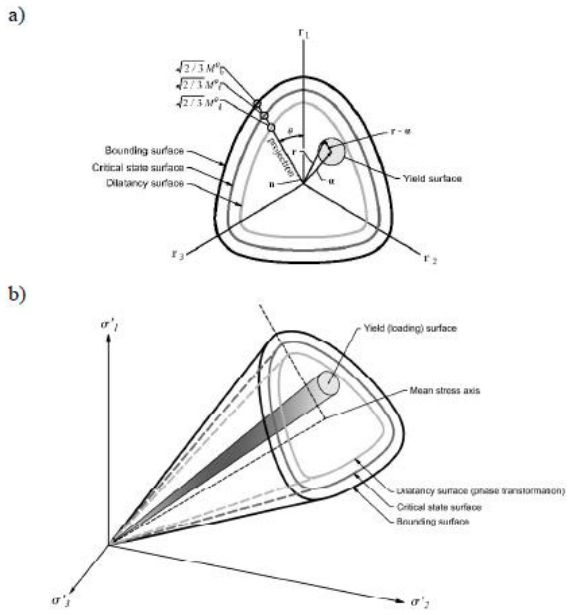

Figure 2-6 Illustration of the yield, bounding, dilatancy and the critical surfaces in a) the normalized deviatoric plane and b) principal stress space. Reprinted from [Whyte]

surface, all described to be non-circular in the deviatoric plane. Fig. 2.6. The critical state surface is fixed in the stress space, while the bounding and the dilatancy surfaces evolve as shearing progresses. Their evolution is controlled by a model state variable, dependent on the critical state line.

The hardening modulus is controlled by the distance between the current stress state and the bounding surface for each plastic strain increment, with the current model allowing only kinematic hardening. The gradient of the plastic potential is controlled by the distance between the current state stress and the dilatancy surface. Though, the gradients of the yield function and the plastic potential are not equal, an associative flow rule is assumed for the current model. The size of the surfaces, and thus the hardening modulus and the stress-dilatancy response vary with the loading direction due to the inclusion of anisotropy into the formulation of the model.

2.2.3.1. Parameters

The model requires a total of nineteen parameters. The elastic response is controlled by three parameters, Shear modulus constant, G_{ref}, Poisson's ratio, *v*, and an elastic modulus mean effective stress power exponent, n; all of which can be determined by triaxial tests. The elastic threshold is defined by the parameter m. The elastoplastic and the stress-dilatancy response are determined by a group of seven parameters. The critical state line is defined by another five parameters, and a further three fabric parameters are used to factor in the laboratory testing conditions. All the parameters can be determined by triaxial compression and extension tests with radial and axial local strain gauges. A detailed explanation of calibration of the model parameters are described in Whyte [Whyte].

2.3. Continuum Finite Element Formulation

Continuum soil mechanics adopts the view that the soil domain to be investigated can be regarded as a continuous mass, rather than as discrete particles. [Chen's book] This indicates that rather than looking into the individual soil particle interactions, the soil properties are approximated as continuously varying. This assumption allows finite element discretization, where the continuum is treated as an assemblage of smaller regions, called finite elements, inter-connected at key points, called nodes. The soil behavior is then simulated at each element using the constitutive model adopted.

2.3.1. Axisymmetric Stress-Strain analysis

An infinitesimal axisymmetric solid is presented in Fig 2.7. Due to the rotational symmetric nature of the geometry, material properties and loading conditions of the case

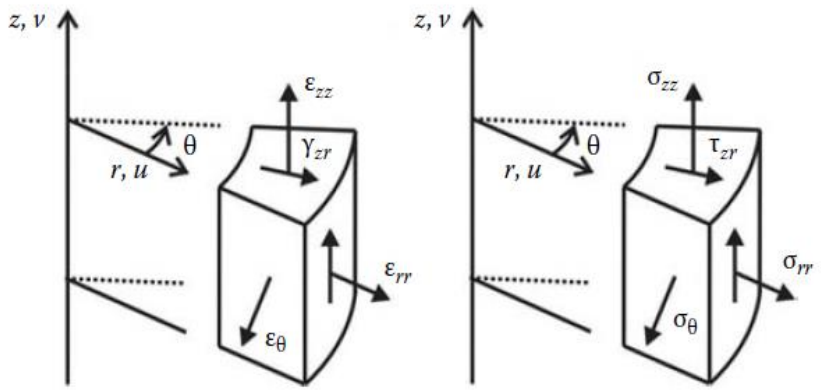

Figure 2-7 Stress and strains on an axisymmetric solid. Reprinted from [Khennane, 2013]

in the current study, an axisymmetric space is adopted. This allows three-dimensional problems to be efficiently solved in two-dimensions.

Axisymmetric analyses are carried out in the cylindrical coordinate system: radial direction (r), vertical direction (z), and the circumferential direction (θ). Due to symmetry, only the radial and vertical displacements are required. This reduces the stress and strain tensors to: [Potts, 1999]

$$[\sigma] = \begin{Bmatrix} \sigma_{rr} \\ \sigma_{zz} \\ \sigma_{\theta\theta} \\ \sigma_{zr} \end{Bmatrix} = \begin{Bmatrix} Normal\ stress\ in\ the\ radial\ direction \\ Normal\ stress\ in\ the\ vertical\ direction \\ Circumferential\ stress \\ Shear\ stress \end{Bmatrix}$$

$$[\varepsilon] = \begin{Bmatrix} \varepsilon_{rr} \\ \varepsilon_{zz} \\ \varepsilon_{\theta\theta} \\ \gamma_{zr} \end{Bmatrix} = \begin{Bmatrix} -\dfrac{\partial u_{rr}}{\partial r} \\ -\dfrac{\partial u_{zz}}{\partial z} \\ -\dfrac{u}{r} \\ -\dfrac{\partial u_{zz}}{\partial r} - \dfrac{\partial u_{rr}}{\partial z} \end{Bmatrix}$$

$$= \begin{Bmatrix} Normal\ strain\ in\ the\ radial\ direction \\ Normal\ strain\ in\ the\ vertical\ direction \\ Circumferential\ strain \\ Shear\ strain \end{Bmatrix}$$

where, u_{rr} and u_{zz} are the displacements in the radial and axial directions, respectively. Due to symmetry, there is no circumferential displacement.

2.3.2. **Finite element formulation**

To study the effects of drainage conditions on soil behavior, effects of pore pressure along with the effective stresses must be taken into account. A two-phase environment with coupling between the soil behavior and the flow through the porous media is utilized. [Smith, 1982]

The finite element formulation is based on Biot's consolidation equation, along with conditions of equilibrium and continuity. The primary unknowns will be the nodal displacements ($\{d\}_n$) and the nodal excess pore pressure ($\{\Delta p_f\}_n$) [Potts, 1999]

Assuming a soil domain, meshed into N elements:

The displacement field of one single element can be defined as:

$$\{\Delta d\} = \begin{Bmatrix} \Delta u_{rr} \\ \Delta u_{zz} \end{Bmatrix} = [N_d] \begin{Bmatrix} \Delta u_{rr} \\ \Delta u_{zz} \end{Bmatrix}_n = [N_d]\{\Delta d\}_n$$

where, u_{rr} and u_{zz} are the displacement components, and the n-subscript represents nodal quantities. N_d represents the displacement interpolation function.

The strain field corresponding to the above displacement field is:

$$\begin{Bmatrix} \Delta\varepsilon_{rr} \\ \Delta\varepsilon_{zz} \\ \Delta\varepsilon_{\theta\theta} \\ \Delta\gamma_{zr} \end{Bmatrix} = \begin{Bmatrix} \frac{\partial}{\partial r} & 0 \\ 0 & \frac{\partial}{\partial z} \\ \frac{1}{r} & 0 \\ \frac{\partial}{\partial z} & \frac{\partial}{\partial r} \end{Bmatrix} [N_d]\{\Delta d\}_n$$

or,

$$\{\Delta\varepsilon\} = [B]\{\Delta d\}_n$$

where, [B] is the strain displacement matrix, and contains the derivatives of the interpolation function.

The stress-strain relationship is defined by the constitutive equation:

$$\{\Delta\sigma\} = [D]\{\Delta\varepsilon\}$$

where, [D] is the constitutive matrix.

Incorporating the effect of the pore fluid, the fundamental constitutive equation in terms of effective stress takes the following form:

$$\{\Delta\sigma\} = [D']\{\Delta\varepsilon\} + \{\Delta\sigma_f\}$$

where, $\Delta{\sigma_f}^T = \{\Delta p_f, \Delta p_f, \Delta p_f, 0,0,0\}$, with Δp_f as the excess pore pressure increment:

$$\{\Delta p_f\} = [N_p]\{\Delta p_f\}_n$$

Here, $\{\Delta p_f\}_n$ is the nodal excess pore pressure increment and N_p is the pore pressure interpolation matrix.

To satisfy equilibrium condition:

The principle of minimum potential energy is invoked to establish equilibrium in a single element:

$$\delta\Delta E = \delta\Delta W - \delta\Delta L = 0$$

$$Total\ energy, E = Strain\ energy, W - Work\ done\ by\ applied\ loads, L = 0$$

The incremental change in strain energy, ΔW is defined as:

$$\Delta W = \frac{1}{2}\int_{Vol} \{\Delta\varepsilon\}^T\{\Delta\sigma\}\ \mathrm{d}Vol$$

Substituting the coupled stress tensor into the equation gives,

$$\Delta W = \frac{1}{2}\int_{Vol} [\{\Delta\varepsilon\}^T[D']\{\Delta\varepsilon\} + \{\Delta\sigma_f\}\{\Delta\varepsilon\}]\ \mathrm{d}Vol$$

The incremental work done by the applied loads, ΔL is defined as:

$$\Delta L = \int_{Vol} \{\Delta d\}^T\{\Delta F\}\ \mathrm{d}Vol + \int_{Surf} \{\Delta d\}^T\{\Delta T\}\ \mathrm{d}Vol$$

the first part is from the body force, F , and the second due to surface traction, T.

From the concept of finite element discretization, the potential energy of the continuum is now attained by summing the potential energies of all the elements. Expressing the pore pressures and the displacements in terms of their nodal values, provides the required equilibrium equation for each element. These assembled, provides the equilibrium equation of the continuum:

$$[K_G]\{\Delta d\}_{nG} + [L_G]\{\Delta p_f\}_{nG} = \{\Delta R_G\} \qquad \text{Eq. 2.14}$$

where,

$[K_G]$ is the global stiffness matrix:

$$[K_G] = \sum_{i=1}^{N}[K_E]_i = \sum_{i=1}^{N}\left(\int_{vol}[B]^T[D'][B]dVol\right)_i$$

$[L_G]$ is a rectangular coupling matrix:

$$[L_G] = \sum_{i=1}^{N}[L_E]_i = \sum_{i=1}^{N}\left(\int_{vol}\{m\}[B]^T[N_P]dVol\right)_i$$

$\{\Delta R_G\}$ is global incremental load vector:

$$\{\Delta R_G\} = \sum_{i=1}^{N} \{\Delta R_E\}_i = \sum_{i=1}^{N} \left[\left(\int_{vol} [N]^T \{\Delta F\} dVol \right) + \left(\int_{surf} [N]^T \{\Delta T\} dSrf \right) \right]_i$$

$$\{m\}^T = \{1\ 1\ 1\ 0\ 0\ 0\}$$

To satisfy continuity conditions:

Fig. 2.8 illustrates an infinitesimal cube with flow. From the law of conservation of

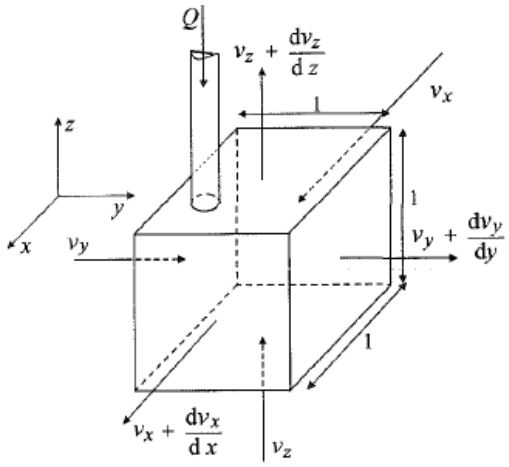

Figure 2-8 Continuity conditions. Reprinted from [Potts, 1999]

mass, the continuity equation for an element is given as:

$$\frac{\partial v_{rr}}{\partial r} + \frac{\partial v_{zz}}{\partial z} - Q = \frac{\partial \varepsilon_v}{\partial t}$$

which states that the outflow from the element is equal to the reduction in volume of the body. [Smith, 1982]

where Q represents any external flow, v is the superficial velocity of the fluid in the radial and vertical directions and is defined by Darcy's law as:

$$\begin{Bmatrix} v_{rr} \\ v_{zz} \end{Bmatrix} = -\begin{bmatrix} k_{rr} & k_{rz} \\ k_{rz} & k_{zz} \end{bmatrix} \begin{Bmatrix} \frac{\partial h}{\partial z} \\ \frac{\partial h}{\partial z} \end{Bmatrix}$$

$$\{v\} = -[k]\{\nabla h\}$$

where, [k] represents the matrix with the coefficients of permeability of the soil. The current study assumes an isotropic soil, thus, $k_{ij} = k$, if $i = j$; and $= 0$, if $i \neq j$. The hydraulic head, h in turn is defined as:

$$h = \frac{p_f}{\gamma_f} + (ri_{Gr} + zi_{Gz})$$

and $\{i_G\}$ represents a unit vector parallel but opposite to gravity, and γ_f is the unit weight of the fluid.

As in the case of equilibrium, continuity equations are attained for each element from the principle of virtual work and then assembled to achieve the continuity equation of the continuum:

$$[L_G]^T \left(\frac{\{\Delta d\}_{nG}}{\Delta t}\right) - [KP_G]\{p_f\}_{nG} = [n_G] + Q \qquad \text{Eq. 2.15}$$

where,

$[KP_G]$ is the global fluid stiffness matrix:

$$[KP_G] = \sum_{i=1}^{N} [KP_E]_i = \sum_{i=1}^{N} \left(\int_{vol} \frac{[E]^T[k][E]}{\gamma_f} dVol \right)_i$$

$$[n_G] = \sum_{i=1}^{N} [n_E]_i = \sum_{i=1}^{N} \left(\int_{vol} [E]^T[k]\{i_G\} dVol \right)_i$$

$$[E] = \left[\frac{\partial N_P}{\partial x}, \frac{\partial N_P}{\partial y}, \frac{\partial N_P}{\partial z}\right]^T$$

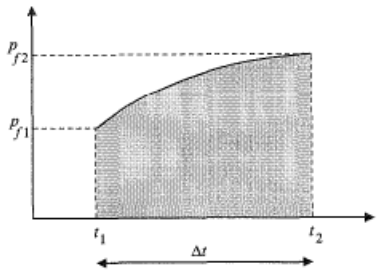

Figure 2-9 Approximation of pore fluid integral. Reprinted from [Potts, 1999]

The equilibrium (Equation 2.14) and continuity (Equation 2.15) system of equations are solved for the primary unknowns by integrating over time, where the solution at time t_1 is known (or assumed), and the solution at time $t_1+\Delta t$ is sought.

The integral of the incremental nodal pore pressure over time is graphically presented in Fig. 2.9. It is assumed that,

$$\int_{t1}^{t2} [KP_G]\{p_f\}_{nG}dt = [KP_G]\left[\theta(\{p_f\}_{nG})_2 + (1-\theta)(\{p_f\}_{nG})_1\right]\Delta t$$

where, $0<\theta<1$; but $\theta=0.5$ provides the most accurate approximation and is unconditionally stable.

The required system of equations (Equation 2.14 (equilibrium) and Equation 2.15 (continuity integral)) can be summarized in the following incremental matrix form:

$$\begin{bmatrix} [K_G] & [L_G] \\ [L_G]^T & -\theta\Delta t[KP_G] \end{bmatrix} \begin{Bmatrix} \{\Delta d\}_{nG} \\ \{\Delta p_f\}_{nG} \end{Bmatrix} = \begin{Bmatrix} \{\Delta R_G\} \\ ([n_G] + Q + [KP_G](\{p_f\}_{nG})_1)\Delta t \end{Bmatrix}$$

2.4. Suction Caissons

The current thesis concentrates on analyzing a tripod suction caisson-jacket foundation as a viable means to support offshore windfarms.

2.4.1. **Loading Conditions**

Though the concept of suction caissons has been prevalent in the engineering world for several decades, it is a fairly recent addition in the offshore renewables sector, supporting mostly heavy oil and gas rigs prior to this. The drastic decrease in the self-weight of the structure it is designed to support alters the resulting loading conditions that the foundation footing is required to sustain.

Loading conditions for offshore wind turbines are significantly different than land-based wind turbines. In addition to the aerodynamic drag on the structure and the 1P and 3P loads exerted by the rotation of the blades of the turbine, wave and current loads in the form of hydraulic drag also need to be taken into account when designing an offshore foundation. [Nikitas, 2016] Fig 2.10. presents the relevant forces acting on an OWT. The

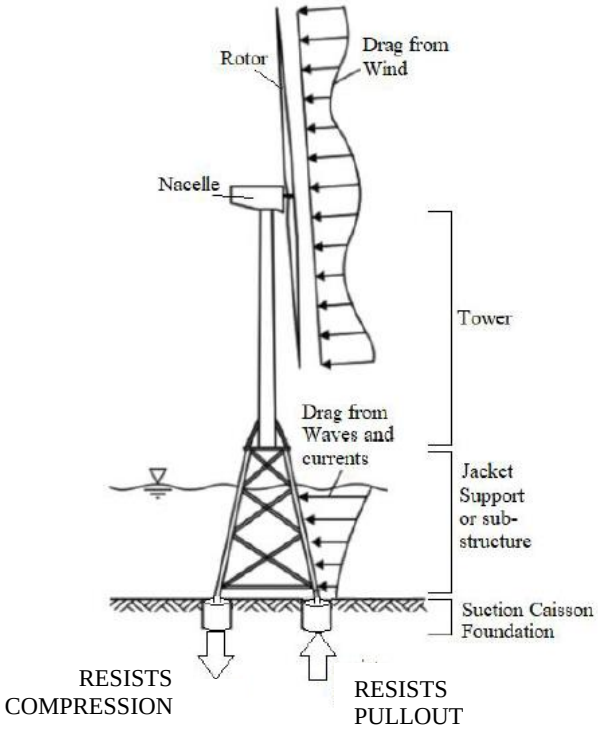

Figure 2-10 Loads on an OWT. Reprinted from [Nikitas, 2016]

cumulation of these conditions results in the horizontal load exceeding the compressive load, leading to the development of large overturning moments at the mudline. [Byrne, 2000] The overturning moments create an opposing ‘push-pull’ compression and tension vertical loading on the multi-bucket system. During extreme storm conditions, the significant overturning moments generated outweigh the restoring moment form the self-weight of the structure, putting the trailing suction caisson of the multi-bucket jacket system into net tension (as illustrated in Fig. 2.8). This makes tensile loading the most unfavorable loading case, and allows the tensile capacity of the trailing suction caisson to dominate the design. [Thieken, 2014]

2.4.2. **Drainage Conditions**

The drainage conditions of the soil prevailing at the installation sites dictate the response of the caissons when exposed to the above-mentioned loads. Suction caissons when subjected to tensile loading, generate zones of negative pore water pressure or suction around them. [Aubeny, 2018] The rate of dissipation of this suction defines the load-bearing behavior of the foundation, which in turn is controlled by the drainage conditions of the soil. Drainage depends on the soil permeability, loading intensity and the size of the foundation. [Vaitkunaite, 2016]

The response of the caisson under an ideal drained condition is described as ‘frictional’ and that under an ideal undrained condition as ‘reverse end bearing’, with partial drainage conditions exhibiting intermediate behavior. [Senders, 2008]

Frictional behavior is when the tensile resistance of the caisson results from its self-weight and the skin frictions mobilized along the outer and the inner surface of the caisson

skirt. Due to the conditions of long-term loading which instigates such behavior, the suction pressure created at the soil-caisson interface below the top cap of the caisson is provided sufficient time to dissipate during the loading itself, resulting in the formation of a gap in the region. On the other hand, short-term loading occurs at a much faster rate than the rate of dissipation of the suction, resulting in the generation of significant pore pressure at the soil-caisson interface below the top cap. Due to this, no gap is created in the region, and the entire volume of soil mass inside the caisson gets pulled up during the loading- resembling the behavior of a soil plug. Additionally, frictional resistance is also mobilized along the outer surface of the skirt. [Thieken, 2014] This results in four contributors to the soil resistance – the self-weight of the caisson, the skin friction along the outer surface of the skirt, the weight of the soil plug and the suction pressure generated. Such a behavior is termed as 'reverse end bearing' and provides the strongest resistance to an uplift loading condition. Fig. 2.11 demonstrates the failure mechanisms described.

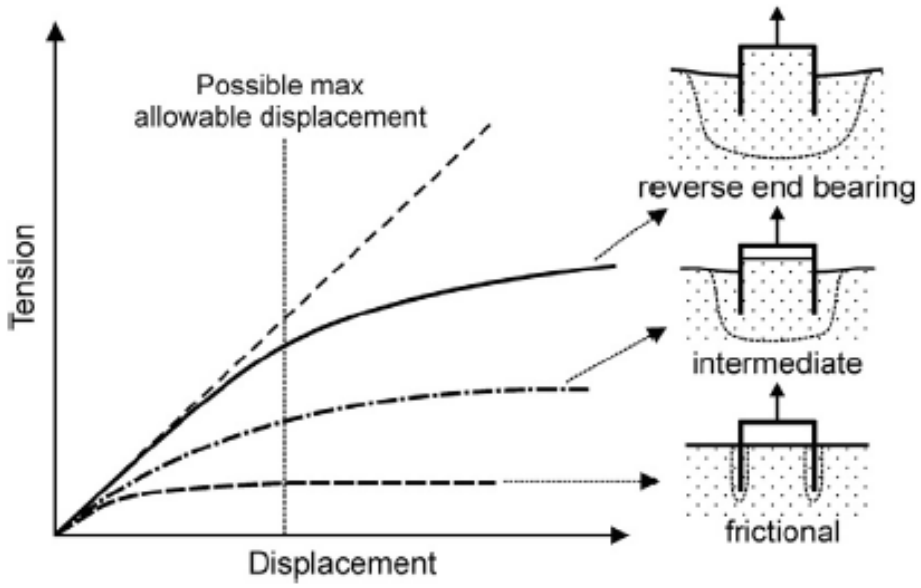

Figure 2-11 Failure mechanisms. Reprinted from [Senders, 2008]

2.4.2.1. Coarse grained soil

Coarse grained soil, as described in Section 2.1.2, possesses high soil permeabilities. Due to this, the pore water is allowed to pass through the soil media rapidly, occupying the region at the soil-caisson interface below the top cap. Thus, in the absence of a suction pressure pulling up the soil plug, the tensile load is resisted only by the mobilized shear resistance in the region around the skirt along with the self-weight of the caisson, exhibiting a 'frictional' response.

However, due to the locations of the erection of OWT, extreme environmental conditions need to be accounted for as well- individual storm cycles which might be rapid enough to result in fully undrained cases. To simulate such a response, the loading rates are increased. [Thieken, 2014] This will result in an undrained to intermediate loading analysis even for highly permeable coarse-grained soil. Fig. 4.28. shows the response of a suction caisson in dense sand subjected to a monotonic vertical uplift. The increase in the loading rate signifies the transition into an undrained state. It can be observed from the figure that though significant undrained capacity is generated, large deformations are required to mobilize the full capacity, whose probability of occurrence is highly unlikely. [Thieken, 2014]

2.4.2.2. Fine grained soil

Fine grained soil such as clay, due to their granular arrangement, possesses lower permeabilities as compared to coarse grained soil. Due to this, the suction pressure generated during loading is dissipated at a much slower rate than it is formed. This results in a 'reverse end bearing' response, and the suction pressure along with the self-weight of

the soil plug also contributes to the resistance against the tensile load. This being favorable, most suction caisson installations are preferred in clay rich beds. [Cotter, 2009] However, if the if the loading rate is significantly lowered to allow full suction pressure dissipation, a long-term analysis can be conducted where 'frictional' response is exhibited. [Cotter, 2009]

2.4.3. **Analytical tensile capacity**

The tensile capacity of a suction caisson in sand is widely determined analytically by the formulations presented by Houlsby and Byrne [Houlsby, 2005]. Their theory factored in the effects of soil permeability, rate of load application, pore pressure generation as well as the limiting conditions of cavitation, and produced a simplified expression where the soil capacity showed an increase with the undrained condition of the soil.

The drained capacity is represented as the sum of the external and the internal frictional loads, and takes into account the reduction of vertical stresses close to the caisson due to the frictional forces further up the caisson: [Houlsby, 2005]

$$V' = -\gamma' {Z_0}^2 y\left(\frac{h}{Z_o}\right)(Ktan\delta)_o(\pi D_o) - -\gamma' {Z_i}^2 y\left(\frac{h}{Z_i}\right)(Ktan\delta)_i(\pi D_i)$$

where the function, $y(x) = \exp(-x) - 1 + x$, and uniform stress is assumed inside the caisson.

The undrained capacity depended on the dilation of the soil, the loading rate, and the transient pore pressures developed due to the rapid loading.

$$V' = -sA\left(1 + \left(\frac{2h}{D}\right)(ktan\delta)\right)$$

where, s is the pressure in the caisson with respect to the ambient seabed water pressure, and could be represented in terms of the loading rate as:

$$s = -\frac{\pi}{4F}\frac{D\gamma_w}{k_o}\frac{dh}{dt}$$

Their proposed methods were validated against small scale tests done on different types of sand at different loading rates, as well as field tests conducted at a prepared site in Luce bay, Scotland. [Houlsby, 2005]

2.4.4. **Previous works**

Several studies have been conducted to understand and thus, develop models capable of predicting the tensile behavior of suction caissons in dense sand. Laboratory floor tests, centrifuge tests and numerical analysis have been carried out with successful results to aid the offshore industry to adopt suction caissons in the form of mono-bucket as well as multi-bucket jacket systems as a viable foundation option for the emerging field of offshore renewables. Following is a brief description of a few.

2.4.4.1. Experimental studies

The current study refers to the experimental work of Senders [Senders, 2008] and Bienen [Bienen, 2018] for comparative studies to establish the validity and the accuracy of the finite element model developed. The following sections contain a short outline of the same.

2.4.4.1.1. Senders centrifuge tests

Senders looked into the behavior of suction caissons as tripod foundations for offshore wind turbines in sand and layered soils. Centrifuge tests were performed on small scale suction caissons to study their response during the installation phase and during monotonic

and cyclic loading. [Senders, 2008] Evaluation of the possible loading conditions an OWT would be subjected to during its lifetime was conducted by employing an existing computer program, arriving at the conclusion that the tensile capacity of the suction caissons in sand should be treated as the critical case.

Centrifuge tests were performed at an acceleration of 100g at the geotechnical beam centrifuge at the University of Western Australia, with the aim of prototype caisson dimensions between 4 to 12m in diameter and 4 to 8m in height, with aspect ratio in between 0.5 to 1. Dense sand and silt or clay overlaying dense sand were tested, with silicon oil, at a viscosity of 100 centistokes, used to simulate the realistic fluid flow through the soil.

For the suction installation tests, the resistance achieved was significantly lower than installation by jacking. The uplift capacity tests were performed for drained and undrained soil conditions with the results indicating the undrained capacity to be 40% higher than the drained capacity.

The centrifuge results were then used to formulate a model to predict the installation process and the tensile and cyclic response of a suction caisson in dense sand and layered soil.

2.4.4.1.2. Bienen's centrifuge tests

Bienen [Bienen, 2018] conducted a series of centrifuge tests to study the installation, cyclic loading and subsequent extraction of a suction caisson. The study explores the experimental arrangement and procedures to simulate the behavior of a tripod suction caisson system to support OWT in the dense sands of the North Sea. The installation

procedure, its dependence on the pumping rate and its effect on the foundation system, along with the effects of the drainage conditions, average stress and cyclic amplitude on the tensile response has been evaluated.

The tests were also conducted using the geotechnical beam centrifuge at UWA, with an acceleration of 100g. The prototype caisson dimensions were 8m in diameter and 4m in length (aspect ratio = 0.5), subjected to load paths representing the generic loading conditions for an 8 MW turbine, in 40m water. The Baskarp Sand soil type selected mimicked the particle size distribution of North Sea dense sands, and employed high viscosity pore fluids for the higher frequency loading cases.

The results of the study reinforced previously established theories about the tensile behavior of suction caissons in dense sand subjected to a range of drainage conditions.

2.4.4.2. Numerical studies

The complex undrained behavior of dense sand is better simulated by numerical analysis than predictions by analytical models. [Thieken, 2014] They also require the adoption of sophisticated soil models, since conventional plasticity theories fail to capture this behavior. [Byrne, 2000] Several numerical studies have been conducted to better understand this response. Studies by Achmus [Achmus, 2014], Mana [Mana,2014], Cerfontaine. [Cerfontaine, 2015], Thieken [Thieken, 2014], Whyte [Whyte], Green [Green, 2019] have been referred to during the course of this thesis. The following sections present a brief outline of the finite element analysis of two such studies.

2.4.4.2.1. Numerical simulations using Hypoplasticity soil model by Thieken [Thieken,2014]

Numerical studies conducted by Thieken and Achmus at the University of Leibniz developed a fully coupled finite element model to simulate the response of a suction caisson in IGtH sand subjected to tensile loading. The coupled pore fluid diffusion and stress analysis performed focused on the partially drained soil conditions reproduced by varying the pull-out rates of the caisson. In order to account for the dilatancy, barotropy and pyknotropy of granular soil, a rate dependent Hypoplastic soil model as presented by Wolf [Wolffersdorff, 1996] was adopted to model the soil behaviour. This soil model is described in Section 2.2.2. The soil permeability was expressed as a function of the void ratio, using the Kozney-Carmen equation, as described in Section 3.3.3.

The analysis was performed in Abaqus. The model was developed in axisymmetric space, taking advantage of the symmetric nature of the problem. In order to accurately represent the transfer of pore pressure from the soil body to the top-cap of the bucket foundation, and to account for the creation of a gap below the top-cap, a thin layer of negligible stiffness elements is generated, with properties similar to that of water. The soil around the tip of the caisson skirt was also modelled with similar low-stiffness elements. The adoption of such a layer also aids in the convergence of the numerical method under rapid loading conditions.

Their method was successfully validated by performing back calculations of reported field tests. Parametric studies established the influence factors concurrent with earlier findings. In addition, they reported the strong impact of the bucket diameter on the

drained capacity and the skirt length for the undrained capacity. Their numerical study was also able to fully simulate the undrained behaviour.

2.4.4.2.2. Numerical simulations using the bounding surface soil model by Whyte

Whyte studied the behavior of a suction caisson in dense sand subjected to tensile loading. A bounding surface plasticity model based on the model architecture of Manzari and Dafalias was developed to overcome the deficiencies of conventional plasticity models to predict the dilatant response of dense sand. The model parameters were calibrated by single element tests with the consideration of inherent anisotropy. This soil model is described in Section 2.2.3.

An axisymmetric fully coupled flow- deformation finite element analysis was performed in the commercially available FE code, Plaxis. The suction caisson was subjected to a range of pull-out velocities to simulate drainage conditions of the soil. A low-stiffness water layer beneath the top-cap was adopted, similar to the work by Thieken [Thieken, 2014] and others [Mana, 2014]. In addition to this, a superficial top sand layer outside the bucket and an elastic toe region below the skirt tip were created following the recommendations by Cerfontaine [Cerfontaine, 2015]. These artificial add-ons were modeled as linear elastic with parameters one order of magnitude lower than that of the soil model. [Cerfontaine, 2015] These adoptions aided in overcoming convergence issues and minimized the risk of high stress formations at the skirt tip.

The finite element model developed and the soil model proposed were validated by conducting comparative studies against the centrifuge test results of Senders [Senders, 2008] and Bienne [Bienen, 2014]. The results depicted an accurate matching of the

experimental data, and the model's successful ability to capture the effects of soil density, stress level and path dependency.

3. FINITE ELEMENT MODEL

This chapter gives an overview of the finite element model developed to simulate the response of the trailing suction caisson in a multi-bucket jacket in sands when subjected to monotonic tensile loading. A fully-coupled system is utilized which allows for the transient analysis of a partially or fully drained porous medium and adopts an effective stress principal to describe its behavior. The analysis was performed with the numerical formulation available in the software package ABAQUS-6.12.1, and the mesh generation in the programming language MATLAB.

3.1. Model Geometry

The model comprises of a rigid, impermeable skirted foundation in an isotropic soil with a stress dependent Young's Modulus, E. In addition to this, for the accurate representation of the transfer of pore pressure from the soil body to the top-cap of the caisson, a thin layer of negligible stiffness elements is generated. The finite element mesh generated is presented in Fig. 3.1.

SOIL TYPE	DIAMETER	LENGTH	ASPECT RATIO	SKIRT THICKNESS
	d in meters	l in meters		t in millimeters
Generic medium dense sand	8	4	0.5	50
UWA Superfine silica sand	6	6	1	30
IGtH dense sand	10	10	1	30

Table 3-1 Geometry of suction caisson

Suction caisson of aspect ratios 0.5 and 1 are simulated in this study, with Diameter D, length L and wall thickness t. (Table 3.1) The geometry was selected from literature

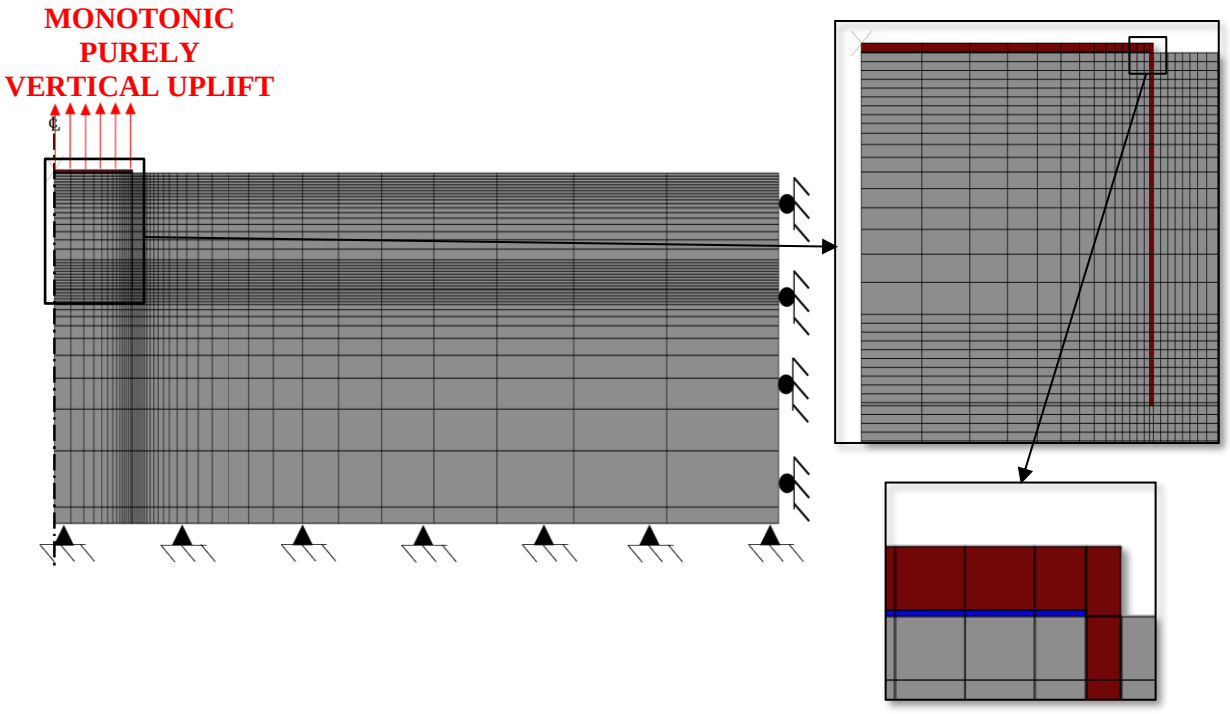

Figure 3-1 a) Finite element mesh generated b) Magnified view of the suction caisson c) Magnified view of the water layer

review, so as to be able to conduct accurate comparisons. The caisson is placed in a soil doma in, with the assumption of causing no disturbance to the soil in the vicinity during the installation process. Thus, the calculations are conducted for a wished-in place suction caisson.

The size of the soil domain is selected so as not to allow the effect of boundary conditions in the model. It is fixed at 3.5 times the length of the caisson and 6 times its diameter. [Thieken, 2014] Since the analysis is conducted for a purely vertical load, and no lateral loads are involved, only a 2-dimensional axisymmetric model is developed. The symmetric nature of the geometry of the structure and the loading conditions about the central axis of the caisson, allows for a more efficient study.

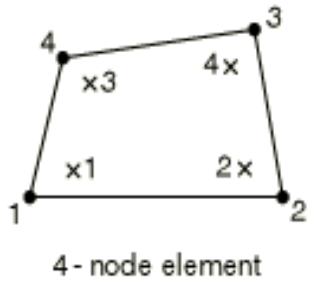

Figure 3-2 Four noded element. Reprinted from [ABAQUS, 2013]

3.2. Mesh Analysis

3.2.1. **Elements**

The soil domain is meshed using elements, from the element library available in ABAQUS/Standard, equipped to perform displacement and pore-pressure analysis in an axisymmetric model. CAX4P elements are selected, which are two-dimensional, 4-noded solid continuum (C) axisymmetric (AX) displacement and pore pressure (P) elements, with first-order interpolation and full integration. Since the caisson material (i.e., steel) possesses negligible permeability, comparable elements of CAX4 are used to mesh it. Fig. 3.2 illustrates a generic CAX4 element.

Continuum axisymmetric elements are used to model a continuum mass in a 360^0 ring. [ABAQUS, 2013] They require only the coordinates of the nodal points to define their geometry, which must be ordered in a counter-clockwise direction.

The CAX4 elements possess 2 active degrees of freedom at each of its 4 nodes – displacement along the x and the y axis, while CAX4P elements have pore pressure as an additional variable at the nodes. The pore-pressure and the displacement are interpolated linearly from the nodes. [ABAQUS, 2013]

3.2.2. **Boundary Conditions**

3.2.2.1. Displacement Boundary Condition

In order to produce reactive forces against the applied loading, boundary conditions are placed at the periphery and the bottom of the soil domain. Radial movement is fixed at the far end by applying a displacement/rotation boundary condition – roller support at the nodes, but vertical deformation is allowed. At the bottom of the domain, movement is restrained in both the vertical and radial directions by applying a simply supported displacement/rotation boundary condition.

The central axis of the suction caisson acts as the axis of symmetry for the current finite element model. It is restrained in the horizontal direction since such movement is un-realistic in an axisymmetric space. Vertical movement is allowed along this line. The monotonic tensile loading studied for this thesis is applied along this axis of symmetry.

3.2.2.2. Pore-pressure Boundary Condition

The seepage path is defined by controlling the pore pressure degree of freedom for the nodes at the boundary of the model. A fixed pore-pressure degree of freedom represents a permeable surface. This degree of freedom is fixed at the top, side and the base of the soil domain to simulate a free drainage surface. Care is taken to ensure that the surface between the top cap of the caisson and the thin water layer is made impermeable but the surface between this water layer and the soil beneath it is made permeable. The axis of symmetry and the caisson as a whole are designed as impermeable. These conditions define the flow of water through the soil body and along the caisson walls.

3.2.3. **Interface behavior**

ABAQUS requires well defined contact formulation to simulate the interaction between the different parts of the model over the course of the analysis. The contact equations are assigned onto the group of nodes forming the interacting surfaces, called the 'contact pair'. [ABAQUS, 2013]

In the current model, four contact pairs are described – the inner wall of the caisson skirt with the soil inside, the outer wall of the caisson skirt with the outer soil, the tip of the caisson skirt with the soil at the bottom, and the bottom of the caisson top-cap with the inner soil (where a thin layer of water elements are introduced).

A master-slave relationship was established between the caisson and the surrounding soil. The caisson, designed as a rigid body, is made to act as the master-surface and the soil body acts as the slave-nodes. The caisson is also constructed of stiffer material and has a coarser mesh density than the soil domain – fulfilling requirements to be the master surface between the two. [ABAQUS, 2013]

3.2.3.1. Caisson skirt and the soil

The caisson skirt is built to be in direct contact with the surrounding soil. A node-to-surface contact discretization is adopted to define the caisson skirt walls and the inner and outer soil contact pair. This traditional method establishes interaction between the two surfaces by interpolating the values of the master (caisson skirt) surface onto the projected location of each slave (soil) node on the master surface. [Abaqus, 2013]

To account for the expected stress concentrations at the skirt tip, a surface-to-surface contact discretization is adopted for the skirt tip and bottom soil contact pair. In this particular discretization, contact conditions are averaged over the soil (slave) surface, instead at the individual soil nodes. This improves contact pressure accuracy since the shape of both the surfaces are considered. [ABAQUS, 2013]

The relative motion between the contact pairs are calculated using the small-sliding tracking approach. It is the more computationally efficient approach available in ABAQUS/Standard and is based on linear approximation. According to this method, throughout the analysis, each slave (soil) node will interact with the same local master nodes, chosen on the basis of the undeformed geometry of the model. The degree of interaction is computed based on the proximity of the nodes to the master surface.

The isotropic Coulomb friction model is used to define the frictional behavior between the contact pairs. The concept behind this model is to relate the tangential (shear) behavior with the normal force between the contact pairs. A critical shear stress is defined for each interaction, beyond which the bodies in contact will begin to permanently slide. [Lees, 2006] This value depends on the contact pressure between the two surfaces and the coefficient of friction.

$$\tau_{crit} = \mu * p$$

where, μ is the coefficient of friction and p is the effective normal pressure. [ABAQUS, 2013]

The coefficient of friction, μ is defined as:

$$\mu = \tan(\varphi_{in})$$

where, φ_{in} is the interface friction angle, which in turn is defined as:

$$\varphi_{in} = \delta * \varphi$$

where, φ is the frictional angle of the soil and δ is the correlation between the two.

The interface friction is generally assumed to be between half or whole times the internal shear strength of the soil, depending on the characteristics of the surface. This provides a range between 0.5 to 1 for the value of δ. [Lees, 2006, Ahmed, 2015] Studies conducted earlier have also established that though the axial resistance is influenced by this value, the pull-out capacity of the caisson for typical loading conditions is not significantly influenced. [Ahmed, 2015]

The current study assumes $\delta = 0.5$ for the generic medium dense sand. The interface soil properties for UWA Super-fine Silica Sand and IGtH dense sand are obtained from laboratory tests conducted at the respective Universities and have been represented in Table 3.2.

SOIL TYPE	INTERFACE FRCITION ANGLE (degrees)
Generic Medium Dense Sand	20
UWA Superfine Silica Sand	20.951
IGtH Dense Sand	20.8 [Thieken]

Table 3-2 Interface properties for the different soil types

The normal behavior is controlled by the tensile strength ($= c * \tan(\varphi_{int})$) at the interface, where separation occurs if the tensile stress exceeds this value.

An additional condition of no separation was applied to the interface between the inner wall of the skirt and the soil. [Mana, 2014] This prevented numerical convergence

problems when running the model for large displacements, which is required to mobilize the undrained capacity.

Fig. 3.3 presents the distribution of the shear stress and the normal pressure along the outer wall of the caisson skirt as obtained from ABAQUS, for the simulation of a vertical uplift loading condition in drained generic medium-dense sand. The slope of the graph for the outer wall and the inner wall are 0.129 and 0.134, respectively. (Desired slope = coefficient of earth pressure at rest * coefficient of friction = 0.4 * 0.3 = 0.12) The close values show the variation between the shear stress along the skirt and the normal contact pressure is linearly dependent on the coefficient of friction. This confirms that the numerical model is correctly implementing the Coulomb friction model. This has been further looked into in Section 4.1.1.5.3.

3.2.3.2. Caisson top-cap and soil

The top-cap of the caisson and the soil inside the caisson are connected by a thin layer of interface elements. This layer is made to resemble the physical properties of water. [Thieken, 2014; Achmus, 2014; Mana, 2014; Ryan, 2019]

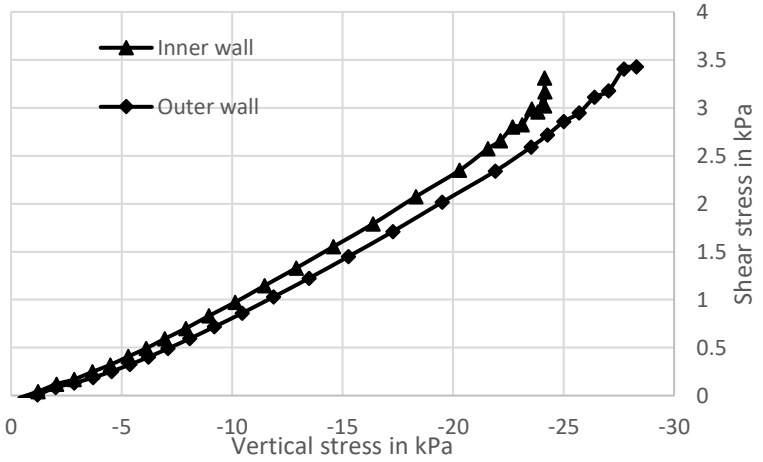

Figure 3-3 Shear stress vs vertical stress

Their primary function is to maintain net suction force on the top-cap of the caisson, while ensuring that no tensile forces are transferred into the soil during uplift. This layer also enables the formation of a gap below the top-cap during drained loading. As stated by Mana [Mana], the concept behind this approach is that the water elements will not undergo immediate volume change during loading, but will instead produce excess pore pressure within the elements. The layer is designed with negligible stiffness and Poisson's ratio to ensure that the expected expansion of the layer does not result in unrealistically high effective stresses along it. [Whyte] To accurately simulate the desired behavior, the water layer is directly bonded to the soil elements below it, and follows a master-slave relationship with the caisson top-cap (master) above it. A tie constraint with the nodes of the water layer as the slave is implemented to ensure the continuous transfer of pore pressure into the surface of the top-cap.

Loading under drained conditions, which occur gradually over time, causes this layer to undergo volumetric expansion whereas, for undrained conditions, no volumetric expansion is detected. However, the suction transferred causes the whole soil body inside the caisson to undergo an uplift. This phenomenon is described in detail in Section 2.4.2. Fig. 4.8 demonstrates the behavior of the water layer under a drained loading condition vs an undrained case.

3.3. Material Properties and Model Parameters

3.3.1. Relative density

Relative density is a simple soil parameter used to define the degree of compactness of the soil particles. [Kulhawy, 1990] For the case of a generic medium-dense sand,

Meyerhof [Kulhawy, 1990] provides a range of 40% to 80% for its value. Their average, 60%, has been adopted in the current study.

For the UWA Superfine Silica Sand, the maximum and minimum void ratio are 0.84 and 0.50, respectively. The tests were performed at an initial void ratio of 0.535, giving a relative density of (~) 90%. For the simulations to compare with centrifuge test results by Bienen [Bienen, 2018], a relative density of 95% was used, with an initial void ratio of 0.57.

Very dense IGtH sand was referred to, with relative density 77% and initial void ratio of 0.6. [Thieken, 2014]

ABAQUS requires the mass densities of all the parts of the model to establish initial stress conditions due to gravity. The densities for three soil types were calculated from their unit weights. [Kulhawy, 1990]

$$\rho = \frac{\gamma}{g}$$

where, a gravitational acceleration of 9.807 m/s^2 is used.

Since an effective stress analysis is conducted, the submerged unit weights of the soil are considered.

The steel suction caisson and the thin water layer are assigned typical density values for their respective materials. Table 3.3 lists the unit weights and the density values adopted in the current project.

PART		Effective Unit Weight (kN/m^3)	Mass Density (kg/m^3)
Soil	Medium-Dense Sand	8.2 [EAU]	8044.2
	UWA Super-fine Silica Sand	10.6 [Tran]	10398.6
	IGtH Sand	10.31 [Thieken]	10114.11
Steel Suction Caisson		78 [Thieken]	76518
Water elements		10	9807

Table 3-3 Soil densities for the different soil types

3.3.2. **Young's Modulus of Elasticity**

The soil is modelled with an isotropic Young's modulus, *E*, expressed as a function of the rigidity index. It is dependent on the initial vertical stress state of the soil and made to vary through the depth of the soil domain.

$$E = I_r * [2(1 + \upsilon)(\sigma_v * tan\varphi)]$$

where the rigidity index, I_r, is defined as:

$$I_r = (a * D_r + b)[m_0 + m_1 * \log(\sigma'_c) + m_2 * log^2(\sigma'_c)$$

with the empirical values for a, b, m_0, m_1, m_2, are provided in Fig. 3.4. [Al Hakeem, 2019]

The Poisson's ratio is another parameter which controls the elastic response of the soil. For the generic medium-dense sand, a value of 0.3 was adopted using the following equations.

$$\upsilon = 0.1 + 0.3 * \varphi_{rel}$$

with, the relative friction angle, φ_{rel} is determined from: [Kulhawy, 1990]

$$\varphi_{rel} = \frac{\varphi_p - 25}{45 - 25}$$

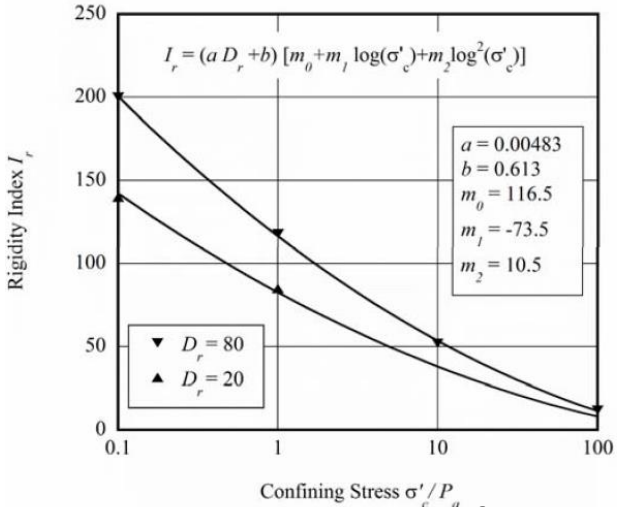

Figure 3-4 Relation between Rigidity index and confining stress. Reprinted from [Al Hakeem, 2019]

3.3.3. **Permeability**

The permeability of the soil is another important parameter in describing the soil behavior. In the numerical model, the coefficient of permeability was defined in different ways depending on the failure model used.

For the cases with the Mohr-Coulomb mode, permeability was defined for the initial void ratio at the beginning of the analysis, and subsequent values determined by the in-built permeability model in ABAQUS/Standard based on Darcy's Law. The current study uses a value of $5e^{-4}$m/s [Kulhawy, 1990] for the generic medium-dense sand at a void ratio of 0.5.

An initial value of 10.9 e^{-5}m/s [Whyte] at a void ratio of 0.535 was used for the base case in the studies with the UWA Superfine Silica Sand, and $8.04e^{-5}$m/s at a void ratio of 0.57 for comparison with Bienen's Centrifuge test results. [Bienen, 2014]

For the study with the hypoplastic soil model, on IGtH sand, permeability was specified by the user for a range of void ratios in ABAQUS, using the semi-empirical Kozney-Carman equation.

$$k_{K-C} = \left(\frac{\gamma_w}{\mu_w}\right).\left(\frac{1}{C_{K-C}}\right).\left(\frac{e^3}{1+e}\right).\left(\frac{1}{{S_0}^2}\right)$$

At the assumed temperature of 10^0C, $\frac{\gamma_w}{\mu_w}$ is equal to 7.645. The Kozeny-Carman empirical coefficient was set to 5 and S_0 = 1.633e^4 based on the grain size distribution. [Carrier, 2003]. This allowed permeability to be accurately updated as the void ratio changed during uplift of the caisson, thus taking into account the expansion and contraction of the soil.

The water elements were modelled with significantly higher permeability than the soil to ensure a uniform distribution of pore pressure throughout the layer. The initial permeability values along with their corresponding void ratios are presented in Table 3.4.

SOIL	INITIAL PERMEABILITY (m/s)	INITIAL VOID RATIO
Medium-Dense Sand	5e^{-4}	0.5
UWA Super-fine Silica Sand	10.9 e^{-5}	0.535
	8.04e^{-5}	0.57
IGtH Dense Sand	7.73e^{-4}	0.6

Table 3-4 Initial void ratio and permeability for the different soil types

The coefficient of consolidation adopted is derived from the following expression [Davis, 1968]:

$$c_v = \frac{kE}{\gamma_w}\frac{(1-\upsilon)}{(1-2\upsilon)(1+\upsilon)}$$

This was calculated at two-thirds of the caisson skirt length, resulting in a value of 0.2141m^2/s for the UWA Superfine Silica Sand.

3.3.4. **Mohr-Coulomb soil model parameters**

ABAQUS requires three input parameters to define the plastic behavior of the elasto-perfectly plastic Mohr-Coulomb failure model – angle of internal friction, dilation angle and cohesive stress. Though, they are dependent on the effective stress state of the soil, the current study assumes a constant soil strength profile. The stress state at two-thirds the caisson skirt length is taken as the average stress value for subsequent stress dependent parameters.

3.3.4.1. Generic Medium-dense sand

The angle of peak internal friction is derived from the equations set forth by Bolton [Bolton, 1986], which also interrelates the dilation with the relative density of the soil.

$$\varphi'_{max} - \varphi'_{crit} = a * I_R = 0.8 * \psi_{max}$$

where, the value of a, as provided by Bolton, is 5 for plane strain and 3 for triaxial strain. Thus, 5 in the current study. A critical state friction angle of 33degrees is assumed, as is common practice for medium-dense sand. [Bolton, 1986; Kulhawy, 1990] The relative dilatancy index, I_R, is dependent on the soil relative density and the mean principle stress in the form:

$$I_R = I_D(10 - lnp_s') - 1$$

For the adopted relative density of 60%, the peak friction and dilation angles used were 39 degrees and 9 degrees, respectively.

3.3.4.2. UWA Superfine Silica Sand

For the UWA Super-fine Silica Sand, the soil model parameters for Mohr-Coulomb were attained from published results of Direct Shear and Simple Shear tests conducted on the soil at UWA, for a stress level at two-thirds the caisson skirt length.

The base case for this soil type was modelled for an initial void ratio of 0.535 (Relative density ~ 90%). For the skirt length of 6m, with the vertical stress at its two-third depth, constant friction angle of 41 degrees and dilation angle of 10 degrees were selected. [Chow, 2019]

The other caisson geometry studied for this soil type was aimed at conducting comparison against centrifuge tests by Bienen [Bienen, 2018]. The tests were performed for an initial void ratio of 0.57 (Relative density ~ 95%) [Bienen, 2018]. With a skirt length of 4m, the peak friction and dilation angles were set at 43.4 degrees and 17.9 degrees, respectively. [Soil report]

3.3.4.3. IGtH Dense Sand

The Mohr Coulomb parameters for the IGtH sand used in the last phase of the project were determined by using Bolton's equations on the soil properties adopted by Theiken [Thieken, 2014]. For a relative density of 77 %, and critical state friction angle of 31.7 degrees, calculated peak friction angle and dilation angles were 45.84 degrees and 14.14 degrees, respectively.

To avoid numerical convergence failures in ABAQUS, cohesion was set to $1kN/m^2$ as recommended by previous studies, throughout the thesis. [Ahmed, 2015]

Table 3.5 summarizes all the Mohr Coulomb model parameters adopted in the project.

SOIL	RELATIVE DESNITY	PEAK FRICTION ANGLE	PEAK DILATION ANGLE
		(degrees)	
Medium-Dense Sand	60%	39	9
UWA Super-fine Silica Sand	90%	41	10
	95%	43.3	17.9
IGtH Dense Sand	77%	45.84	14.14

Table 3-5 Mohr Coulomb model parameters for the different soil types

3.3.5. **Hypoplastic soil model parameters**

The Hypoplastic soil model was implemented in Abaqus via a User Subroutine written in FORTRAN by Felin [Felin, 2002].

3.3.5.1. IGtH Dense Sand

The model parameters adopted for the IGtH soil were the same used by Thieken [Thieken, 2014] and are given in Table 3.6.

PARAMETER	VALUE
Critical state friction angle, ϕ_c	31.7
Granular hardness, h_s	3300 MPa
Exponent, n	0.26
Minimum void ratio, e_{do}	0.499
Critical void ratio, e_{co}	0.789
Maximum void ratio, e_{io}	0.947
Exponent, α	0.21
Exponent, β	1.00

Table 3-6 Hypoplasticity model parameters for IGtH dense sand. Reprinted from [Thieken, 2014]

3.3.5.2. UWA Superfine Silica Sand

The Hypoplasticity soil model parameters for UWA Superfine Silica Sand were calculated using the equations described in Section 2.2.2.1 (Eq.2.2 to Eq.2.13). The

additional soil properties required for their determination were attained from consolidation tests and sieve analysis tests done at UWA, and have been listed in Table 3.7. The model parameters were calculated at a stress level of two-thirds the caisson skirt and have been listed in Table 3.8.

PROPERTY	VALUE
Maximum void ratio, e_{max}	0.84
Minimum void ratio, e_{min}	0.5
50% sieve passing diameter, d_{50}	0.18 mm
Coefficient of curvature, C_c	0.005
Coefficient of uniformity, C_u	1.67

Table 3-7 Soil properties of UWA Superfine Silica Sand

PARAMETER	VALUE	
	Skirt length of 6m	Skirt length of 4m
Critical state friction angle, ϕ_c	33.1^o	33.1^o
Granular hardness, h_s	211929.9 MPa	17378.9 MPa
Exponent, n	0.2657	0.2657
Minimum void ratio, e_{do}	0.5	0.5
Critical void ratio, e_{co}	0.84	0.84
Maximum void ratio, e_{io}	1.008	1.008
Exponent, α	0.0346	0.075
Exponent, β	1.00	1.00

Table 3-8 Hypoplasticity model parameters for UWA Superfine Silica Sand

3.4. Loading Conditions

3.4.1. Geotstatic Loading

In most geotechnical analyses in ABAQUS/Standard, the first loading condition must be to re-create the in-situ stress state for the soil domain, in order to accurately simulate the real soil response when subjected to test loads. The continuum elements used to model the soil have to be prestressed and exposed to the pre-existing loading conditions, such as

the load due to the effect of gravity. In the numerical model developed for this study, two such loads are applied –

i) self-weight of the soil due to gravity

ii) self-weight of the caisson skirt (the top-cap of the caisson is described as weightless)

The analysis is conducted in terms of excess pore water pressure; thus, the initial pore pressure conditions are kept at 0kN/m^2 and the overburden effect of water can be ignored.

The self-weights due to gravity are simulated in ABAQUS using a distributed loading option in terms of their unit weights. The initial stress field is defined in terms of the effective unit weight of the soil. The vertical stress linearly increases with depth. The horizontal stress is expressed using the coefficient of earth pressure at rest, k_o. [Kulhawy, 1990]

$$k_0 = 1 - \sin(\varphi_{max})$$

where, φ_p is the peak friction angle, averaged at two-thirds the depth of the caisson skirt.

ABAQUS features an in-built geostatic step, which creates this required state of equilibrium between the initial stress field and the applied loads. The ABAQUS solver will iterate till a stress state is obtained which equilibrates the prescribed loads. [ABAQUS, 2013] This stress state will act as the initial stress condition for the subsequent loading condition – vertical uplift in the current study.

3.4.2. **Monotonic uplift**

The primary goal of this thesis is to study the response of a trailing suction caisson subjected to monotonic vertical uplift for a range of drainage conditions. This loading condition is simulated in the numerical model by controlling the pull-out rate of the caisson.

Saturated dense sand, when loaded slowly, allows sufficient time for the excess pore pressure developed due to the applied load to dissipate completely, causing a volume change in the soil. Thus, low pull-out rates are used to simulate drained loading. A sufficiently rapid pull-out will not allow the generated pore pressure to dissipate, leaving them entrapped within the soil pores. This creates an undrained loading condition. [Helwany, 2007]

A rate dependent load can be created in ABAQUS by utilizing its velocity-controlled boundary condition. This constraint was applied in the positive vertical direction, to the reference node for the rigid body of the suction caisson. The movement of this node in the horizontal direction, as well as rotation into the plane were constrained. This was done to prevent the lateral movement and the folding of the caisson, respectively, about its central axis. Constant pull-out rates ranging from 0.001mm/s to 1000mm/s [Thieken,2014] were investigated, till a specified heave relative to the caisson diameter was attained.

3.5. Single Element Simulations

3.5.1. **Hypoplastic soil model**

In order to overcome the drawbacks of the Mohr Coulomb soil model, the rate dependent Hypoplastic model as proposed by Wolffersdorff [Wolffersdorff ,1996] was

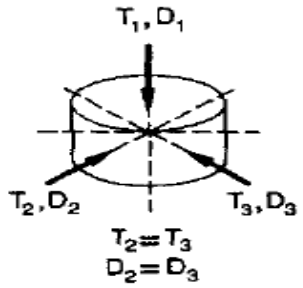

Figure 3-5 Boundary Conditions for triaxial test. Reprinted from [Wolfersdorff, 1996]

adopted in the last phase of this thesis. In order to assess the compatibility of the finite element model developed in the current study with the Hypoplastic soil model, single element simulations were performed in Abaqus with a material subroutine in FORTRAN [Felin, 2002]. The results demonstrated by the simulations were verified against available similar test results [Wolffersdorff ,1996], along with large scale experimental tests used by Wolfersdorff to validate his model. The tests were performed on Hochstetten sand, using model parameters from literature. The soil properties and the model parameters are listed in Table 3.9 and Table 3.10, respectively. The shearing mode adopted was triaxial compression, and the boundary conditions have been presented in Fig. 3.5. The elements were initially isotopically consolidated with three different stresses of 100kPa, 200kPa and 300kPa, and then subjected to axial compression till an axial strain of 10%. In an attempt to further improve the predictions of the model, parameter calibration studies were also conducted.

PROPERTY	VALUE
Soil density	2.65 g/cm^3
Maximum void ratio, e_{max}	0.95
Minimum void ratio, e_{min}	0.55
50% sieve passing diameter, d_{50}	20 mm
Coefficient of curvature, C_c	0.60

Table 3-9 Soil properties of Hochstetten sand

PARAMETER	VALUE
Critical state friction angle, ϕ_c	33
Granular hardness, h_s	1000 MPa
Exponent, n	0.25
Minimum void ratio, e_{do}	0.55
Critical void ratio, e_{co}	0.95
Maximum void ratio, e_{io}	1.04
Exponent, α	0.25
Exponent, β	1.5

Table 3-10 Hypoplasticity model parameters for Hochstetten sand

The permeability was derived using the Kozney-Carmen equation [Section 3.3.3] based on the initial void ratio, [Carrier, 2003] where C_{K-C} was set to 5, as is common practice [Thieken,2014; Carrier, 2003] and the specific surface area per unit volume of particles, S_0, was calculated with the assumption of uniform particle diameter of 20mm [Herle, 1999], using [Carrier, 2003]

$$S_0 = \frac{6}{D}$$

For a critical state friction angle of 33degrees, Wolf uses a value of 0.25 for the granular hardness exponent, n, whereas the current study achieved better results with a value of 0.28, as reported in [Herle, 1999] for the particular soil type. The maximum void ratio at zero pressure can be estimated to be 1.2 times the maximum void ratio. [Herle, 1999] Thus, for a maximum void ratio of 0.95, the e_{io} model parameter was set to 1.14 instead of 1.05. This estimation aided in improving the dilatancy prediction of the model. The influence of the altered parameters on the stress-strain response of the element is shown in Fig. 3.6.

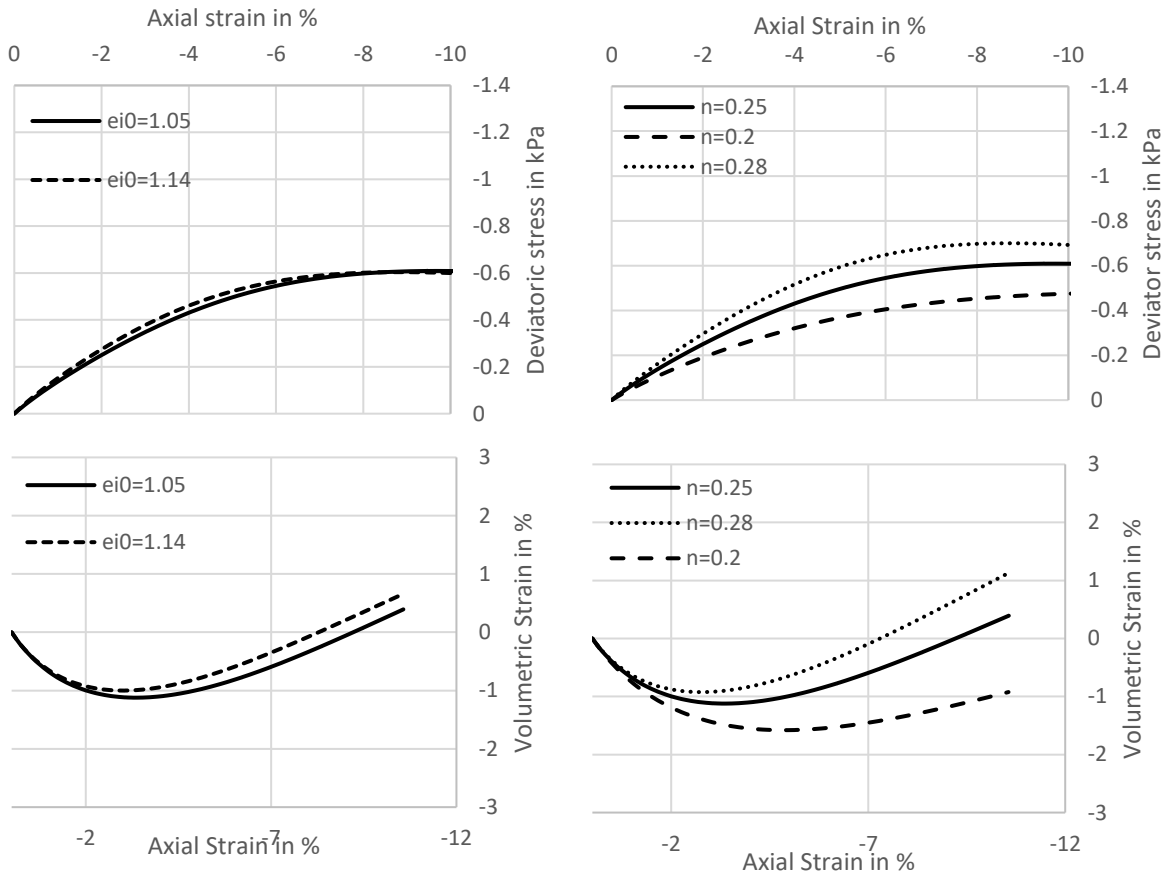

Figure 3-6 Hypoplasticity model parametric study for Hochstetten sand

The results of the consolidated-drained triaxial compression test is presented in Fig. 3.7 against the experimental results of the large-scale test and Wolf's numerical study. It can be clearly observed that the current FE model accurately mimics the soil response of both the cases. Following this success, the model was used with the Mohr Coulomb soil model, to compare the soil models at an element level.

3.5.2. **Mohr Coulomb failure model**

The tests were repeated using the Mohr Coulomb failure model, with the aim of comparing the two soil models at the element level.

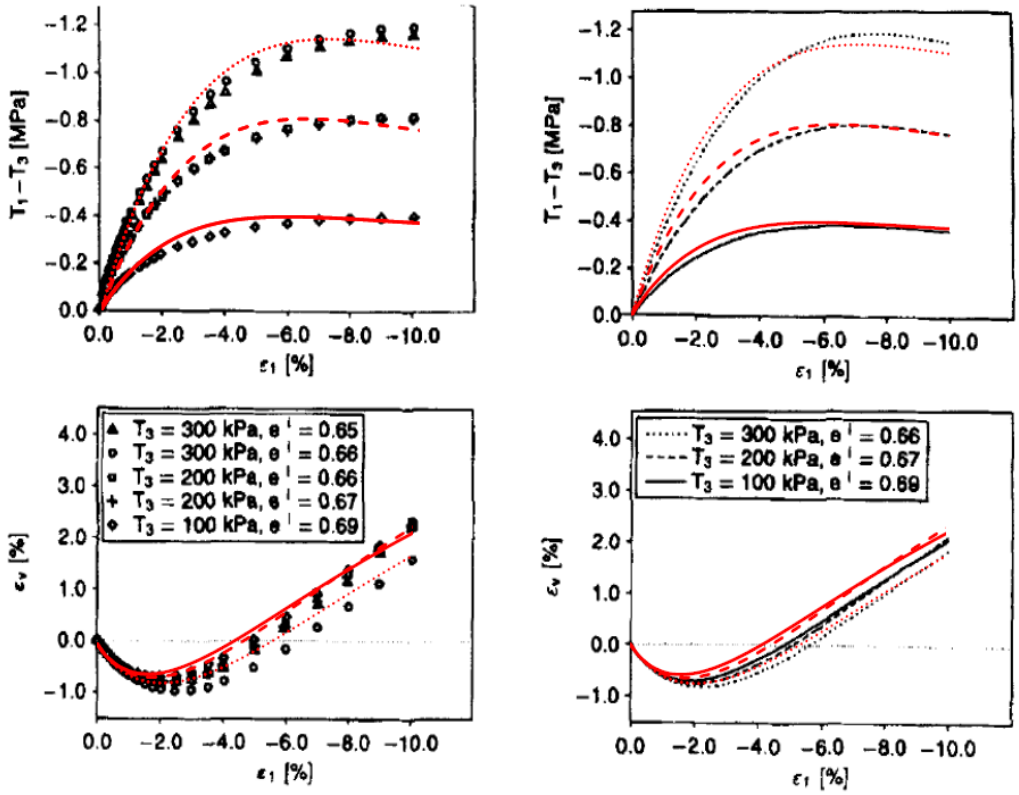

Figure 3-7 a) Results of large scale test vs current model predictions (red lines) b) Results of single element tests by Wolffersdorff (1996) vs current model predictions (red lines)

The Mohr Coulomb model parameters, peak friction and dilation angles, for Hochstetten sand, for the given critical state friction angle were attained using Bolton's equations, as described in Section 3.34., for each confining stress. The Young's modulus, *E*, is expressed in terms of the bulk modulus, K.

$$E = 3K(1 - 2\upsilon)$$

and, with a generic Poisson's ratio of 0.3 and K in terms of the model parameters as: [Herle, 1999]

$$K = \frac{1}{3}\frac{h_s}{n}\left(1 + \frac{1}{e}\right)\left(\frac{3p_s}{h_s}\right)^{(1-n)}$$

The derived Mohr Coulomb parameters have been presented in Table 3.11.

Model Parameter	Confining stress in kPa	
	100	300
Young's Modulus, E	10173.41 kPa	23042.029 kPa
Poisson's ratio	0.3	0.3
Peak friction angle	40.5	39.34
Peak dilation angle	9.0	7.9
Cohesion	1	1

Table 3-11 Mohr Coulomb model parameters for Hochstetten sand

The soil stress-strain behavior from the two soil models in the current FE model is presented in Fig. 3.8. The variations in the response is noticeably present. The perfectly-plastic nature of Mohr Coulomb prevents hardening after yield, as observed in the real soil behavior. The model also fails to capture the volumetric response observed in the soil.

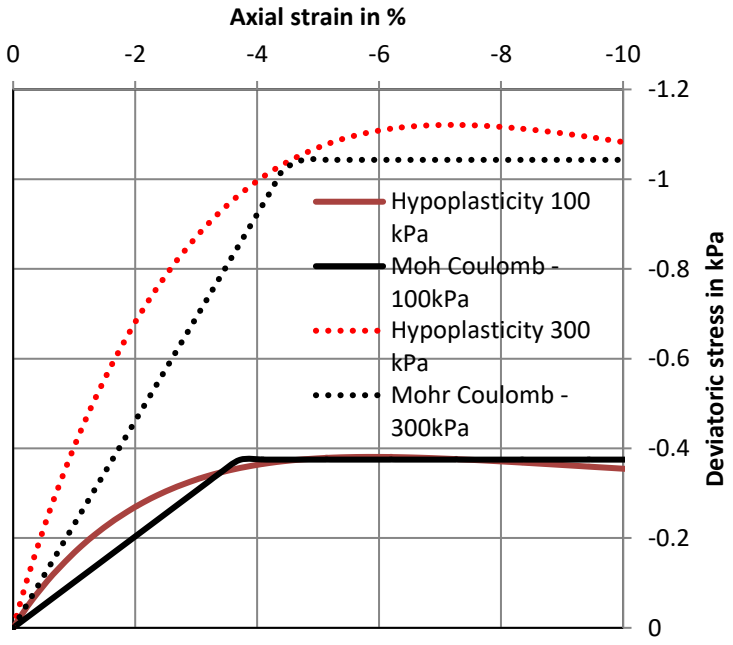

Figure 3-8 Results of Hochstetten sand by Hypoplasticity vs Mohr Coulomb

Table 3.12 summaries the friction angles and dilation angles attained from the four cases described above.

Despite such outcomes, the simulations ran with Mohr Coulomb for the suction caisson FE model, is successful in capturing the drained response of the soil. The problematic undrained behavior was not analyzed at an element level due to the lack of available physical test data to verify the outcomes against.

Confining stress in kPa	Peak friction angles		Peak dilation angles	
	Hypoplasticity model	Mohr Coulomb model	Hypoplasticity model	Mohr Coulomb model
100	40.96	40.5	17.17	9.0
300	41.81	39.94	23.75	7.9

Table 3-12 Summary of friction and dilation angles for Hochstetten sand from Hypoplasticity model and Mohr Coulomb model

It should be noted, that though convenient, single element results cannot be fully relied on since such tests fail to capture the inherent anisotropic behavior within the soil models. Also, they do not account for the interaction formulation of the actual physical problem.

4. RESULTS

This chapter presents the results obtained for the numerical analysis undertaken in this thesis. The simulations consider a monotonic vertical uplift on the trailing suction caisson of a multi-bucket jacket in dense sand, based on the formulations described in the previous chapters. This chapter has been categorized on the basis of the soil failure model adopted, and subcategorized according to the type of the soil tested. Simulations using the Mohr Coulomb failure model are denoted as the first phase of the project and those using the Hypoplastic failure model are denoted as the second phase of the project.

This chapter has been categorized on the basis of the soil failure model adopted, and sub categorized according to the type of soil tested.

4.1. Mohr Coulomb Soil Model

4.1.1. Generic Medium-dense sand

A suction caisson with a dimeter of 8m, skirt length of 4m (Aspect ratio = 0.5) and wall thickness of 50mm was modelled first. This will subsequently be referred as the base case for the tests done on the generic medium dense sand. The caisson was subjected to a tensile load applied at constant pull-out rates in the range of 0.001mm/s to 1000mm/s, till a targeted uplift of 2% of the diameter was achieved (=160mm for the base case), to simulate the drainage conditions of the soil. [Thieken, 2014] The pull-out behavior of the caisson and the excess pore pressure generation due to loading for each simulation for an initial void ratio of 0.5 has been described and compared with theoretically predicted responses in the following sections. The variation of the uplift capacity as a function of

the duration of loading; and effects of the caisson geometry are presented in Sections 4.1.1.3 and 4.1.1.4, respectively. In addition, outcomes of verification tests undertaken to validate the finite element model for the base case are described in Section 4.1.1.5, along with simple skirt pull-out hand calculations.

4.1.1.1. Load – displacement response for different loading rates

A plot with the variation of the uplift capacity with axial displacement for different loading rates has been presented in Fig. 4.1. The uplift capacity is obtained from ABAQUS as the total axial force acting on the loading node in response to the applied displacement. It can be observed from the figure that the capacity increases with the pull-out rate – towards an undrained condition, as expected on the basis of theoretical studies.

For a very slow pull-out rate of 0.001mm/s, a bilinear load-displacement curve develops. This indicates the response for a case where the resistance is du e to skin friction

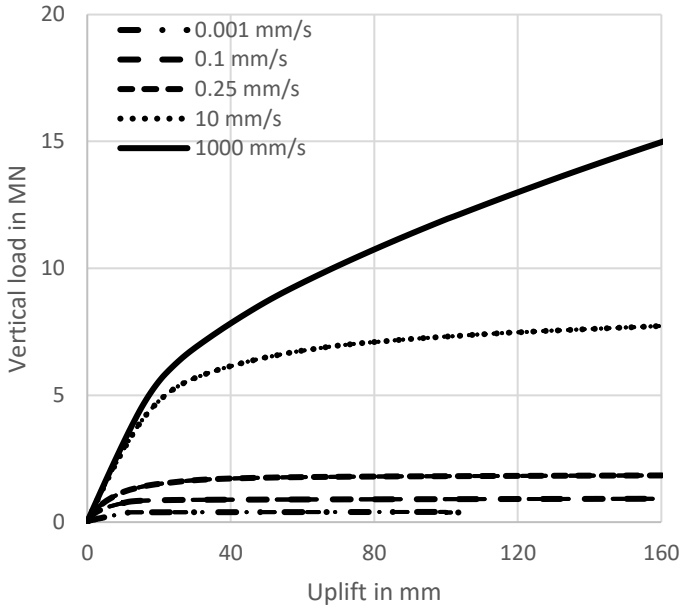

Figure 4-1 Load displacement curves for generic medium dense sand base case at different loading rates

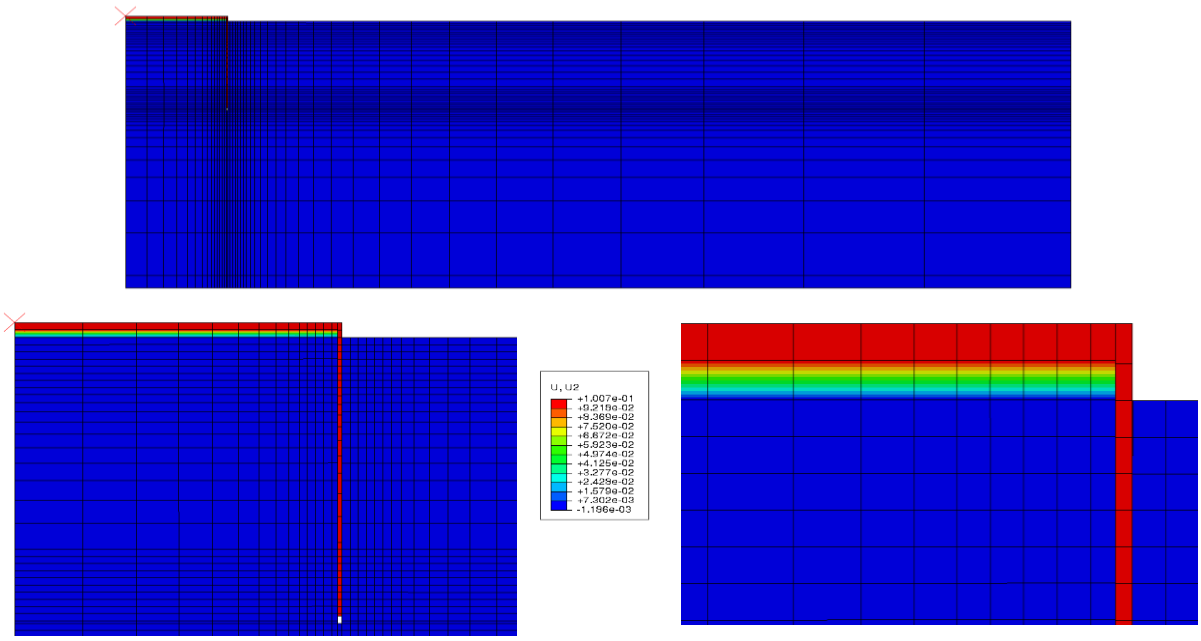

Figure 4-2 Vertical displacement contours for fully drained condition

only. [Thieken, 2014] As stated in Section 2.4.2, this is in accordance to the 'frictional' behavior described by Senders [Senders, 2008], specifying a purely drained condition. Fig. 4.2 shows contours of vertical displacement undergone by the finite element mesh, and its similarities with frictional behavior in Fig 2.11 can be observed, where only the caisson experiences any uplift, and soil displacement is negligible. This justified assigning a loading rate of 0.001mm/s to depict full drainage. Fig. 4.3 shows contours of shear stress developed on the inner and outer surface of the caisson skirt for the fully drained condition.

For faster pull-out rates, the vertical resistance increases drastically with the total axial displacement and the pull-out rate, though the initial stiffness response shows very small variation with the pull-out rate. For loading at rates above 10mm/s, the ultimate capacity was not attained even for 160mm axial displacement, indicating the requirement of very

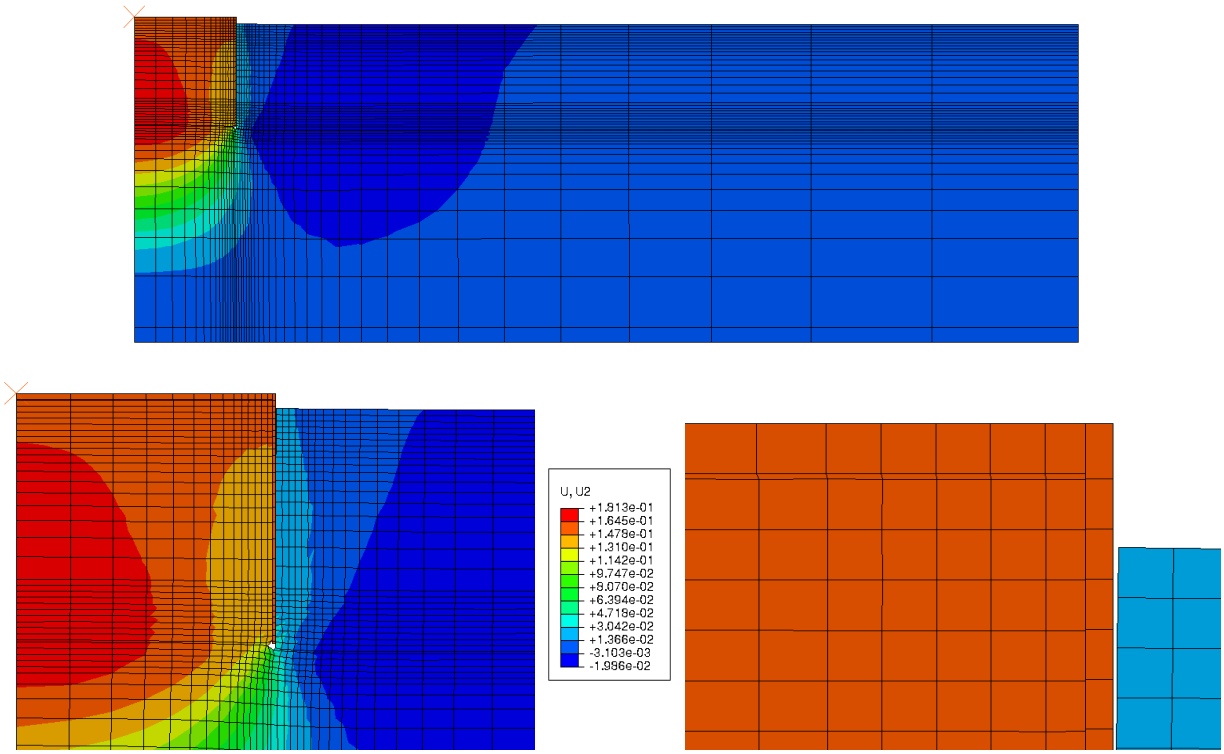

Figure 4-4 Vertical displacement contours for fully undrained condition

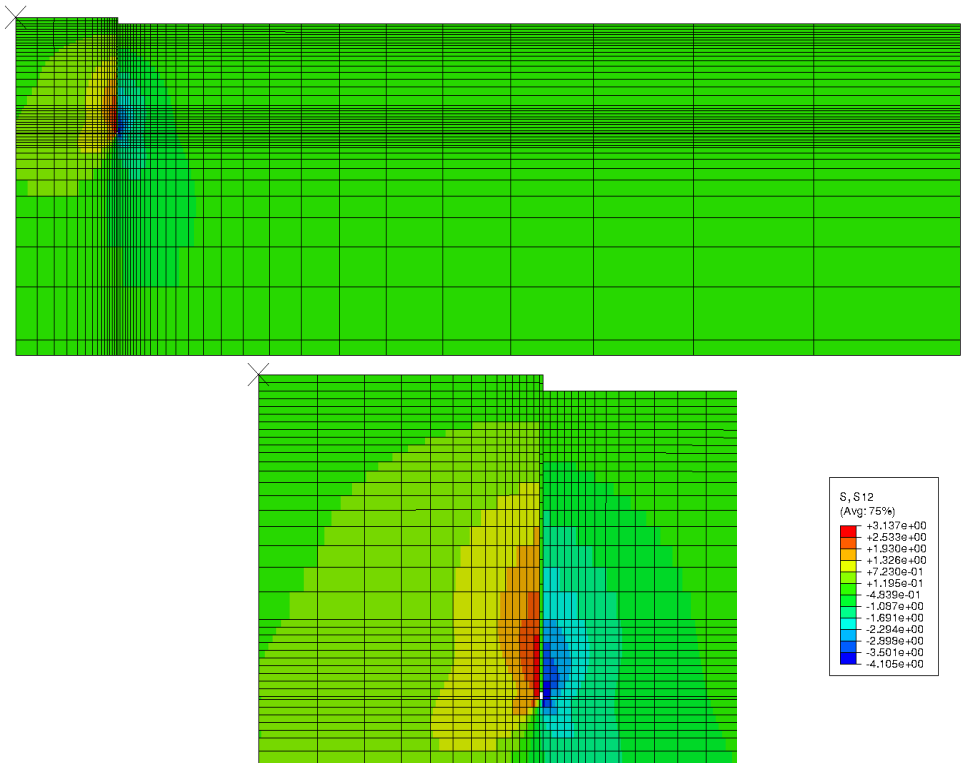

Figure 4-3 Shear stress contours for fully drained condition

large displacements for the full mobilization of capacity. Maximum loading rate was limited to 1000mm/s since a further increase in the rate brought about negligible difference to the load-displacement curve thus justifying the assignment of 1000mm/s to specify a fully un-drained condition. The response of the soil is presented in Fig. 4.4 in terms of contours of total vertical displacement for a fully undrained case. The soil inside the caisson demonstrates vertical displacement as well along with the caisson. This reveals a 'reverse end bearing' behavior, as described in Section 2.4.2 and illustrated in Fig 2.11. The corresponding contours of shear stress show negligible development along the inner skirt of the caisson. (Fig. 4.5)

4.1.1.2. Suction pressure development

The behavior of the suction generated with respect to the applied loading follows a similar trend to that of the load-displacement curve as described in the previous section.

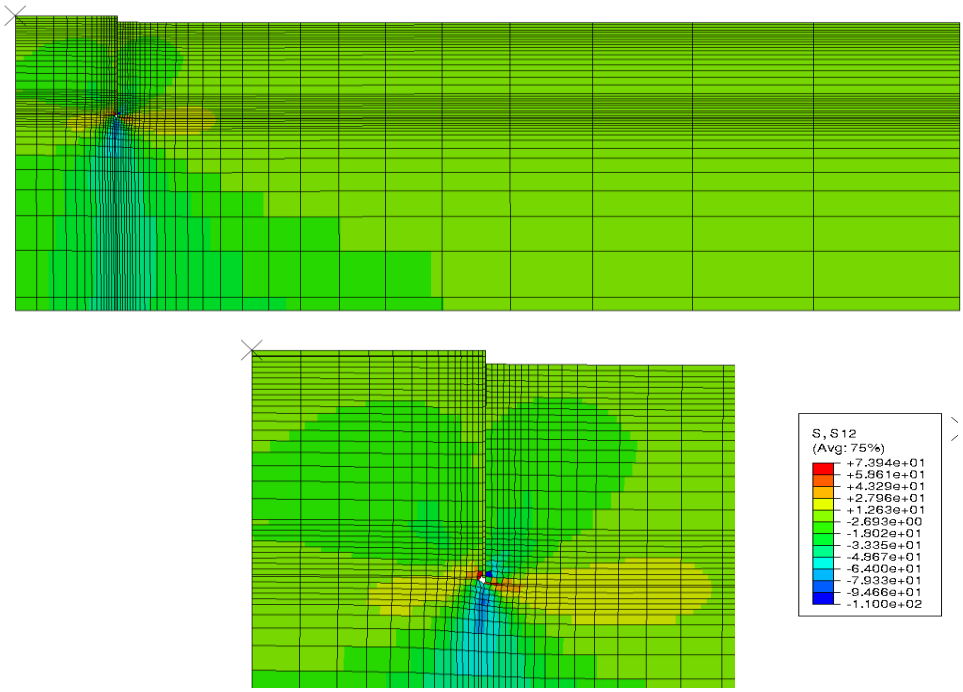

Figure 4-5 Shear stress contours for fully undrained condition

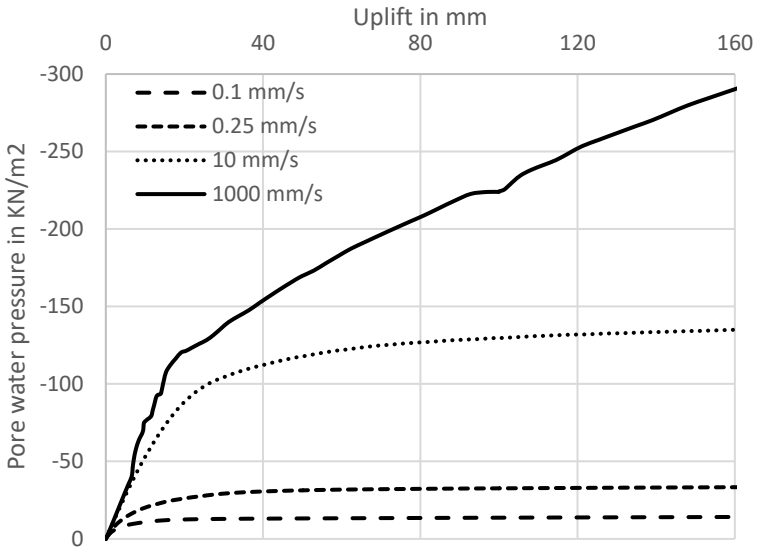

Figure 4-6 Pore pressure vs axial displacement curves for the generic medium dense sand base case for different loading rates

Fig. 4.6 shows the variation of suction pressure with total vertical displacement for the different loading rates. The suction pressure was attained by recording the pore pressure behavior of an element right below the cap of the suction caisson. The suction resistance can be calculated as the product of the pressure and the area of the cap, since the suction pressure is uniformly developed across the cap.

For the fully drained loading condition (0.001mm/s), negligible suction is generated, since the slow loading provides sufficient time for the water to flow into the caisson cap-soil interface. This is demonstrated in the behavior of the water elements adopted below the caisson cap. Fig 4.2 c. shows the expansion of the water elements, representing the creation of a gap, which is equal to the vertical displacement undergone by the caisson (and thus, no vertical displacement occurs in the soil). The pore pressure contours in Fig. 4.7 a. also show the creation of no suction.

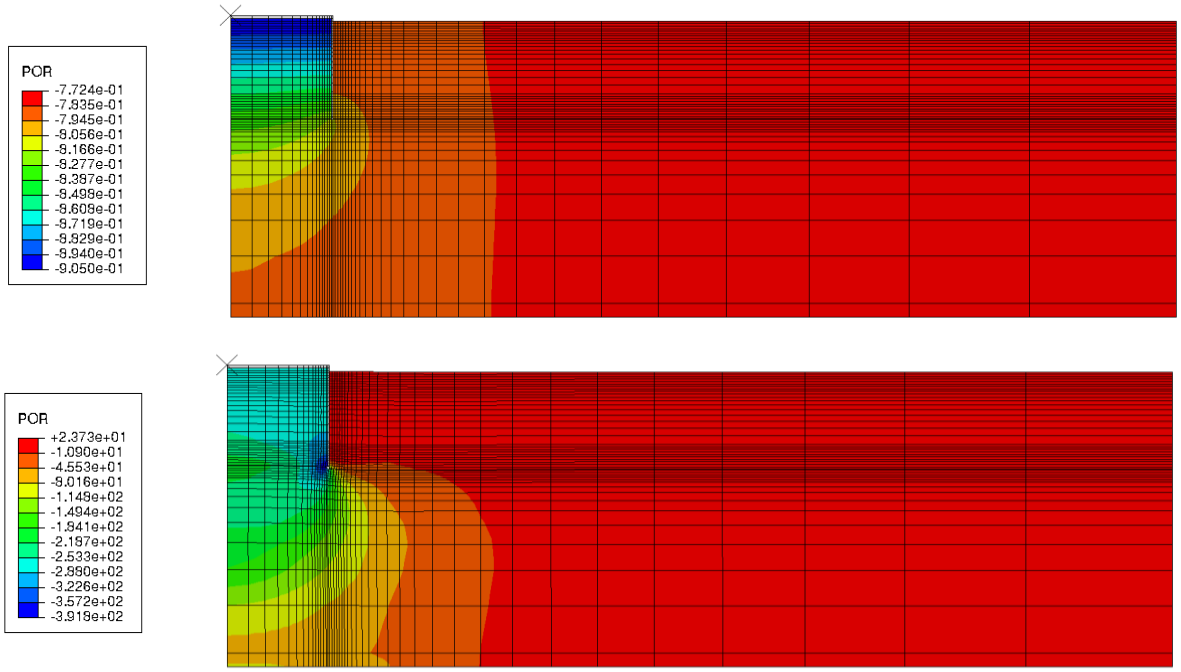

Figure 4-7 Pore pressure contours a) Fully drained condition b) Fully undrained condition

The excess pore pressure contours for the fully undrained condition show very small pore pressure dissipation within the caisson. (Fig. 4.7 b.) Thus, significant suction pressure is available at caisson-soil interface beneath the caisson top cap. This prevents the expansion of the water elements (Fig. 4.4 c.) as was observed in the case of drained loading, and subsequently causes the entire soil within the caisson to undergo vertical displacement, thus contributing to the vertical capacity, as noted in Section 4.1.1.1. This in turn also causes the soil outside the caisson to move in, thus subjecting them to a vertical downward displacement. The net vertical displacement of the soil inside and outside the caisson for a fully undrained condition should be zero, since no volume change is allowed for a fully undrained analysis. This is verified subsequently in Section 4.1.1.5.

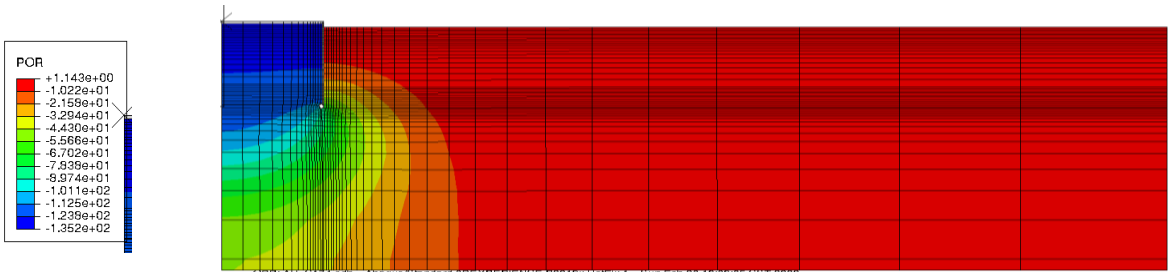

Figure 4-8 Pore pressure contours for partially drained condition

Partial drainage conditions exhibit intermediate suction pressure response. The loading rate allows partial dissipation of the excess pore pressure. Fig. 4.8. represents the pore pressure contours for a loading rate of 10 mm/s, considered to demonstrate partial drainage conditions, where dissipation occurs majorly within the caisson. Thus, the soil undergoes vertical displacement but it is less than the caisson displacement. This can also be observed in the behavior of the water elements adopted. Fig. 4.9 shows the expansion of the water layer for the different loading rates. As the rates are increased, expansion or the formation of gap is prevented due to suction, thus instigating greater uplift of the soil within the caisson.

Increasing the pull-out rate thus causes an increase in the pore-pressure difference inside the bucket and outside the bucket, resulting in an increase of the effective stress.

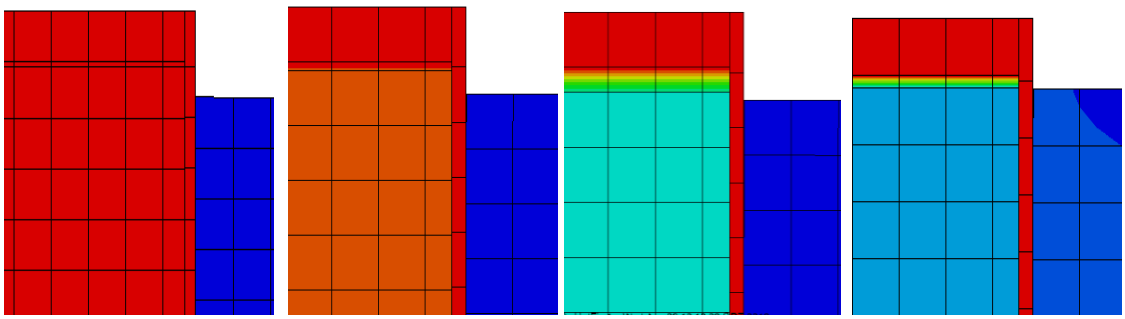

Figure 4-9 Behavior of water element layer as soil transitions from undrained to drained condition

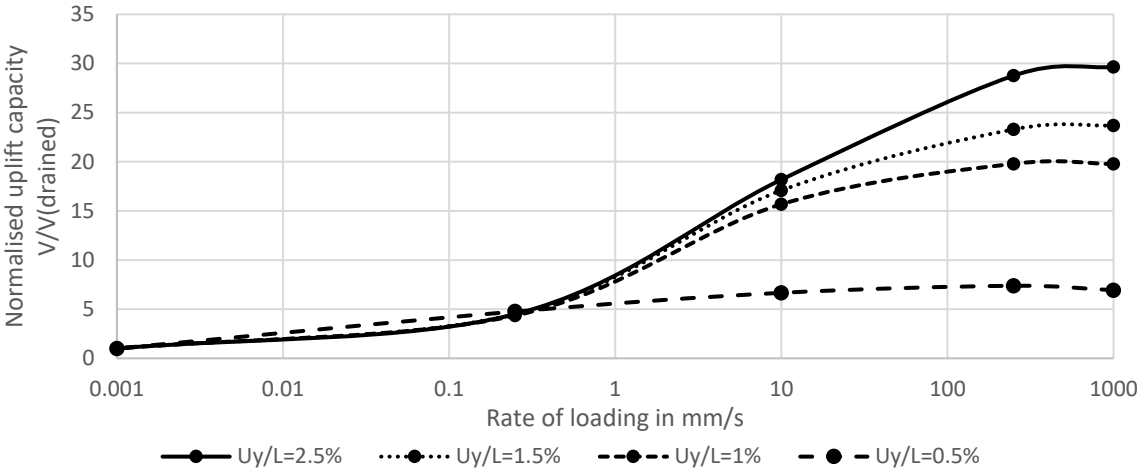

Figure 4-10 Transition curve for the generic medium dense sand base case in terms of loading rate

4.1.1.3. Transition Curve

Fig. 4.10 shows the variation of the vertical load required for the specified axial displacements as the system transitions from a state of complete drainage to an undrained state, presented as a function of the loading rate. The diagram further substantiates the trends established in the above sections in regard to the transition from drained to undrained behavior.

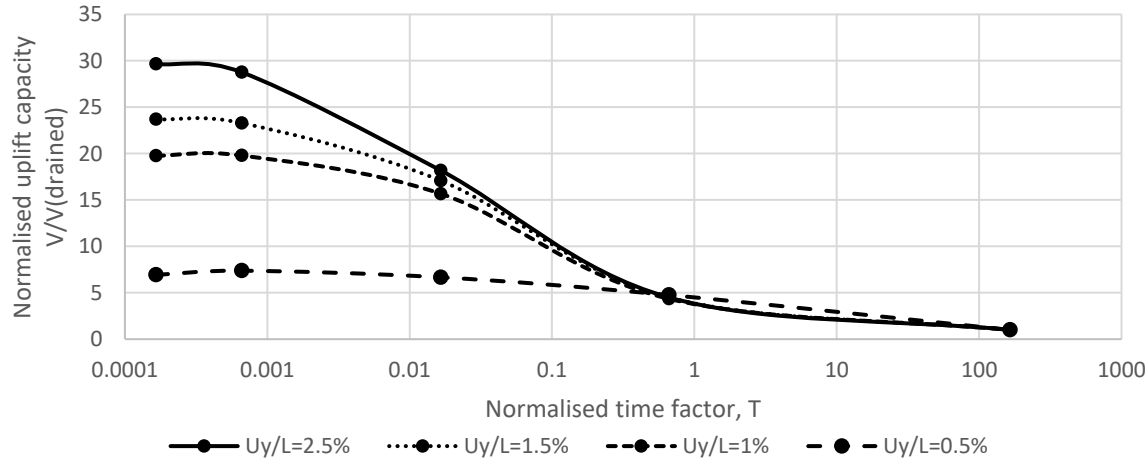

Figure 4-11 Transition curve for the generic medium dense sand base case in terms of time factor

The vertical loads required for an uplift of 2.5%, 1.5%, 1% and 0.5% of the diameter of the caisson are presented. For the smaller displacement (0.5%), only a slight increase in the vertical load with an increase in the loading rate is observed. This is in concurrence with the load displacement curve (Fig 4.1) in Section 4.1.1.1, where the initial stiffness response of the soil showed very small variation with the loading rate. The response of the larger displacements show a drastic increase in the capacities only after the loading velocity of 1 mm/s, and negligible difference for velocities lower than 0.5 mm/s, indicating complete drainage. The diagram also demonstrates again the requirement of large vertical displacement for the full mobilization of the faster pull-out capacities.

Fig.11 shows a similar variation of capacity with the drainage condition of the soil expressed in terms of a normalized time factor, T. [Whyte]

$$T = \frac{c_v t}{D^2}$$

where the coefficient of consolidation of the soil is given by: [Davis, 1968]

$$c_v = \frac{kE}{\gamma_w} \frac{(1-\vartheta)}{(1-2\vartheta)(1+\vartheta)}$$

calculated with the value of the Young's Modulus at two-thirds the caisson length.

The curve attained is a mirror image of Fig. 4.9, since a higher quantity of the time factor indicates a longer loading period, and thus a transition into a state of complete drainage.

4.1.1.4. Parametric Studies

To investigate the influence of the caisson geometry on the undrained capacity and the drainage transition curves, caissons with different aspect ratio and skirt lengths were

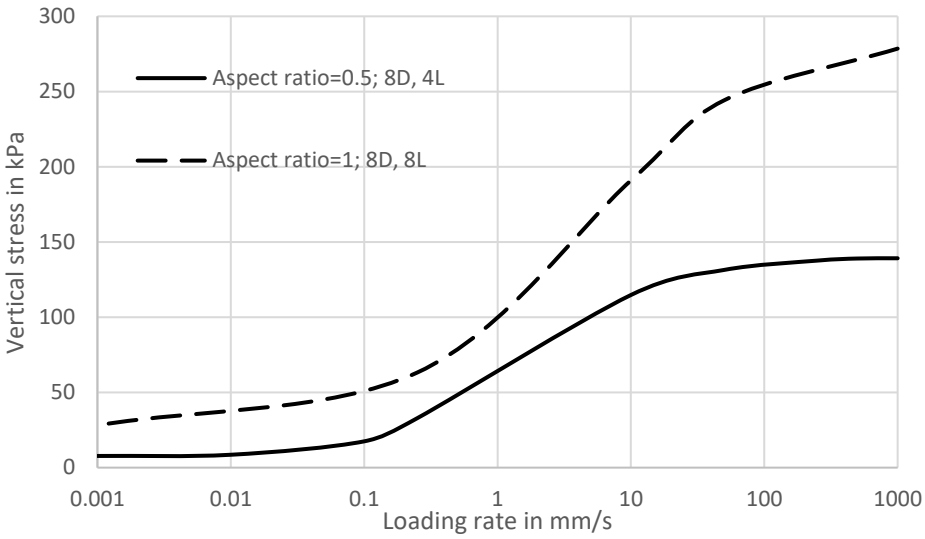

Figure 4-12 Transition curves for different aspect ratio

tested. The drainage transition curves, for capacities at vertical displacements of 2% the diameter of the caisson, with the different geometries are presented in Fig. 4.12.

Fig 4.12 shows transition curves attained from altering only the skirt length on the suction caisson. A constant increase in the capacity is observed with an increase in the length (also an indication of increase in aspect ratio) for all loading rates. An increase in the skirt length will lead to larger frictional resistance to be mobilized along the depth, thus producing a higher drained capacity. The increase in the undrained and the partially drained capacities can be attributed to the increase in the seepage path and the increase in the volume of soil within the caisson. [Thieken, 2014] A longer seepage path effects the drainage condition of the soil since it reduces the amount of pore pressure dissipation for a given time, and in turn increasing the suction pressure and thus the capacity. The additional self-weight of the volume of the soil within a longer caisson subjected to uplift due to suction will subsequently lead to an addition in the uplift capacity.

4.1.1.5. Verification Studies

4.1.1.5.1. Analytical drained capacity

The drained tensile capacity was determined using the expressions proposed by Houlsby and Byrne [2005], as stated in Section 2.4.3. The following table (Table 4.1) presents the outcome and its comparison with the capacity produced by the FEA at the loading rate of 0.001mm/s:

METHOD	DRAINED CAPACITY	PERCENTAGE OF ERROR
Analytical [Houslby, Byrne]	394.45 KN	1.96%
Finite element model	402.19 KN	

Table 4-1 Drained capacity for generic medium dense sand base case

The 1.96% error in the finite element study can be considered well within acceptable limits, and thus the study with the model was carried forward.

4.1.1.5.2. Single element behavior for undrained analysis

The undrained behavior of a suction caisson in dense sand subjected to an axial load is complicated. It is controlled by the dilation of the soil and the loading rate. [Byrne,

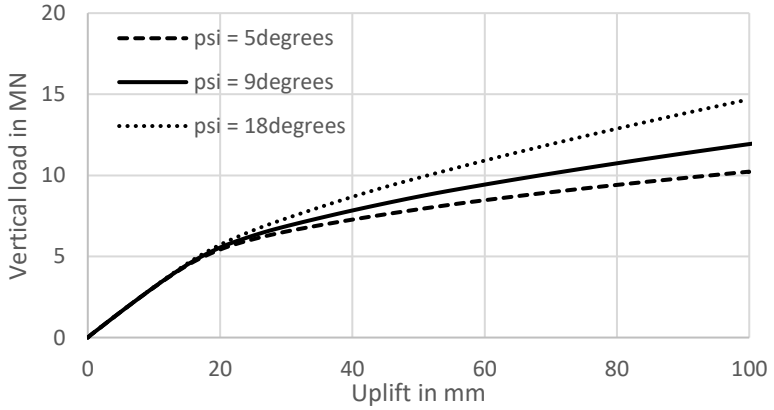

Figure 4-13 Load displacement curve for different dilation angles at fully undrained condition

2000] To assess the finite element model created in this study in its ability to capture the dilatant response of dense sand, the soil behavior at three different locations were studied, each for three angles of dilation, at the loading rate of 1000mm/s. The subsequent load displacement curve for the model is presented in Fig. 4.13, which shows an increase in capacity for higher dilation angles. This is in accordance with the established dense sand behavior, as described in Section 2.1.3. Three single elements were selected at different parts of the soil mesh, as shown in Fig.4.14. Their stress and strain components over the loading period were obtained from Abaqus, and their stress paths were calculated using the Mohr Circle method.

Point A is an element of soil selected within the caisson. The corresponding stress path is shown in Fig. 4.15 a. The inclination of the path towards the right indicates a purely

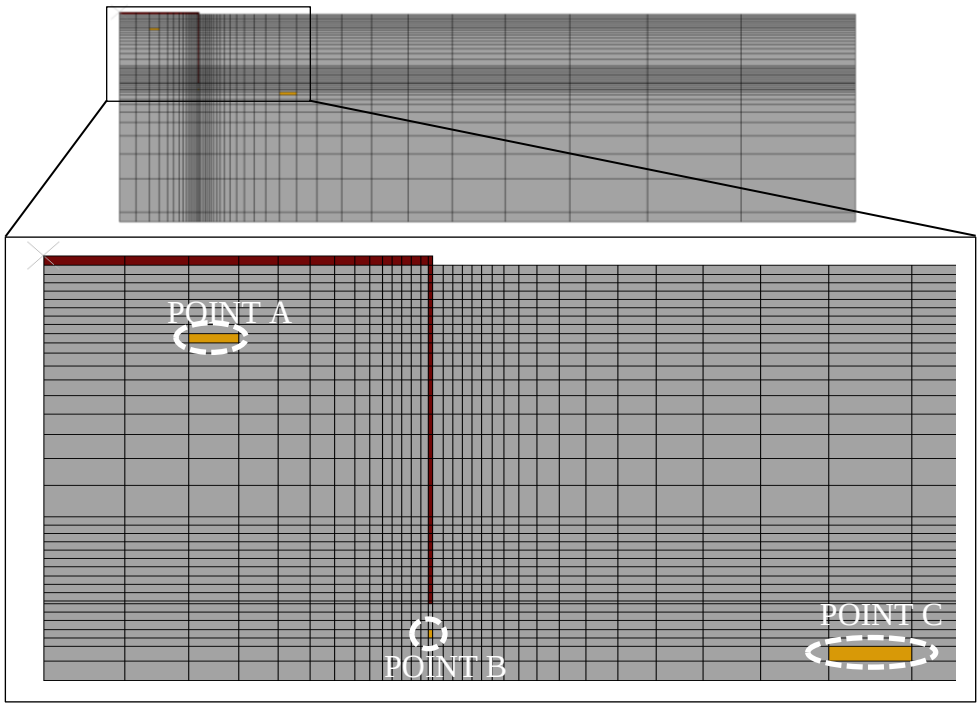

Figure 4-14 Location of elements selected on the mesh

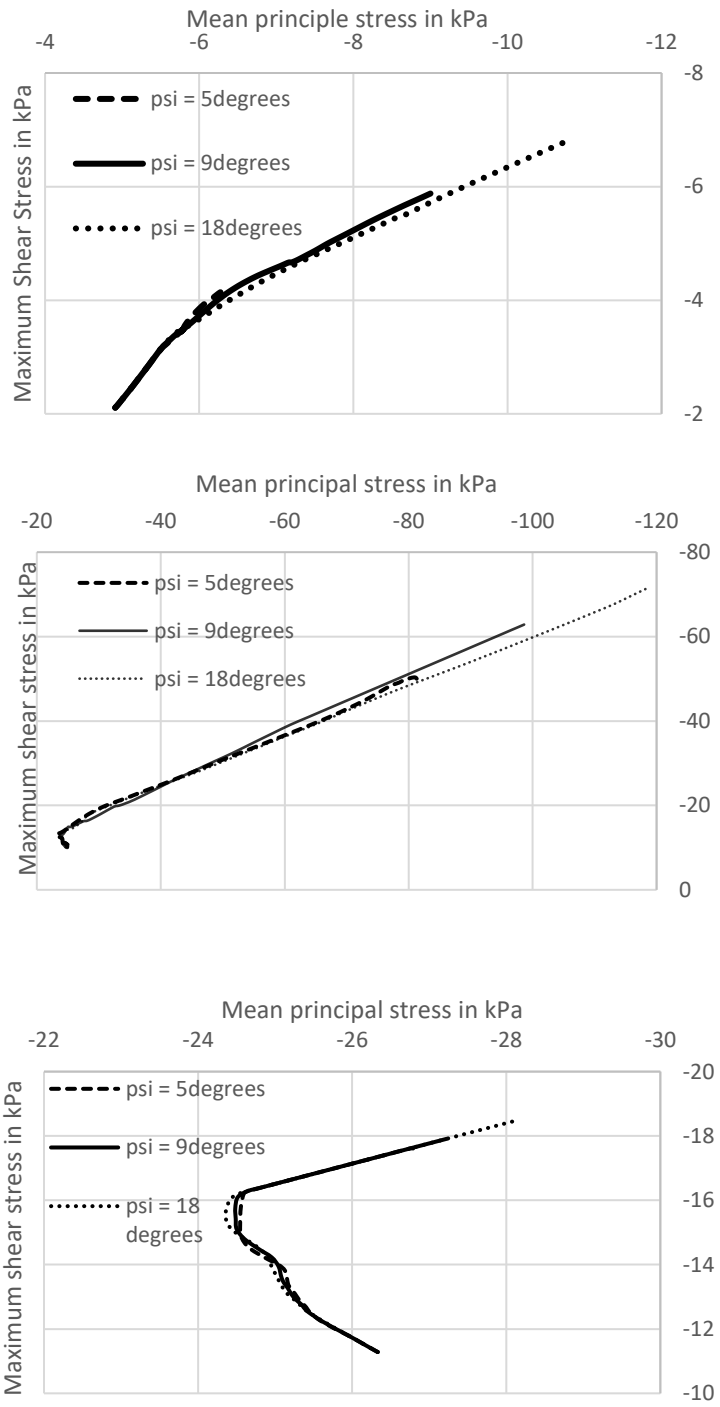

Figure 4-15 Single element response for a) Point A b) Point B c) Point C

dilative response for the element. This behavior corresponds to the high suction pressure at the location.

Point B is located a few elements below the tip of the caisson skirt. The corresponding stress path attained is shown in Fig. 4.15 b. The path follows a dilative behavior, with the angles of dilation provided dictating the dilation amount.

Point C is a soil element selected at the far field region. Its corresponding stress path is shown in Fig. 4.15 c. at the tip of the caisson. The element demonstrates an initial compressive behavior, becoming dilative with continuing loading. This is behavior is typical for dense sand.

4.1.1.5.3. Stress profile

The vertical stress and shear stress profile along the inner and the outer walls of the caisson skirt for a fully drained condition were obtained from ABAQUS. (Fig. 4.16 and Fig. 4.17) A rise in the stresses were observed nearer the tip of the skirt. To check the accuracy of the shear response predicted by the model using Coulomb's frictional law,

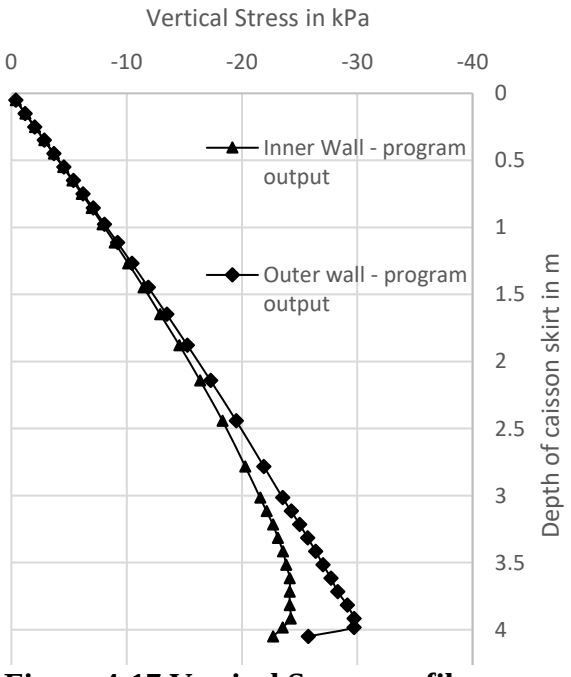

Figure 4-17 Vertical Stress profile

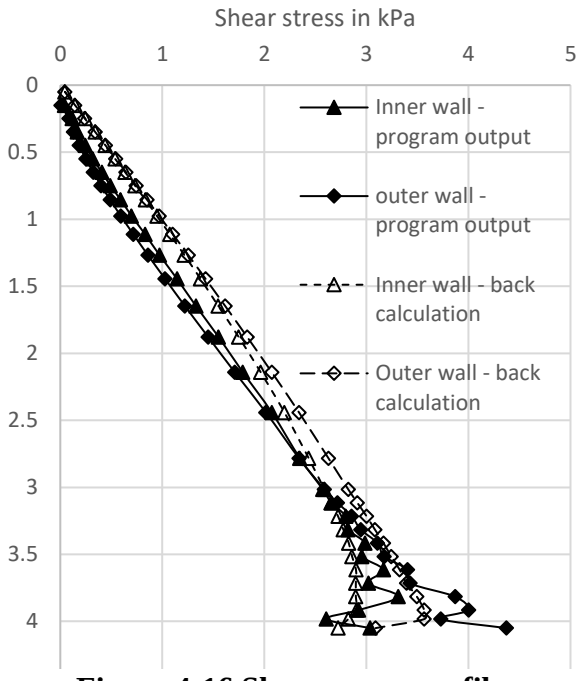

Figure 4-16 Shear stress profile

back calculations were performed using the vertical stress output, and the initial coefficient of earth pressure at rest and the coefficient of friction fed into the program. The calculated shear stress profile was compared with the output from the program, as shown in Fig. 4.17.

The shear stress profile along the wall, before the tip, attained from back calculations are slightly higher than the ones provided by the software, but follow a consistent trend and thus considered acceptable. The output values at the tip, though in the vicinity of the calculated ones, are follow an irregular trend. This may indicate a possible problematic zone.

4.1.1.5.4. Undrained volumetric response

For an undrained analysis, the volumetric strain should be zero. The suction generated due to short term loading will lift the soil inside the caisson, and subsequently cause the soil outside to move in, as explained in Section 2.4.2.

In the current study, for the ease of calculation, a uniform circumferential soil displacement response is assumed. The overall volumetric strain was then determined by estimating the vertical upward and downward displacement of the top layer of soil and multiplying it by their corresponding circumferential area.

From the axial displacement contours for a loading rate of 1000mm/s, (Fig. 4.4 a) the following values were attained:

Soil volume undergoing expansion	10.163 m^3
Soil undergoing compression	9.723 m^3
Overall volume change	0.44 m^3
Percentage error	4.32%

Table 4-2 Volumetric response for a fully undrained case

An overall expansion in the volume of the soil mass was calculated, indicating the presence of an error in the model. Despite this, the model was accepted due to the relatively small value of the error with respect to the total volumetric expansion applied to the soil mass inside the caisson due to the suction generated.

4.1.1.6. Conclusion

The aim of conducting the numerical analysis with the Mohr Coulomb failure model on a generic medium dense sand, was to develop and assess the performance of a coupled finite element model in capturing the soil's tensile behavior when subjected to a range of drainage conditions. Following the outcome of the trend of the load displacement plots and the transition curve in accordance with the expected theoretical response, and the validation tests producing reasonable results, the finite element model was assessed to be acceptable.

4.1.2. UWA Superfine Silica Sand

The second stage of the project was to conduct the same analysis-suction caisson subjected to monotonic tensile loading- using the Mohr Coulomb failure model on the second soil type-UWA Superfine Silica Sand. Availability of outcomes of previous studies with the same testing conditions, eased the process of assessing the validity of the numerical formulation adopted for the present thesis. Successful numerical simulations conducted by Scott Whyte [Whyte] using a bounding surface soil model provided a base to evaluate the accuracy of the Mohr Coulomb model in predicting the partially drained to undrained behavior of dense sand.

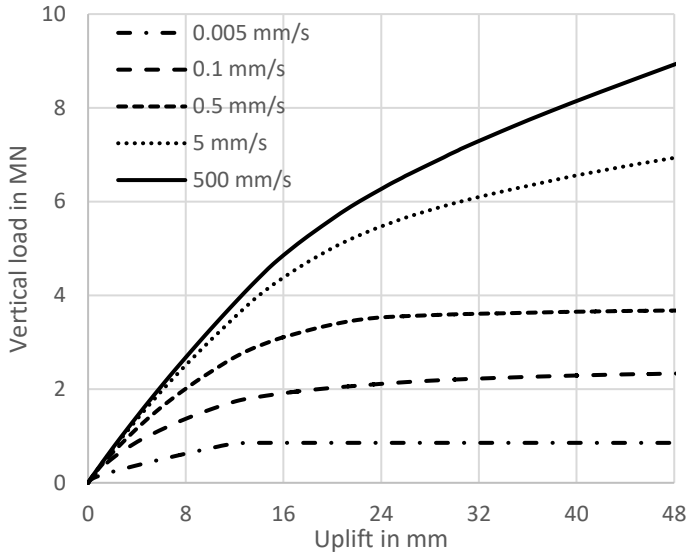

Figure 4-18 Load displacement curve for UWA Superfine silica sand base case at different loading rates

A suction caisson of equal diameter and skirt length of 6m (Aspect ratio = 1), with wall thickness 30mm was modelled as the base case for this soil type. Simulations were created for tensile loading rates in the range of 0.001mm/s to 1000mm/s, till the caisson reached a targeted uplift of 1% of its skirt length (=48mm for the base case). [Scott] The following sections present the results of the simulations for an initial void ratio of 0.535 and permeability of 1.09E-04 m/s.

4.1.2.1. Load-displacement and pore pressure response for different loading rates

The load vs displacement figures for the range of loading rates are shown in Fig. 4.18. The trend of increase in resistance with the increase in loading rate and suction is consistent with the first phase of the current study as well with the findings of earlier studies conducted.

The drained ultimate capacity was predicted to be 852.47 KN. Comapred to the analytical value using Houlsby's method (951.03 KN), it results in an error of 10.3%.

4.1.2.2. Comparison with previous studies

The simulations were compared against results of Centrifuge model tests conducted by Senders [Senders, 2008] and Bienen [Bienen, 2018] for similar loading conditions, and against outcomes of a numerical study conducted by Whyte [Whyte] using a bounding surface sand model.

4.1.2.2.1. Centrifuge tests by Senders [Senders, 2008]

Senders conducted various centrifuge model tests to understand the behavior of tensile loading in sand. His tests labelled Test 6-2 and Test 6-3 have been referred to in the current study for comparison. [Senders, 2008] The tests were conducted on UWA Superfine Silica sand, with an initial void ratio of 0.535 and permeability of 1.09E-04 m/s, with model dimensions resulting in equivalent caisson dimensions equal to the base case in the current phase of the study. These tests were also adopted by Whyte in his numerical

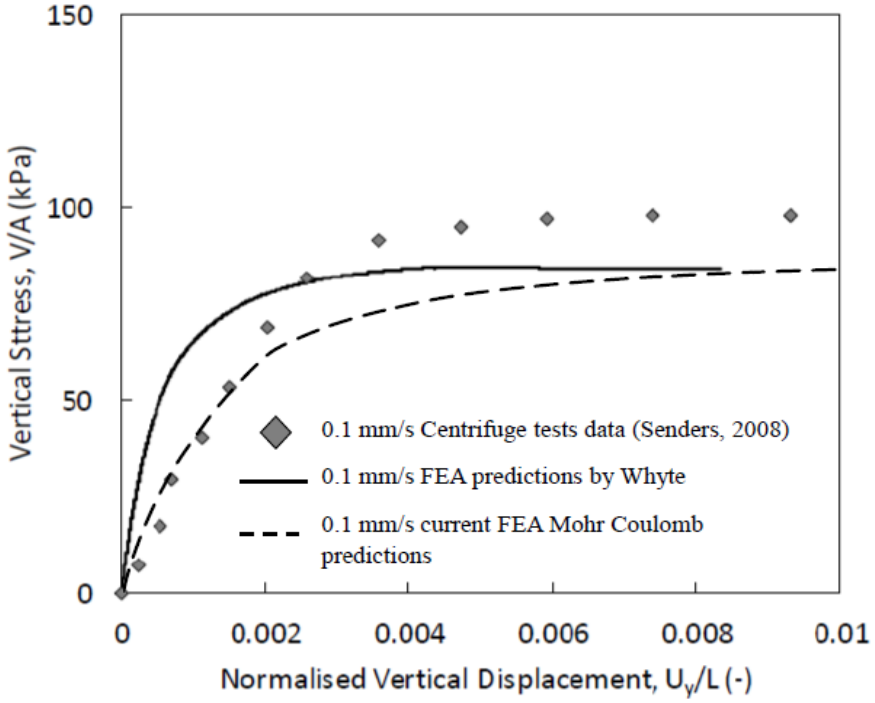

Figure 4-19 Load displacement curve for 0.1mm/s for UWA Superfine Silica Sand

analysis to validate his constitutive model, thus the following sections provide a comparison between the centrifuge results from Senders and numerical predictions by Whyte's bounding surface model and the current finite element model using Mohr Coulomb for specified loading rates.

4.1.2.2.1.1. Comparison with Test 6-2

Test 6-2 was subjected to a loading rate of 0.1mm/s, designed to replicate drained behavior. The load-displacement response is presented in terms of vertical tensile stress vs a normalized displacement. Fig. 4.19 contains the responses from the three cases compared. From inspection, reasonably good matches to the experimental response are obtained from both the numerical studies. Although the current study with the Mohr Coulomb model slightly underpredicts the ultimate capacity, it provides an accurate prediction for the initial soil stiffness response, where the bounding surface model makes stiffer predictions.

he vertical displacement contours (Fig. 4.20) for the present simulation shows an uplift in the soil mass suggesting a not fully drained condition. The expansion in the water

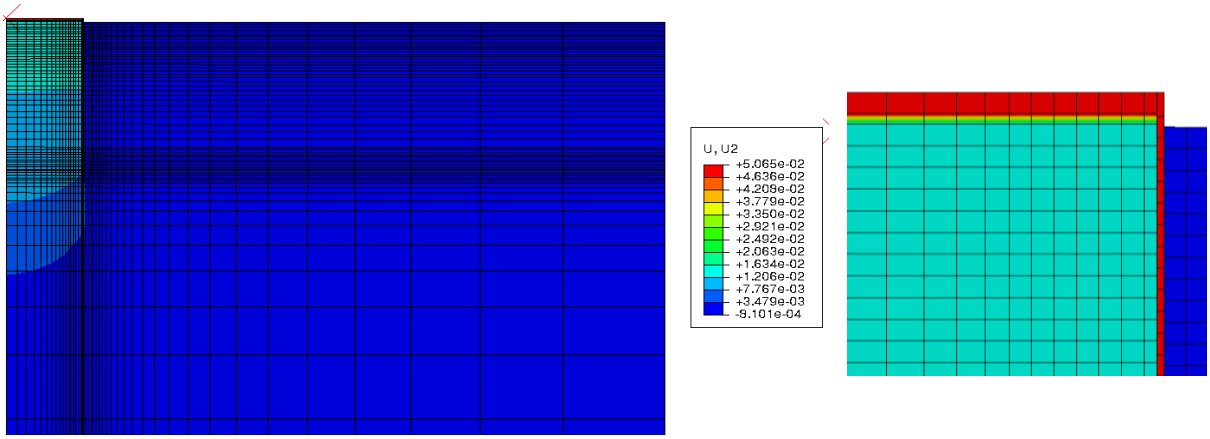

Figure 4-20 Displacement contours for UWA Superfine Silica Sand at 0.1mm/s

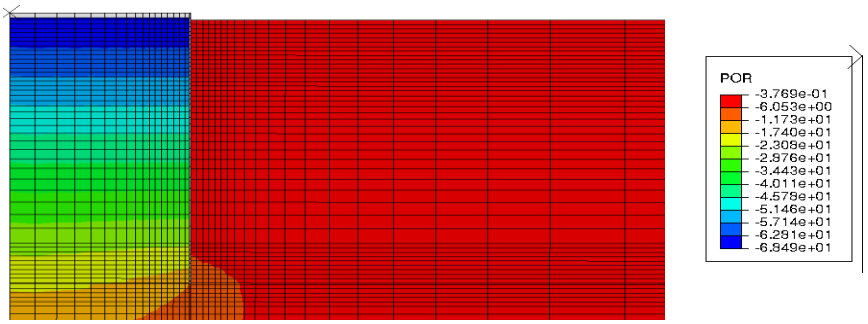

Figure 4-21 Pore pressure contours for UWA Superfine Silica Sand at 0.1mm/s

elements adopted can be observed to be less than the uplift of the caisson. The contours of pore pressure generation (Fig. 4.21) present suction dissipating within the caisson, thus indicating a partially drained condition instead.

4.1.2.2.1.2. Comparison with Test 6-3

Test 6-3 was subjected to a higher loading rate of 0.5mm/s to represent a partially drained condition.

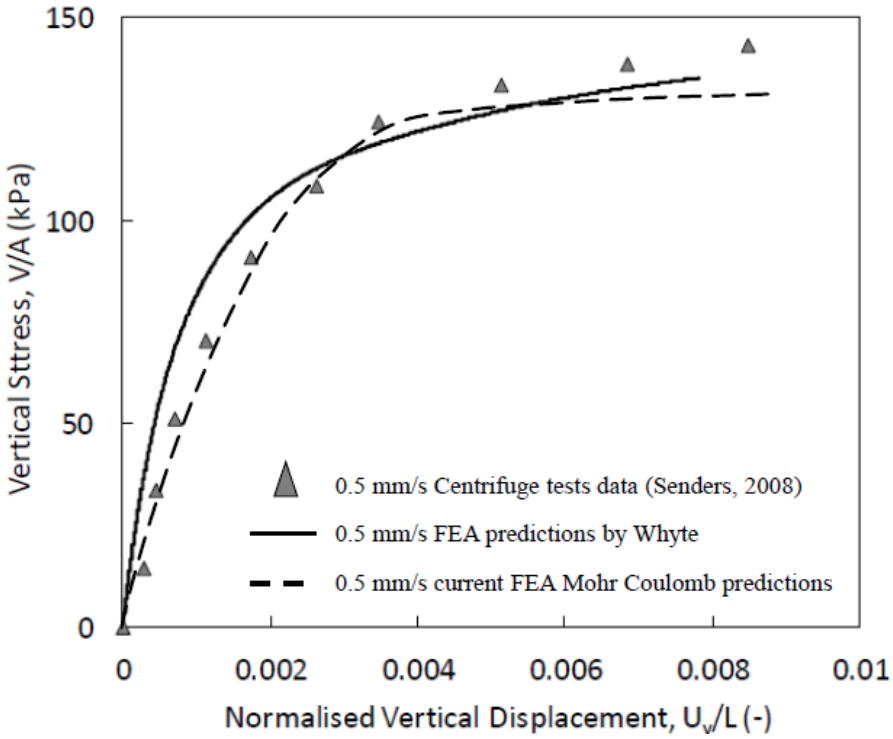

Figure 4-22 Load displacement curve for 0.5mm/s UWA Superfine Silica Sand

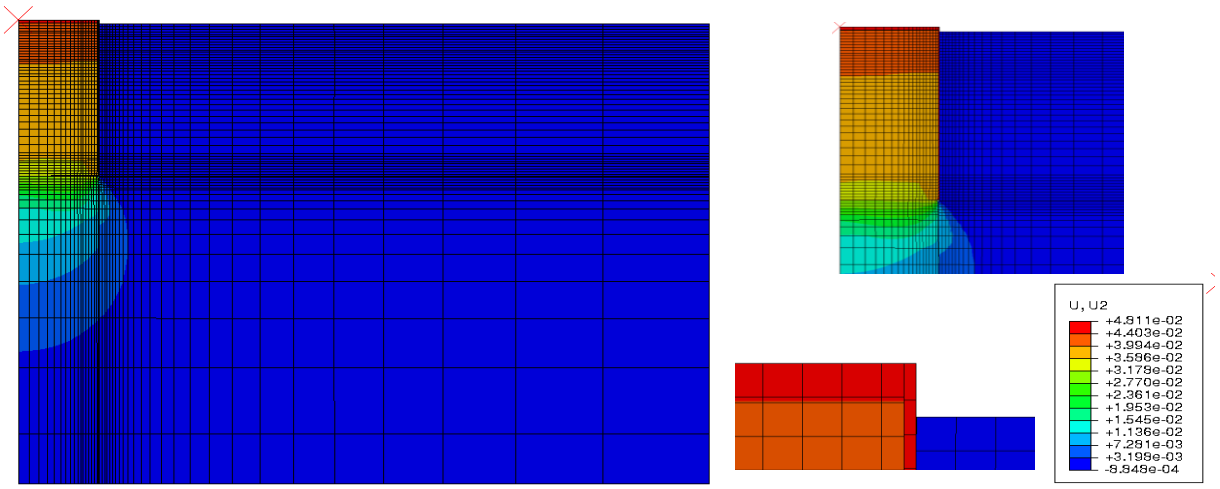

Figure 4-23 Displacement contours for UWA Superfine Silica Sand at 0.5mm/s

The tensile stress vs normalized displacement curve (Fig. 4.22) for the current loading rate replicate the earlier trend – initial stiffness response is better and accurately predicted by the current FE model with Mohr Coulomb, but ultimate capacity is underpredicted, though well within reasonable error limits.

The displacement (Fig. 4.23) and pore pressure (Fig. 4.24) contours from Abaqus for the current loading rate demonstrates behavior consistent with partially drained conditions.

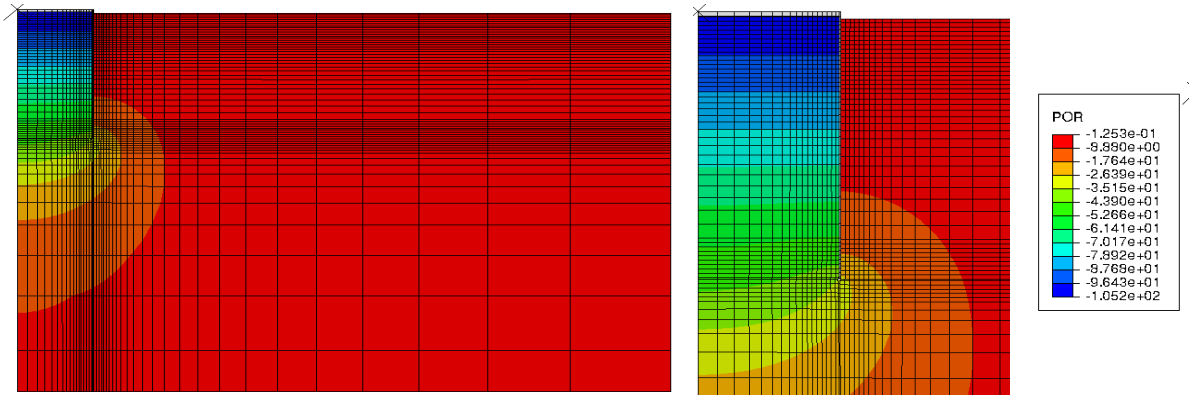

Figure 4-24 Pore pressure contours for UWA Superfine Silica Sand at 0.5mm/s

4.1.2.2.2. Centrifuge tests by Bienen [Bienen, 2018]

A series of centrifuge experiments were conducted to investigate the response of suction caissons in dense sand by Bienen. [Bienen, 2018] The test labelled Test 6-1 have been referred to in the current study as a basis of comparison. The test was conducted on Baskarp Sand, whose particle size distribution is similar to UWA Superfine Silica Sand, and thus the same soil properties can be used. [Whyte] The test was conducted at a loading rate of 3mm/s, representing partially drained to undrained condition, with an initial void ratio of 0.57 and permeability of 1.22E-05 m/s. The simulation adopted caisson dimensions of 8m diameter, 4m skirt length (Aspect ratio = 0.5) and wall thickness of 50 mm.

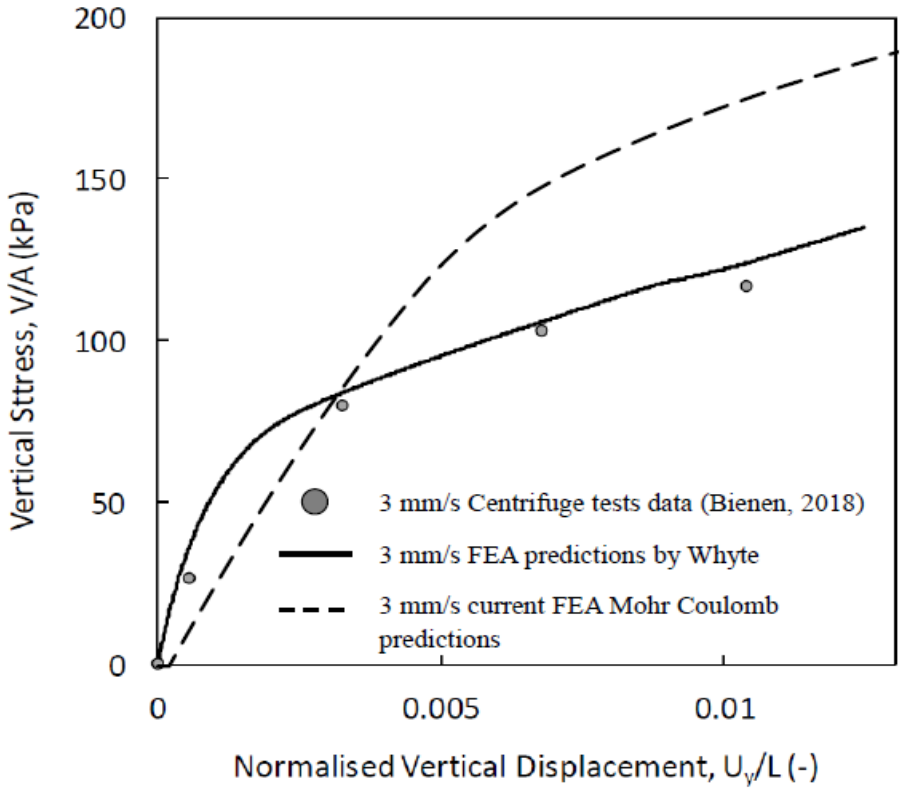

Figure 4-25 Load displacement curve for 3mm/s for UWA Superfine Silica Sand

Fig.4.25 represents the load displacement response in terms of vertical tensile stress and normalized displacement from centrifuge results, Whyte's numerical study and the current study. From simple inspection, it can be observed that the current FE model with Mohr Coulomb failure model drastically overpredicts the ultimate capacity, whereas the bounding surface model is successful in accurately following the stress curve. This overestimation of undrained capacity by Mohr Coulomb can be attributed to the model's inability to accurately capture dilative behavior in soil, as described in Section 2.2.1. Despite the failure to capture the undrained capacity, the model still accurately captures the initial soil response.

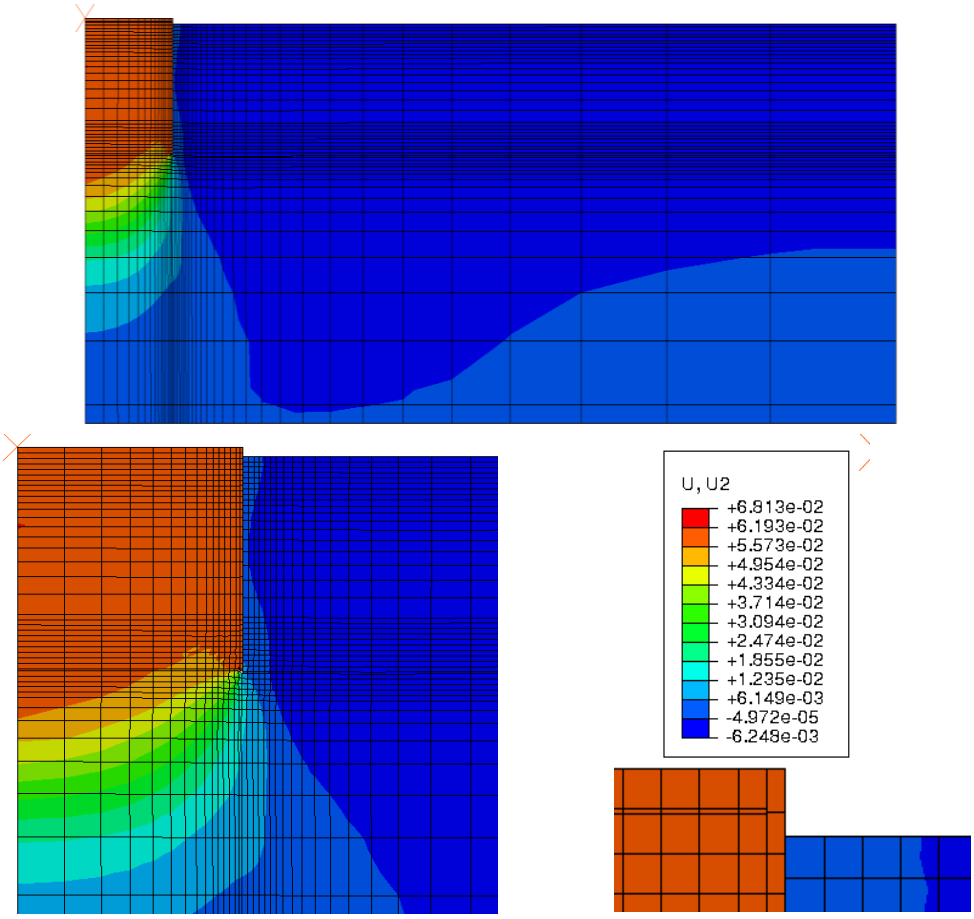

Figure 4-26 Displacement contours for UWA Superfine Silica Sand at 3mm/s

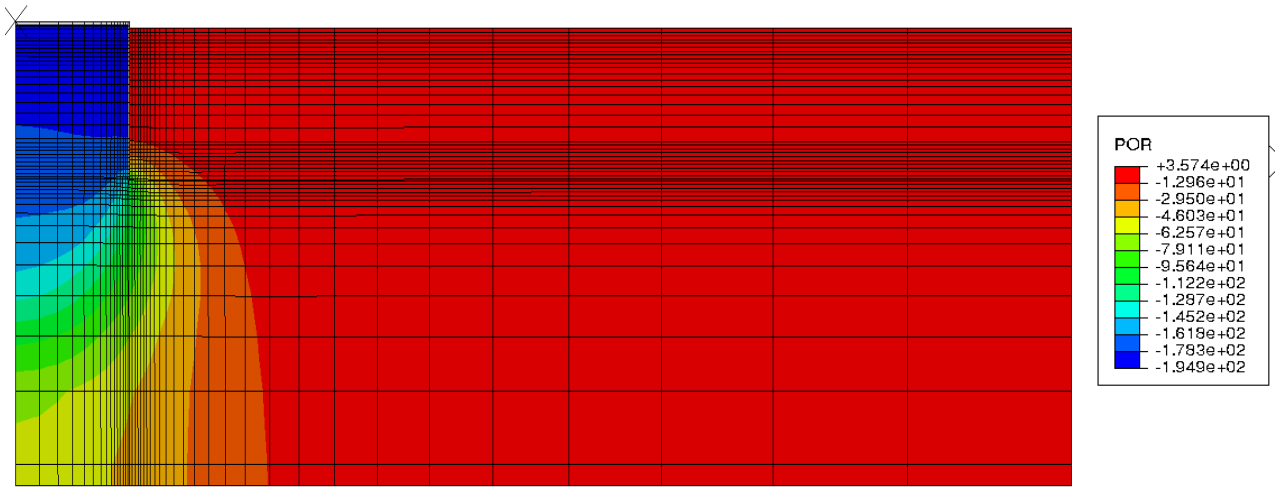

Figure 4-27 Pore pressure contours for UWA Superfine Silica Sand at 3mm/s

The displacement (Fig. 4.26) and the stress contours (Fig. 4.27) for the current loading rate demonstrate a typically undrained behavior.

4.1.2.2.3. Comparison with Whyte's numerical study

To further understand the partial drainage conditions where the finite element model in the current study with Mohr Coulomb fails, Whyte's drainage transition curves were used to compare with the transition curves form the current study. The curve was plotted in normalized load vs time space. The vertical load was normalized by dividing the load with the load for the fully drained condition, with the normalized time factor as described in Section 4.1.1.3. Variation of the capacity for a particular normalized displacement is presented. It can be observed that for smaller time factor, i.e., short term loading or undrained loading, the difference in the predicted capacity by both the cases is significantly high, and with the increase in time, i.e., transition into drained behavior, this difference decreases, subsequently vanishing completely in the fully drained condition. (Fig. 4.28)

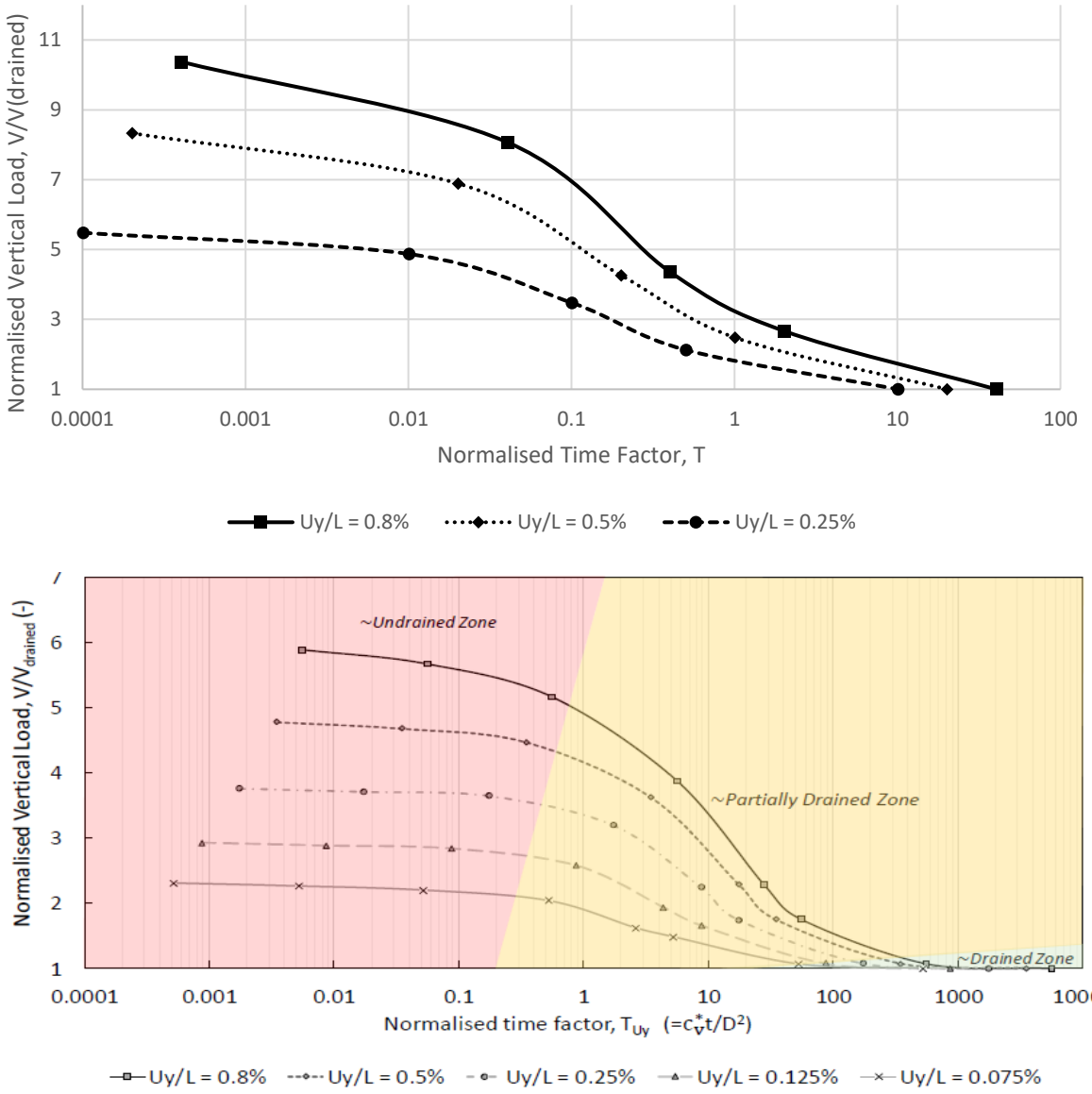

Figure 4-28 Transition curve for UWA Superfine Silica sand in terms of time factor a) Predictions by current study b) Predictions by Whyte's model. Reprinted from [Whyte}

This shows the failure of the current study to predict undrained capacity of dense sand. Since dilation significantly influences the undrained behavior, and the Mohr Coulomb model is known to overpredict dilation, it is reasonable to assume this as the cause of the inadequacy of the current study. Thus, in an effort to overcome the observed shortcomings

and to accurately capture the undrained response of dense sand with the finite element model developed in the current study, the next phase of this thesis adopts a hypoplastic soil failure model by Wolfersdorff [Wolfersdorff, 1996].

4.2. Hypoplasticity soil failure model

The second phase of the thesis employed the Hypoplastic soil failure model, as described in Section 2.2.2, to simulate the response of a suction bucket subjected to a monotonic vertical uplift. The rate dependent failure model, with its parameters closely related to the granulometric behaviour of the soil has proven to provide successful results in previous studies of similar conditions. [Thieken, 2014]

4.2.1. **IGtH dense soil**

The first series of tests using this failure model was conducted on dense IGtH sand, with soil properties described in Section 3.3, and model parameters listed in Table 3.6.

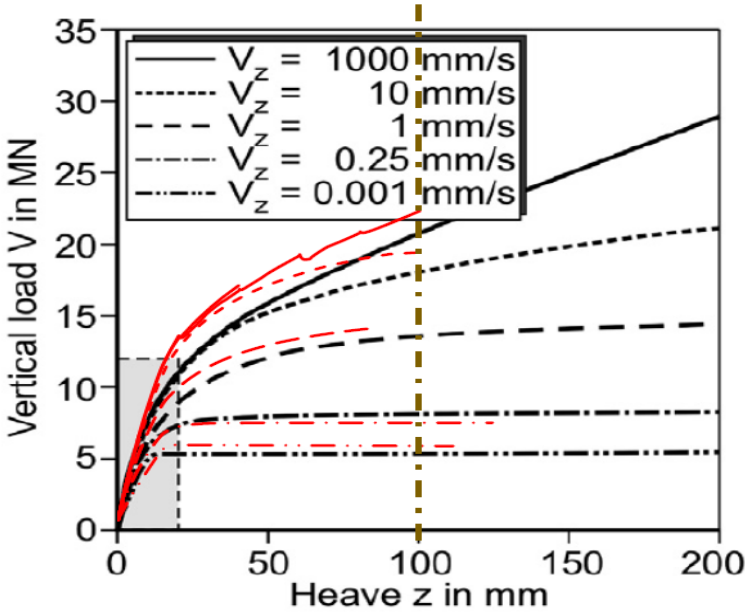

Figure 4-29 Load-displacement curves predicted for IGtH dense sand for different loading rates by Thieken [Thieken, 2014] (in black) and by the current study (in red)

The outcome of this series was compared against the results from a similar study conducted by Thieken as described in Section 2.4.4.2.1. [Thieken, 2014].

A suction caisson of diameter and skirt length 10m, with wall thickness of 30mm was modelled. The tensile load was applied in a range of loading rates between 0.001mm/s and 1000mm/s, till a targeted uplift of 200mm (2% of the caisson diameter). The tests were conducted for an initial void ratio of 0.6 and permeability of 7.73E-04 m/s.

4.2.1.1. Comparisons with Thieken's response

The load versus displacement curve for different loading rates is presented in Fig. 4.29, overlaid on the similar responses from Thieken's study. Thieken's study uses a self-weight of 0.8MN for the suction caisson, whereas the current study adopts a weightless caisson. Thus, 0.8MN vertical load was added to the current results, for better comparison.

The trend of an increase in the resistance with the increase in the loading rates and suction is consistent with the theoretical expectations. For the drained resistance, considered at the loading rate of 0.001mm/s, the current study predicts an uplift resistance of 5.16 MN, whereas Thieken's model predicts (approximately) 5 MN. Based on the analytical model proposed by Houlsby (Houlsby, 2005) as described in Section 2.4.3, the undrained capacity was calculated to be 5.77 MN. This presents an error of 13% and 10% to the predictions made by Thieken's model and the current FE model, respectively.

For the partially drained and the undrained conditions, the initial stiffness response was accurately captured. But, as loading continues, the current model tends to overpredict the vertical capacity, with the amount of overestimation increasing with uplift.

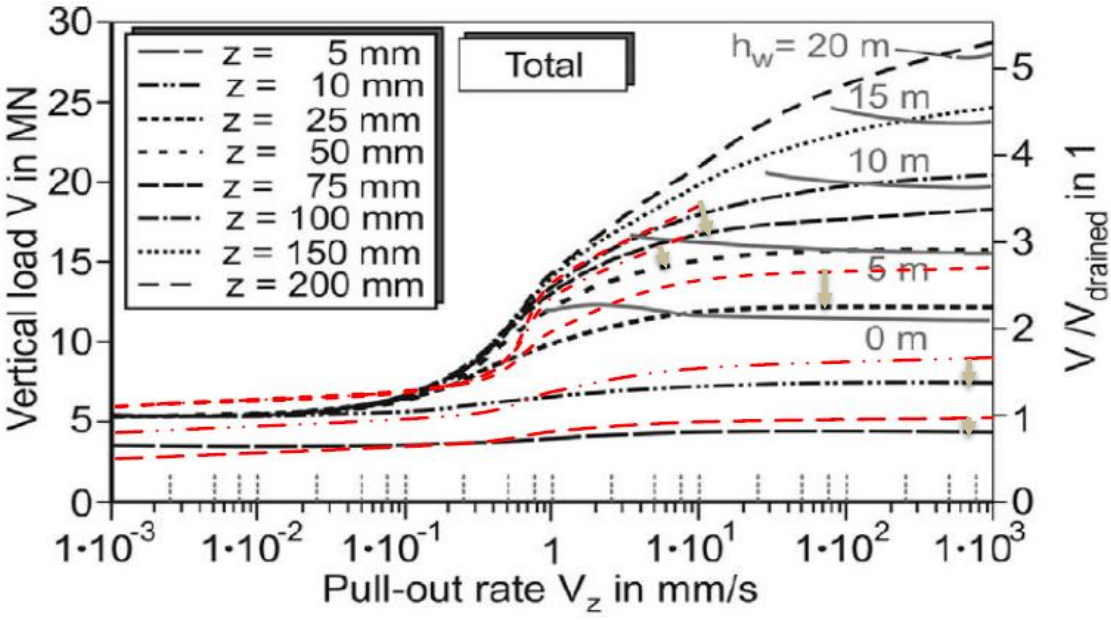

Figure 4-30 Transition curve for IGtH dense sand by Thieken (in black, Reprinted from [Thieken, 2014]) and by current study (in red)

The trend could be studied only till a displacement of 1% (100 mm uplift), and not till the targeted 2%. This was due to numerical convergence issues encountered at higher displacements. Displacement equilibrium criteria required by Abaqus, could not be met for the soil nodes in the region below the tip of the caisson skirt. The soil in this particular region undergoes excessive distortion, and effect of pore water pressure should be taken into consideration while modelling it. Possible means to overcome this concern has been further discussed in Section 4.4. Thus, the current FE model with the Hypoplastic soil failure model could be used to make predictions for only displacements up to 1%.

The transition curve attained from the simulations is presented in Fig 4.30, superimposed on the similar curve from Thieken's study. The red lines represent the transition curve for different vertical displacements attained from the current study, with grey arrows indicating their corresponding curves predicted by Thieken. As observed in

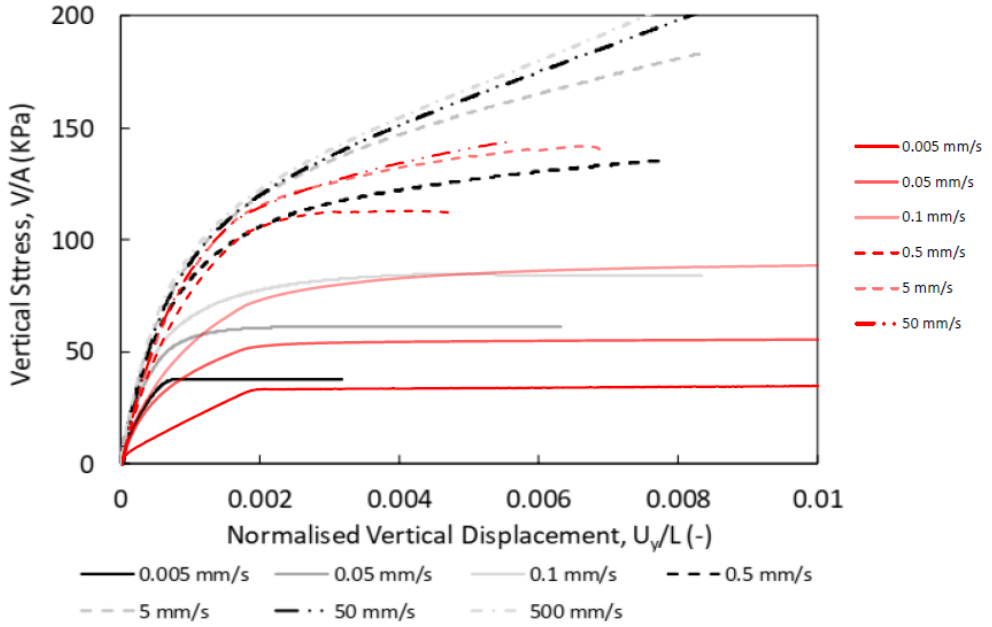

Figure 4-31 Load-displacement curve for different loading rates for UWA Superfine Silica Sand using Hypoplasticity model (in red) and Whyte's bounding surface model (In black, Reprinted from [Whyte])

Fig. 4.29, the initial predictions, i.e. at lower displacements, are acceptable matches, throughout the different loading rates. The capacity at higher displacements tend to be overpredicted with the difference between the two studies increasing with the loading rate.

As mentioned earlier, due to numerical convergence issues, complete transition curves were successfully attained till a caisson uplift of only 100mm (1% of diameter).

4.2.2. **UWA Superfine Silica Sand**

The second set of tests in the second phase of the thesis was conducted on UWA Superfine Silica Sand, which has been the primary soil in focus for this study. The Hypoplasticity model parameters adopted for this soil type have been listed in Table 3.8, determined using equations described in Section 2.2.2.1.

The load displacement curves for this soil type using the Hypoplasticity soil model are presented in Fig. 4.31, which also contains Whyte's curves. For the drained conditions, or the low pull-out rates, though ultimate capacity predictions match, the amount of uplift required to reach that value vary considerably. Whyte's model predicts a much stiffer response. Calculating the drained capacity using Houlsby's method gives a value of 951.036 KN (33.63kPa). This will give an error of just 2.9% (34.8 kPa) for the Hypoplastic drained capacity prediction, while an error of 12.9% (~38 kPa) was attained for Whyte's prediction.

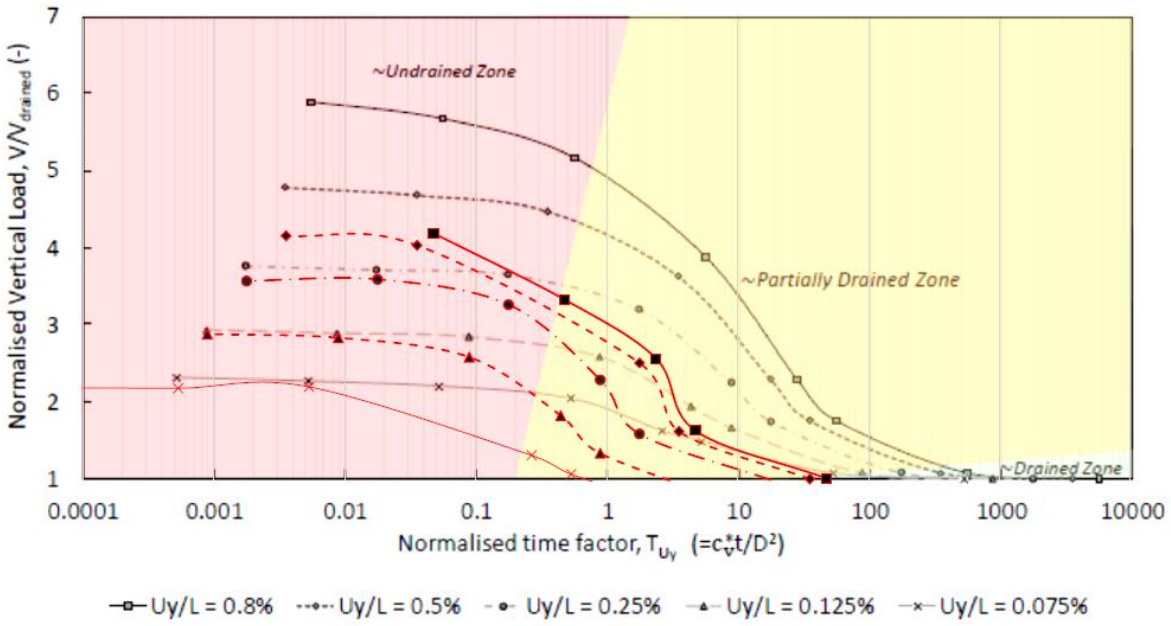

Figure 4-32 Transition curve for UWA Superfine Silica sand by Whyte (in black, Reprinted from [Whyte]) and by current study (in red)

The low predictions of the initial response compared to Whyte's are observed throughout the partially drained conditions, with the current model finally agreeing with Whyte's initial response only at higher pull-out rates, or towards the undrained conditions. This trend reverses for the ultimate capacity prediction, where it can be observed in Fig.

4.31 that the partially drained capacities match but the undrained capacities are underpredicted.

The same results were presented in terms of a transition curve in Fig. 4.32, where the current study results are depicted in red, and are superimposed on Whyte's (black) plot. The underestimation of the initial drained and partially drained response by the current study compared to Whyte, as described above are also visible in this graph. The lower displacements do not match his results, but for lower time periods (or short-term loading or undrained loading), they ultimately fare well. For the ultimate capacities, or the higher displacements, as presented in Fig. 4.32, the undrained capacities are considerably underpredicted.

But taking into account that this set of comparison was conducted only with another numerical model, comparisons with centrifuge tests are presented in the following section. Adopting the same comparison procedure as done with the Mohr Coulomb model, and presented in Section 4.1.2, the predictions made by the current FE model for the UWA Superfine Silica Sand using the Hypoplastic soil model, was compared against outcomes of previous similar studies – centrifuge tests by Senders [Senders, 2008] and Bienen [Bienen, 2018], and Whyte's numerical study [Whyte], as described in Section 2.4.4.1 and Section 2.4.4.2.2, respectively.

4.2.2.1. Comparisons with Centrifuge tests

As described in Section 4.1.2.2.1 and Section 4.1.2.2.2, similar testing conditions were adopted to conduct the comparative study.

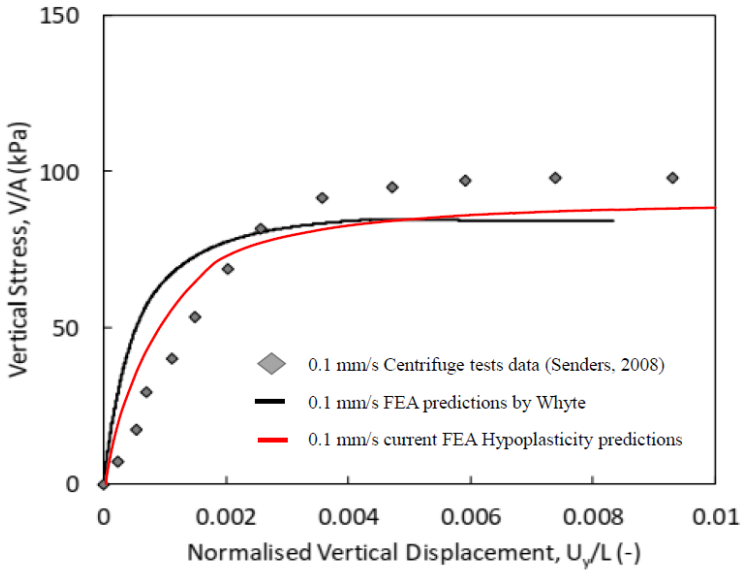

Figure 4-33 Load displacement curve for 0.1mm/s for UWA Superfine Silica Sand

For the drained analysis at a loading rate of 0.1mm/s, as shown in Fig. 4.33, the Hypoplastic model predictions are closer to the centrifuge results attained by Senders [Senders, 2008] compared to Whyte's bounding surface model predictions. A much stiffer initial response is predicted by Whyte's model, which is improved by the current model. The ultimate capacity, though underpredicted by both the numerical studies, is still better captured by the current study using the Hypoplastic soil model, which suggests its load displacement curve to follow the trend of the path set by the Centrifuge results where Whyte's model flattens out at higher displacements.

It should also be noted that the studies conducted at the University of Western Australia restricted the vertical uplift of the caisson to only 1% of the skirt length, in contrast to the 2% target in Thieken's study. This further strengthens the question of the practical need and relevance of subjecting a suction caisson supporting an offshore wind turbine to high displacements.

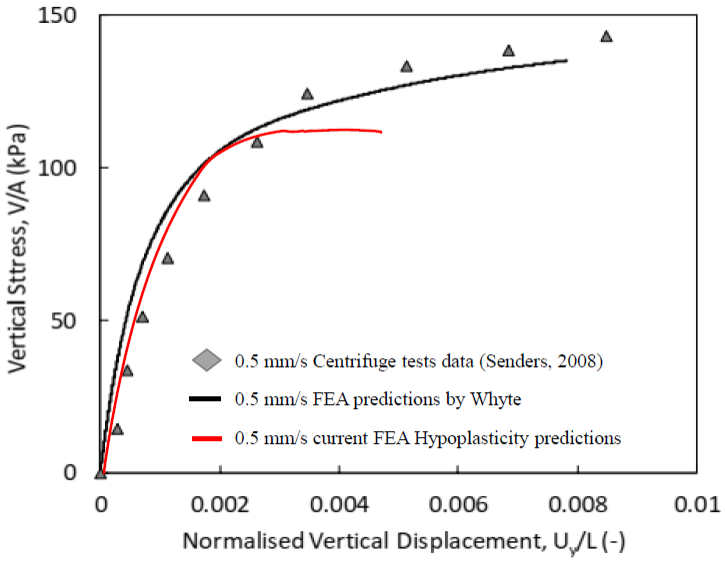

Figure 4-35 Load displacement curve for 0.5mm/s for UWA Superfine Silica Sand

For the partially drained condition of 0.5mm/s, as shown in Fig. 4.34, numerical convergence issues were encountered and the tests had to be stopped at 0.4% displacement. Apart from that, as can be observed in the figure, the current model predictions fall short in capturing the resistance behavior after the initial elastic response, which were similar to the bounding surface model predictions and the centrifuge results.

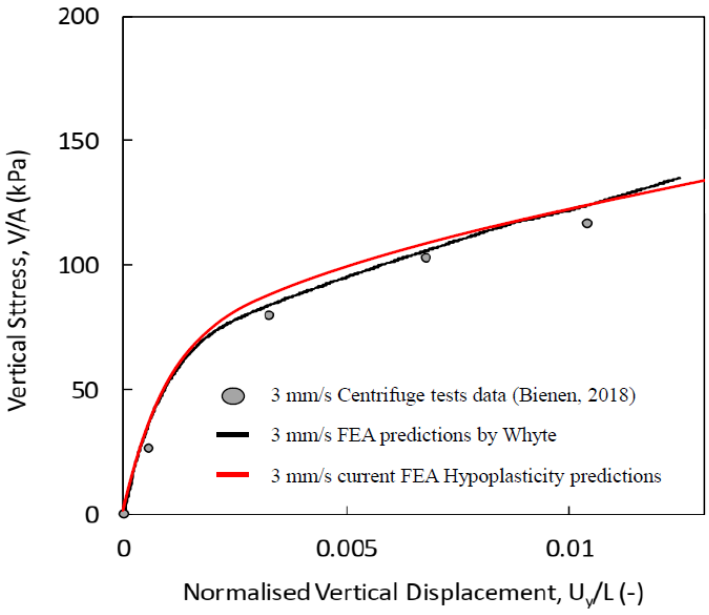

Figure 4-34 Load displacement curve for 3mm/s for UWA Superfine Silica Sand

Thus, for the lower displacements value, both the soil failure models predict acceptable results compared to the centrifuge results for a partially drained condition.

Centrifuge tests described in Section 2.4.4.2.2, conducted by Bienen [Bienen, 2018] were used to assess the fully undrained predictions by the current model. This is presented, along with Whyte's predictions, in Fig. 4.35. From visual observations, it can be noted that the prediction by the current study accurately follows the path of Bienen's test. As loading continues, the Hypoplasticity predictions suggests closer match with the centrifuge results compared to that by the bounding surface model.

Thus, with the comparisons conducted, it can be concluded that for UWA Superfine Silica sand, using the Hypoplasticity soil model predicts good matches with the centrifuge results for low displacements for all the drainage conditions. Though, Whyte's model does the same. For the ultimate capacities, the completely drained and the completely undrained predictions are better from the Hypoplastic model vs the bounding surface model, with the centrifuge results providing a frame of reference. Though, for the partially drained conditions, the Hypoplasticity model provides an underestimation of the ultimate capacity, before the model fails due to numerical convergence at higher displacements. Section 4.4 addresses the issue of the permissible amount of displacement or uplift for a suction caisson supporting an OWT.

4.3. Comparison of the different soil failure models

This thesis employed two failure models -Mohr Coulomb and Hypoplasticity, to predict the capacity of a suction caisson in UWA Superfine Silica Sand subjected to a monotonic vertical uplift, subjected to a range of drainage conditions. The results attained

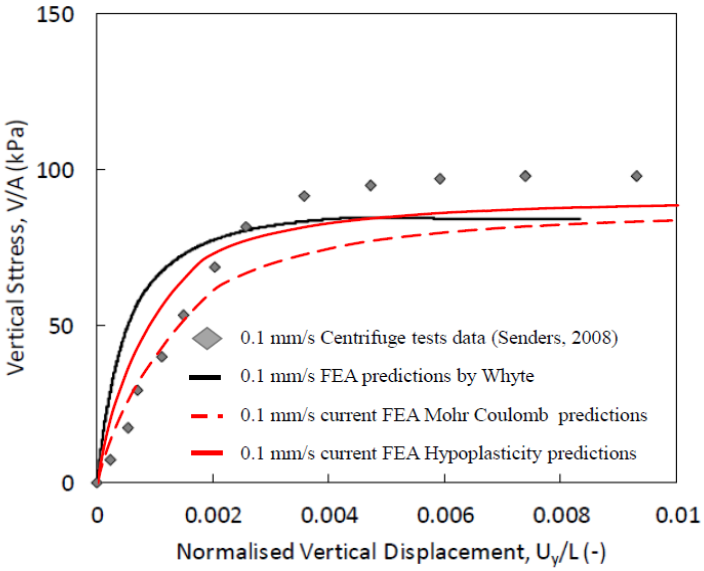

Figure 4-36 Load displacement curve for 0.1mm/s for UWA Superfine Silica Sand

were compared to a previously conducted numerical study which utilized a third failure model – a bounding surface sand model. This section provides a comparison of the predictions made by all the three numerical models, and the ease of application of each of the soil models.

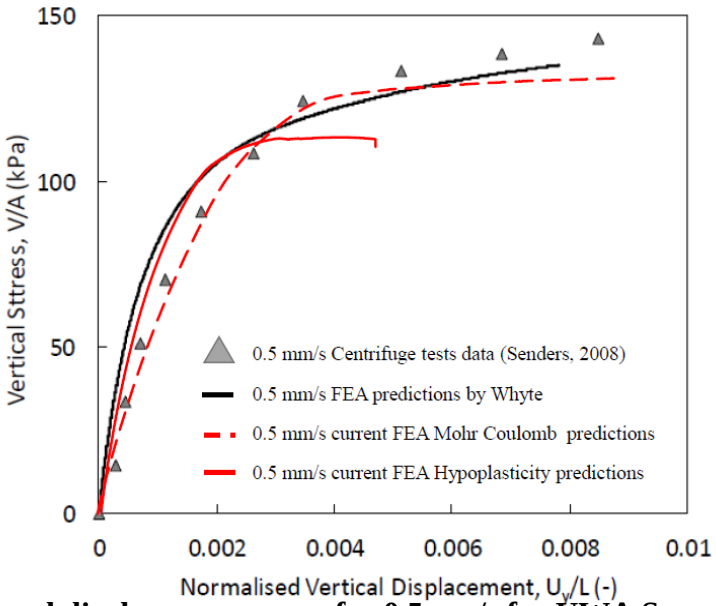

Figure 4-37 Load displacement curve for 0.5mm/s for UWA Superfine Silica Sand

They were first compared against the outcomes of the centrifuge tests, as described in Section 2.4.4.1.

The outcomes from the Mohr Coulomb model constantly provided the most accurate predictions for the initial elastic response, for all the drainage conditions (Fig. 4.36, 4.37, 4.38). This was achieved by relating the Young's modulus to the rigidity index of the soil. [Hakeem, 2019]

For the predictions of the ultimate capacity, for the completely drained response, Mohr Coulomb resulted in an error of 10.3%, Whyte's bounding surface model resulted in an error of 12.9%, while the Hypoplasticity model results only in an error 0f 2.9%, when compared to the capacity derived from Houlsby's analytical method. Thus, the Hypoplastic model is best suited for predicting completely drained response. This can further be observed in Fig. 4.36 where the Hypoplastic model provides the best match with the centrifuge results, considering a balance between the initial and ultimate responses.

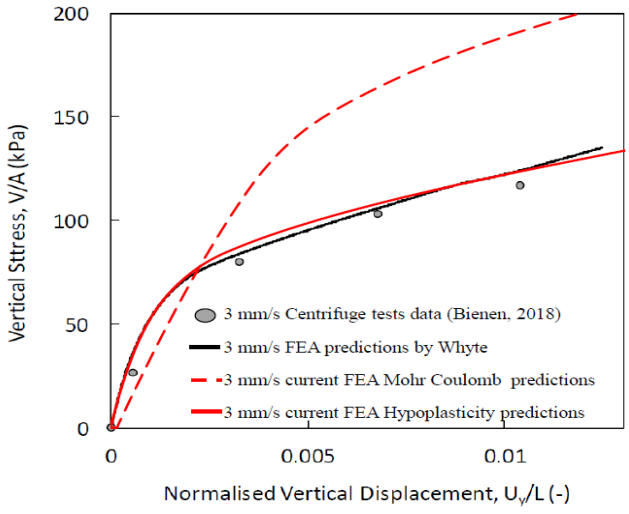

Figure 4-38 Load displacement curve for 0.5mm/s for UWA Superfine Silica Sand

For the partially drained condition, as shown in Fig. 4.37, the Hypoplasticity model and the Mohr Coulomb model, both underestimate the ultimate capacities. The Hypoplasticity model further fails in this condition since the FE model was unable to converge at higher displacements. Thus, the bounding surface model should be referred to for the ultimate capacities of partially drained conditions.

For a fully undrained condition, as shown in Fig. 4.38, the Mohr Coulomb model vastly over predicts the ultimate capacity. The reasons for this inaccuracy are provided in Section 4.1.2.2.3. Between the Hypoplasticity soil model and the bounding surface soil model, as described in Section 4.2.2.1, the Hypoplastic model provides slightly more accurate results.

These differences are further represented in Fig. 4.39 which shows the results in the form of a transition curve. For lower displacements, the stiffer response by the bounding surface model for the partially drained and completely drained conditions can be observed by its higher predictions in the partially drained region. Though, they eventually match with the Hypoplastic predictions in the undrained region. For the higher displacements, the ultimate capacities vary significantly for the three models. The Mohr Coulomb drastically overpredicts, with the overestimation increasing towards the fully undrained region. The Hypoplasticity model, though it provides accurate undrained response, as shown in Fig. 4.38, still underpredicts the capacity for high displacements in the partially drained cases. The ultimate partially drained predictions by Whyte's model are taken as the frame of reference since they provided the best match in Fig.4.37, though, only one set of centrifuge tests were available for this condition.

Predictions by the current FE model using Mohr Coulomb soil

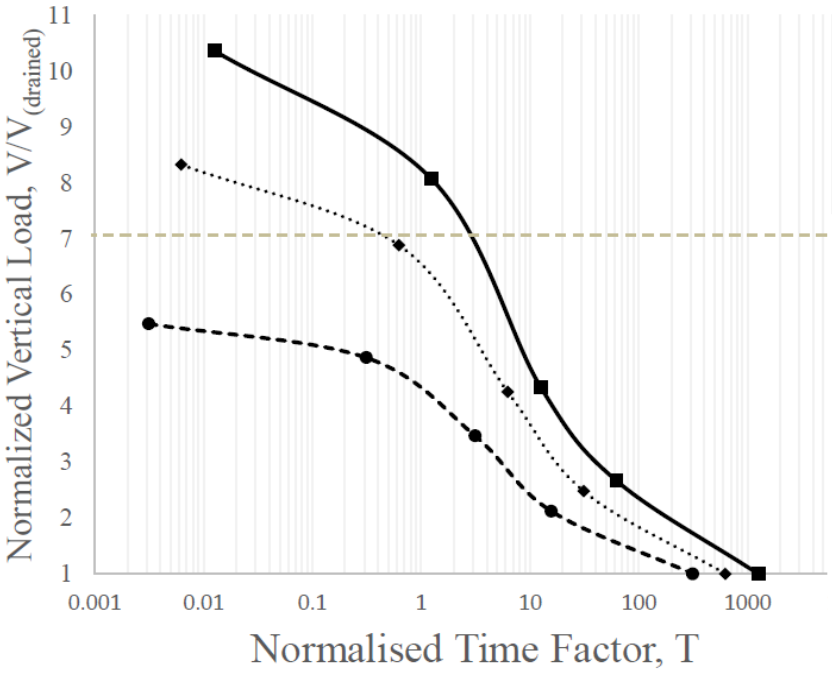

Predictions by Whyte's model using bounding surface soil model (black line, reprinted from [Whyte]) and the current FE model using Hypoplasticity soil model (red line)

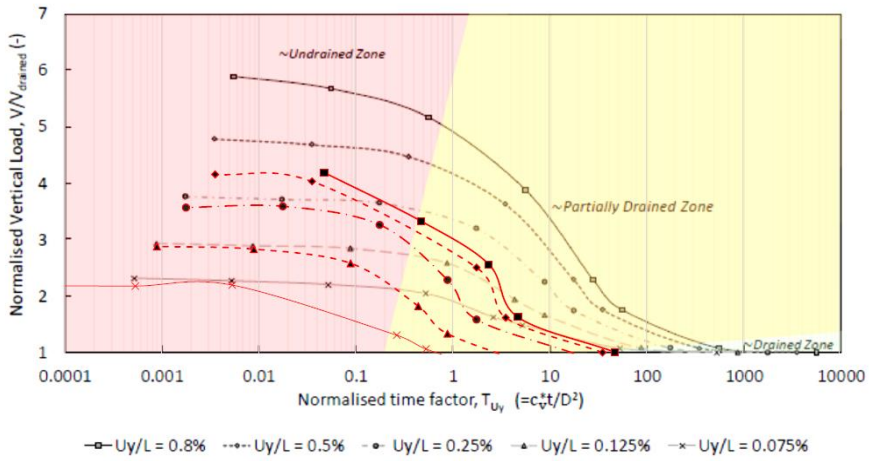

Figure 4-39 Transition curve for UWA Superfine Silica Sand

Thus, it can be concluded that, given the accurate predictions of the Hypoplasticity model for the fully drained and the fully undrained cases, this model should be referred to for them, especially for the ultimate capacities (high displacements). An additional advantage for the model is also its requirement of only eight, easily derivable parameters. For partially drained conditions, Whyte's bounding surface model is recommended due to its accuracy in predicting the ultimate capacity, though it requires a total of nineteen parameters. If the study is limited to only low displacements, the Mohr Coulomb model should be employed, since it provides accurate response with only five required parameters.

Hypoplasticity failure model, when compared to centrifuge results, but lacks in the partially drained capacities. Whereas, the bounding surface model provides consistent fair accuracies with the centrifuge results.

Further tests for partially drained conditions show the Hypoplasticity model falling short for high displacements only. But a key attraction for the model was its requirement of only eight, fairly easily derivable parameters, against the 19 required by the complex bounding surface model.

4.4. Practical application

The focus of the current thesis was to predict the capacity of the windward suction caisson in a tripod foundation system for an offshore wind turbine in dense sand for the duration of its complete operational lifespan. During this time frame, the OWT is expected to be subjected to various offshore environmental conditions. Such conditions can be represented by the drainage condition of the soil. A drained condition, simulated by

applying the test load gradually, represents a normal condition; whereas, the undrained condition, simulated by a rapid application of the load, represents the loading conditions the OWT will be exposed to during an extreme storm condition. The environmental loads, thus can be categorized on the basis of their time periods – severity of the loads increase with the decrease in the loading duration.

Aerodynamic horizontal load and the hydrodynamic horizontal load are the two environmental loads considered in the design of the foundation structure. They have been described in detail in Section 2.4.1. For the aerodynamic loading, an extreme operational gust is taken as an extreme storm condition. A gust is a short-term wind speed variation within a turbulent wind field [Branlard, 2008], and an extreme operating gust is a period which experiences a decrease in the wind speed, followed by a steep rise, a steep drop and then again, a rise back to the average wind speed. Data suggests an extreme operating gust lasts for 10.5 seconds, with a return period of 50 years. [DNV, 2007] For the hydrodynamic loading, the velocity and the acceleration of the water particles due to the motion of the waves and the currents control the loading. The velocity of a water particle varies from a positive to a negative value as the wave passes, thus the horizontal hydrodynamic load increases and decreases in the time taken by a wave to pass through. This time period during a storm condition can be taken as 12 seconds. [Senders, 2008] Thus, a limiting time period of 10.5 seconds is considered to represent an extreme storm condition. These values are typical representations of the offshore conditions in the North Sea and the Norwegian Sea.

Another factor which aids in narrowing down the area of interest for the practical application of a foundation supporting an OWT is the allowable displacement. The typical allowable vertical displacement or uplift for an OWT is less than 20-30mm, from an operational point of view. Data suggests the maximum allowable tilt for an OWT after installation to be between 0.003 to 0.009 radian (0.2 degrees to 0.5 degrees). [Malhotra, 2011] This produces an uplift of 0.17% to 0.45% of the diameter of the suction caisson. For the base case in the study, which adopts a caisson of 6m diameter, this results in a limiting value of 30mm (27mm exact) allowable uplift.

Fig. 4.36 to Fig. 4.38 have been recreated in Fig. 4.40 to Fig. 4.42 with a vertical line representing the allowable operational displacement at 0.45%. Taking this into account,

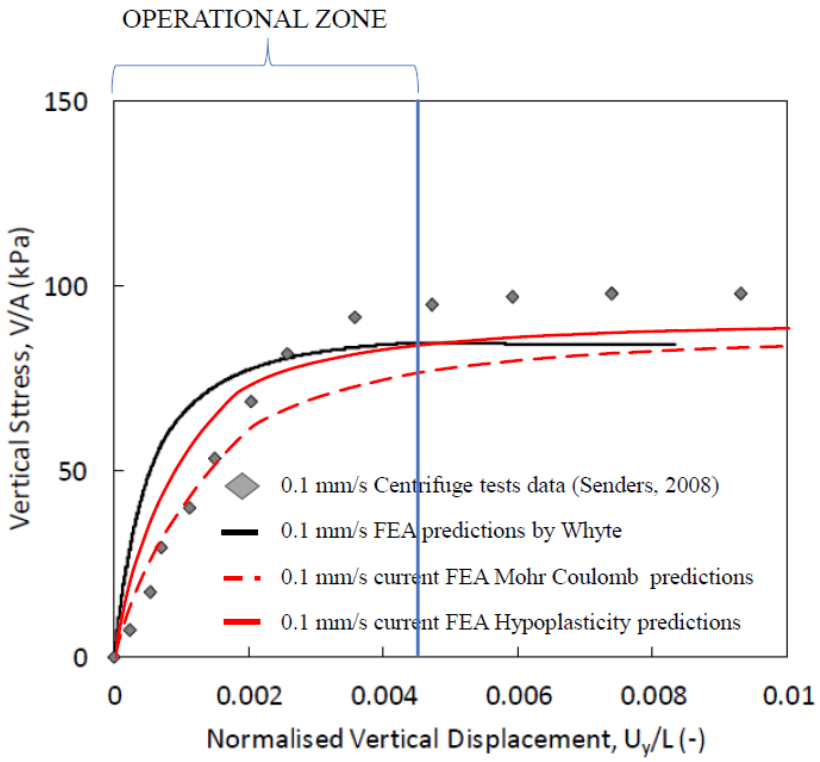

Figure 4-40 Load displacement curve for 0.1mm/s for UWA Superfine Silica Sand with operational displacement limit

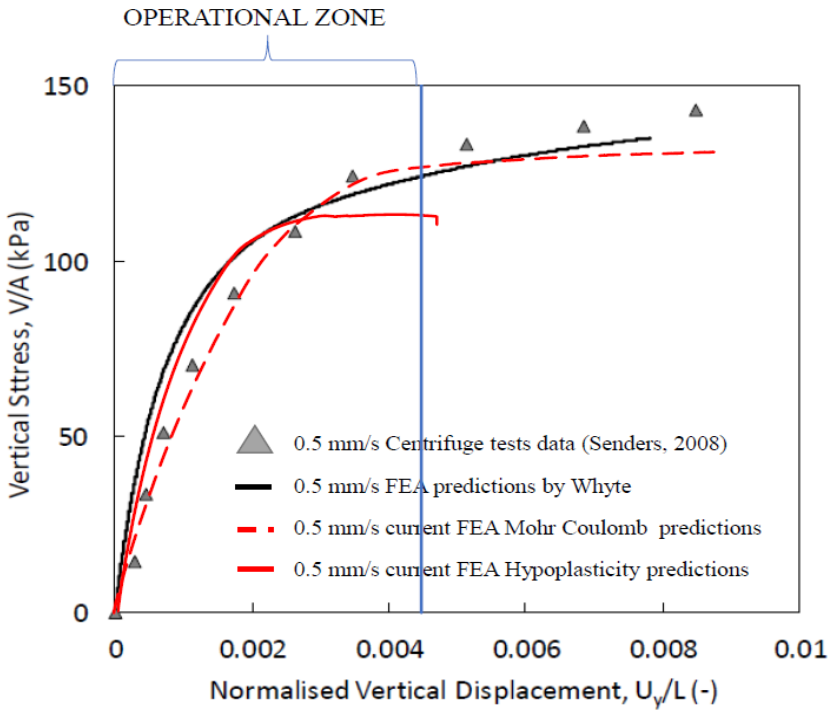

Figure 4-41 Load displacement curve for 0.5mm/s for UWA Superfine Silica Sand with operational displacement limit

the problem encounter in Fig. 3.37 for the prediction by the Hypoplasticity model can be ignored, where the FE model fails at high displacements, though it still underpredicts the capacity. The figures reinforce the conclusion in Section 4.3, which recommends the usage of the Hypoplasticity model for the fully drained and the fully undrained conditions, but for the partial drainage capacity, Whyte's bounding surface model should be employed.

A transition curve, presented in Fig. 4.43, similar to Fig. 4.39, factors in the storm condition as a function of its time period. The curve is plotted in terms of normalized uplift capacity and normalized time factor, T. This time factor is a function of the consolidation coefficient of the soil, the geometry of the suction caisson and the time period of the storm. A time period of 10.5 seconds is used as the cutoff representing an extreme storm condition. The normalized time factor for UWA Superfine Silica Sand and a suction

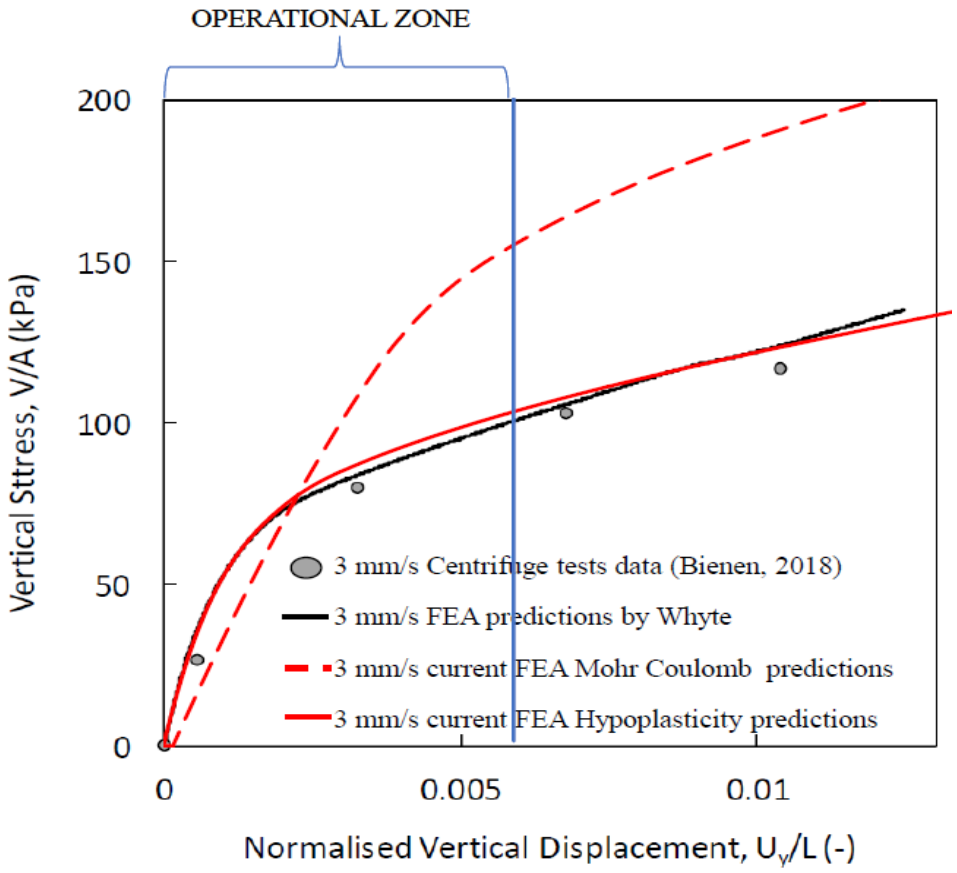

Figure 4-42 Load displacement curve for 3mm/s for UWA Superfine Silica Sand with operational displacement limit

caisson with a 6m diameter, during a typical storm condition is 0.0353 and is illustrated in Fig. 4.43 using the blue vertical line. The different lines of displacement presented in the graph is also restricted to the allowable displacement of 30mm or 0.5% displacement.

Here, for the lower displacements (up to 0.2% displacement), predictions by the Hypoplasticity model should be referred to throughout the entire transition curve, since they provide a better match to the centrifuge results. For the higher displacements (0.2% to 0.45% displacement), for the partially drained zone, Whyte's bounding surface model predictions should be adopted, but for the fully drained and the fully undrained conditions, again, the Hypoplasticity model results should be taken.

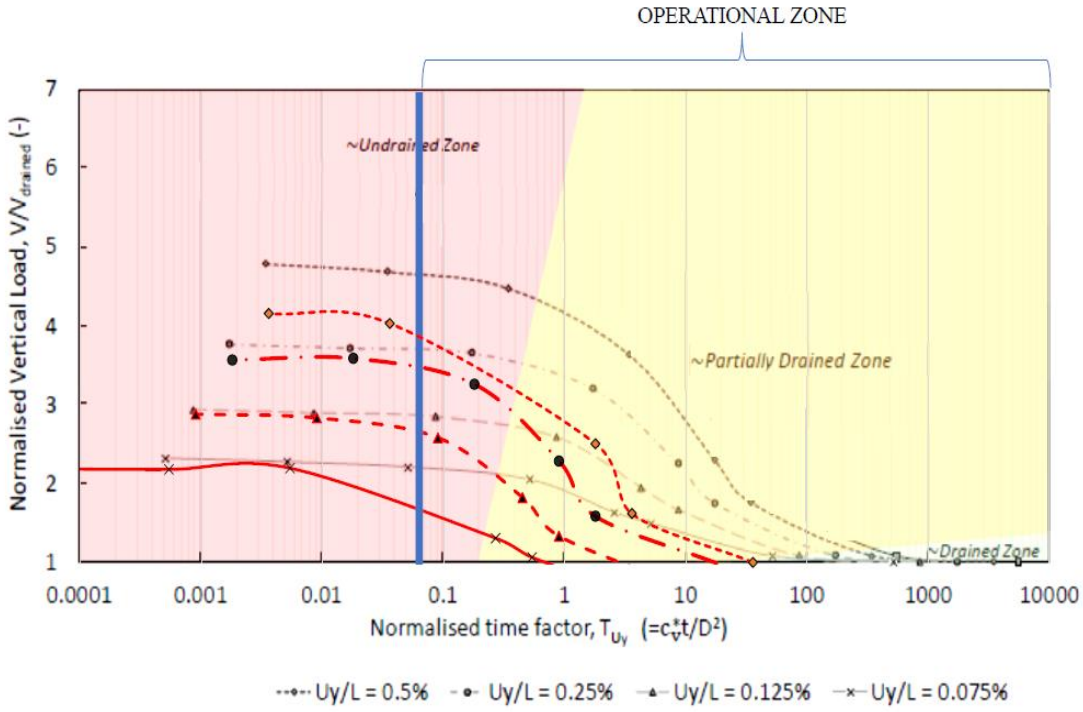

Figure 4-43 Transition curve for UWA Superfine Silica Sand with operational zone

4.4.1. **Resistance against environmental conditions**

The resistance offered by the caisson is required to withstand the environmental conditions an OWT is exposed to. A typical 3MW OWT, 86m high, supported under a 25m depth of water by a tripod suction caisson foundation system, with the caisson spaced at a distance of 22.2m from the column of the OWT is considered. [Senders, 2008] The caisson dimensions are 6m in diameter and 4m in skirt length. The total weight of the structure can be estimated to be equal to 6.6MN (~7MN), distributed equally over each caisson.

During a typical storm condition, peak aerodynamic loads will go up to 1.2MN and peak hydrodynamic loads are in the order of 3 – 4MN in the horizontal direction. These

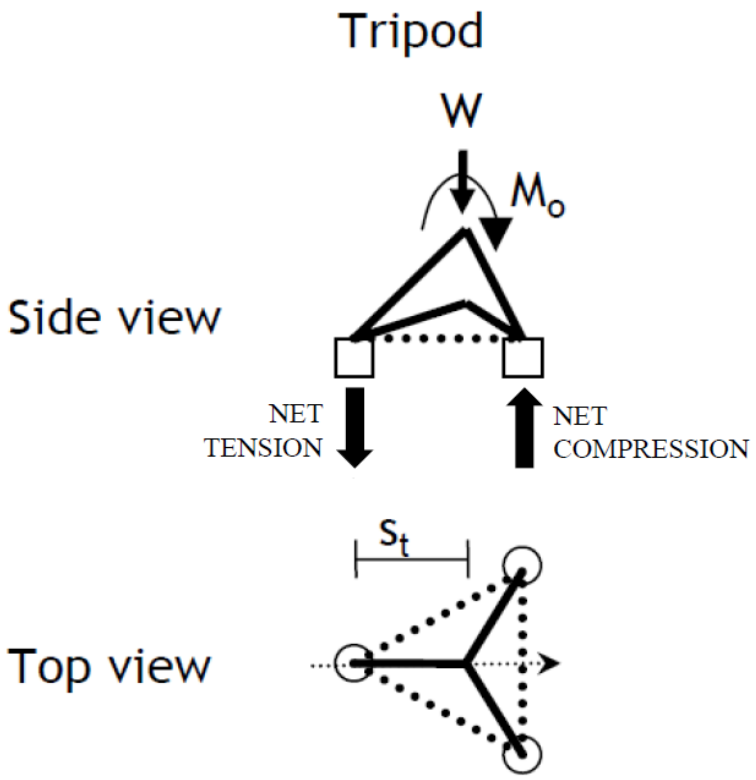

Figure 4-44 Loading on a tripod foundation. Reprinted from [Senders, 2008]

will result in an overturning moment of 153MN-m. [Senders, 2008] This moment will be resisted by the push-pull mechanism of the caissons in the tripod system, as described in Section 2.4.1. This push-pull mechanism is a result of the vertical loads on the suction caissons, the caissons in the leeward side of the tripod will undergo compression and on the windward side will undergo compression. The restoring moment can be calculated using the following expression: [Senders, 2008] (Fig. 4.44)

$$M_R = (1.5 * V_T + 0.5 * W)s_t$$

The current FE model, with the Hypoplasticity soil model, predicts a tensile capacity of 3.889 MN during a storm condition. This capacity is attained at the operational displacement limit of 0.45%, from a fully undrained analysis. Along with the self-weight

of the caisson (0.462 MN), the total uplift resistance predicted by the model is 4.351 MN. With the considered values of 7MN for the weight of the structure and a spacing of 22.2m, the above expression results in a restoring moment of 222.58 MN-m. This provides a factor of safety of 1.454. Thus, the FE model developed, with the Hypoplasticity soil model, is capable of successfully predicting the behavior required to resist failure.

5. CONCLUSIONS

The objective set forth in this thesis was to investigate the performance of a suction caisson as a means to support offshore wind farms in dense sands, with a specific interest in drainage effects for UWA Superfine Silica Sand. The environmental loads expected to be endured by the offshore wind turbine during its operational lifespan under different offshore environmental conditions were accounted for.

The numerical study simulated the response of a trailing caisson in a tripod jacket subjected to monotonic uplift, under a range of drainage conditions, by studying it under the influence of different loading rates. A monotonic, purely vertical uplift was adopted as the testing load since previous studies had established the tensile capacity of the windward caisson to be the critical design load condition; while the different drainage conditions were employed to represent the various offshore environmental states. This was justified as the capacity of the foundation is dependent on the permeability of the soil, along with the time period of the load. The model was assessed and validated by conducting comparative analysis against published results of tests under the same conditions.

An axisymmetric, hydro mechanical finite element model was developed and tested in the software package ABAQUS-6.12.1. The first phase of the study employed the classical Mohr Coulomb soil failure model, with the first series of tests conducted on a generic medium-dense sand and the second series on the UWA Superfine Silica Sand. For the first set of tests on the generic medium-dense sand, the model's predicted behavioral

trend for the ultimate capacity of the caisson under the application of different loading rates produced satisfactory results. Theoretically established concepts of drained frictional behavior and undrained reverse end bearing behavior were observed in the outcomes of the model, with intermediate results for the partial drainage conditions. Simple analytical calculations for the drained capacity gave an error of 1.95% against the predicted model capacity for long term loading. The transition curve for the capacity showed a non-linear path with respect to the duration load application, with an exponential decrease as the loading time rose. Different aspects of the model were assessed and confirmed by conducting elementary validation tests – response of the model at an elementary level, shear response along the skirt of the caisson and mean volumetric change in the model. With acceptable outcomes in the validation tests, the second set of tests with the UWA Superfine Silica Sand were conducted.

The second series of tests using the Mohr Coulomb soil failure model focused on the response of the caisson when installed in UWA Superfine Silica sand. The purpose of this was to develop a model capable of making accurate predictions, tested against available centrifuge test results of the same conditions, and thus resort to simple soil models to predict the ultimate capacity rather than complex models such as bounding surface soil models or rate dependent soil models. Partial success was attained in this section. The model was able to successfully capture the initial stiffness response of the soil under all drainage conditions, when compared to centrifuge test results. For the ultimate capacity, though the model was successful in accurately predicting the drained behavior and limited partially undrained behavior, a drastic overestimated capacity was predicted for the fully

undrained response. This outcome was attributed to a well-known shortcoming of the Mohr Coulomb soil model – inaccuracy in dilatancy responses. Since for dense sands, dilatancy of the soil is a major contributor in its strength, this was accepted as a possible source of error.

The second phase of the thesis employed the rate dependent Hypoplastic soil failure model, to test the same loading conditions. The model in the form presented by Wolfersdorff [Wolfersdorff, 1996] was adopted and first tested in dense IGtH sand, before proceeding to UWA Superfine Silica Sand. The rate dependent model whose parameters are closely related to the granular properties of the soil was expected to better capture the dilative response of dense sand. This soil model was first adopted for a single element triaxial test, similar to those conducted by Wolfersdorff. [Wolfersdorff, 1996] With accurate predictions attained for the single element tests, the model was employed for the FE model of the whole suction caisson. The outcomes were validated by comparison against previous work done with the same soil model for dense IGtH sand. [Thieken, 2014] When compared against the numerical study by Thieken [Thieken, 2014], results attained again gave partial success. The fully drained response was better captured by the current FE model when compared with the results from Houlsby's analytical method. The current model gave a percentage of error of 10%, while Thieken's model gave an error percentage of 13%. For the partially drained and fully undrained analyses, the current FE model consistently overpredicted capacity by a small amount, with the difference increasing with the increase in the loading rate, or as the conditions neared the fully undrained state. Also, the FE model failed to attain the capacities at high displacements due to numerical

convergence issues encountered in ABAQUS. Though, as described in Section 4.4, higher displacements are not allowed for the operation of an OWT, thus from a practical point of view, the inability of the FE model to attain numerical convergence at high displacements could be ignored. However, from a research point of view, a possible aim for future works should be to solve the numerical convergence problem in the finite element model. Artificial modelling means such as the adoption of an elastic toe near the skirt tip of the caisson and/or low stiffness elements in the same region with the correct interaction properties can be undertaken. A deeper understanding of the Hypoplasticity model may also lead to developing an alternate user subroutine in FORTRAN with means to tackle the convergence issues at the higher displacements.

The final series of tests undertaken in this thesis was to study UWA Superfine Silica Sand with the Hypoplastic soil model, and again compare the results with established centrifuge test results and numerical studies employing a complex soil model. The predictions by the Hypoplastic soil model provided better results in the fully drained and the fully undrained analyses, though it underpredicted partially drained capacity before failing to converge at higher displacements, though there is no practical requirement of capacities at high displacement. The transition curve in Fig. 4.43 provides the capacities of the suction caisson relevant in its operational life.

Thus, from the thesis and its summary provided above, the following conclusions can be drawn for UWA Superfine Silica Sand:

- In a normal offshore environmental state, represented by a long-term loading, or fully drained conditions, the Hypoplastic failure model provides the closest

match to the capacity predicted by Houlsby, with an error percentage of only 2.9%, versus 10.3% and 12.9% errors predicted by Mohr Coulomb model and Whyte's bounding surface model, respectively. Thus, for fully drained capacity, the Hypoplastic model is recommended.

- In an extreme storm condition, represented by a short-term loading, or fully undrained condition, both the Hypoplastic model and Whyte's bounding surface model provide accurate matches to centrifuge results, whereas Mohr Coulomb provides drastic overestimations. Due to the relatively simple parameters required by the Hypoplastic model, compared to the complex bounding surface model, the Hypoplastic model is preferred.
- In intermediate offshore environmental conditions, represented by partially drained conditions, the Hypoplastic model provides limited success. It is accurate at low displacements, whereas at higher displacements Whyte's bounding surface model shows better agreement to centrifuge results. Thus, for partially drained ultimate capacity, Whyte's bounding surface model should be recommended at this time.
- For application in the offshore industry, the operational displacement is typically limited to only 0.45% of the skirt length. For low displacements, up to 0.2%, the Hypoplastic model is recommended for all environmental conditions. For the higher operational displacements, from 0.2% to 0.45%, the Hypoplastic model is recommended only for the fully drained and the fully

undrained capacities. For intermediate conditions, Whyte's bounding surface model is recommended.

- For a typical 3MW OWT, 86m high, supported by a tripod suction caisson foundation system, the estimated overturning moment during an extreme storm condition can be taken as 153MN-m. This moment must be resisted by the vertical loads developed in the individual caissons, with the critical design load being the tensile capacity of the caisson in the windward side, as described in Section 4.4.1. The current FE model with the Hypoplastic soil failure model predicts a restoring moment of 222.58 MN-m, and a factor of safety of 1.454. Thus, it successfully provides sufficient resistance to uplift against failure and further reinforces the established capability of suction caissons as a viable foundation option to support offshore wind farms.

REFERENCES

Achmus, M., & Thieken, K. (2014). Numerical Simulation of the Tensile Resistance of Suction Buckets in Sand. Journal of Ocean and Wind Energy, 1(4), 231-239.

ABAQUS. (2013). ABAQUS 6.13 Documentation. Providence, RI, USA: Dassault Systemes.

Ahmed, S. S. (2015). Finite Element Modeling of Suction Caisson and Large Diameter Monopile in Dense Sand Under Oblique and Lateral Load. Master's Thesis, Memorial University of Newfoundland, Faculty of Engineering and Applied Sciences.

Al Hakeem, Nabil M. Ali Hameed (2019). Finite Element Investigation into The Performance Of Embedded Plate Anchors In Sand. Doctoral dissertation, Texas A&M University.

Aubeny, C. (2018). Geomechanics of Marine Anchors. Boca Raton: CRC Press.

Bienen B, Klinkvort RT, O'Loughlin CD, Zhu F, Byrne BW. (2018). Suction caissons in dense sand, part I: installation, limiting capacity and drainage. Géotechnique, 68(11)p937-952.

Bolton, M. D. (1986). The shear strength and dilatancy of sands. Geotechnique, 36(1), 65–78.

Branlard, E. (2008) “Gust Definitions.” Emmanuel.branlard.free.fr. Web.

Breusers, H.N.C. (1974) Suction of sand. Bulletin of the International Association of Engineering Geology 10, 65–66.

Briaud, Jean-Louis. (2013) Geotechnical Engineering: Unsaturated and Saturated Soils.

Byrne, B. W. (2000). Investigations of suction caissons in dense sand. PhD. Dissertation. Oxford, U.K.: University of Oxford.

Carrier WD. (2003) Goodbye, Hazen, Hello, Kozeny-Carman. J Geotech Geoenvironment Engineering;129(11):1054–6.

Cerfontaine B, Collin F, Charlier R. (2015). Numerical modelling of transient cyclic vertical loading of suction caissons in sand. Geotechnique, 65(12):p121 – 136.

Chow SH, Roy A, Herduin M, Heins E, King L, Bienen B, O'Loughlin C, Gaudin C, Cassidy M. (2019) Characterization of UWA superfine silica sand. Oceans Graduate School, UWA.

Cotter, O. (2009). The Installation of Suction Caisson Foundations for Offshore Renewable Energy Structures. PhD Thesis, University of Oxford Magdalen College.

Das, Braja M. (1997) Principles of Geotechnical Engineering. Boston: PWS.

Davis, E.H. and Poulos, H.G. (1968), The use of elastic theory for the settlement prediction under three-dimensional conditions. Geotechnique 1968; 18(1): 67-91.

Fellin, W. and Ostermann, A. (2002), Consistent tangent operators for constitutive rate equations. Int. J. Numer. Anal. Meth. Geomech., 26: 1213-1233.

Felin, W. (2002) Hypoplasticity for beginners. Institute of Geotechnique an Tunnel Construction, University of Innsbruck.

Global Wind report (2018).

Grajales Saavedra, Francisco Javier (2017). Lateral Capacity of Piles and Caissons in Cohesive Soils. Doctoral dissertation, Texas A&M University.

Green R. (2019). Finite element modelling of a suction caisson subject to monotonic tensile loading. Master's thesis, University of Delaware.

Gudehus, G. (1996). A Comprehensive Constitutive Equation For Granular Materials. Soils and Foundations 36 (1), 1-12.

Helwany, Sam. (2007) Applied Soil Mechanics with ABAQUS Applications. John Wiley & Son, Inc., USA.

Herle, Ivo & Gudehus, Gerd. (1999). Determination of Parameters of a Hypoplastic Constitutive Model from Properties of Grain Assemblies. Mechanics of Cohesive-frictional Materials.

Houlsby, G. T., Kelly, R. B., & Byrne, B. W. (2005). The tensile capacity of suction caissons in sand under rapid loading. Proceedings of the international symposium on fronteirs in offshore geotechnics, (pp. 405-410). Perth (WA, Australia).

Khennane, A. (2013). Introduction to Finite Element Analysis Using MATLAB and Abaqus. Boca Raton: CRC Press, https://doi.org/10.1201/b15042

Kolymbas D. (1977) A rate-dependent constitutive equation for soils. Mech Res Com- mun;4(6):367–72

Kolymbas D., Herle I. (1998) Hypoplasticity: A Framework to Model Granular Materials. In: Cambou B. (eds) Behaviour of Granular Materials. International Centre for Mechanical Sciences (Courses and Lectures), vol 385. Springer, Vienna

Kulhawy, F.H., and Mayne, P.W. (1990) Manual on estimating soil properties for foundation design. United States.

Lade, Poul. (2005). Overview of Constitutive Models For Soils. Geotechnical Special Publication. 1-34. 10.1061/40771(169)1.

Lees, Andrew. (2016). Geotechnical Finite Element Analysis.

Malhotra, S. (2011). Selection, Design and Construction of Offshore Wind Turbine Foundations, Wind Turbines, Dr. Ibrahim Al-Bahadly (Ed.), ISBN: 978-953-307-221-0, InTech

Mana DS, Gourvenec S, Randolph MF. (2014) Numerical modelling of seepage beneath skirted foundations subjected to vertical uplift. Computers and Geotechnics, 55:p150-157.

Neto EdS, Perić D, Owen DRJ (2008) Computational methods for plasticity. Wiley, New York.

Nikitas, G., Vimalan, N., & Bhattacharya, S. (2016). An innovative cyclic loading device to study long term performance of offshore wind turbines. Soil Dynamics and Earthquake Engineering 82, 154-160.

Potts, D.M., and Zdravkovic, L. (1999) Finite element analysis in geotechnical engineering: theory. Thomas Telford, London.

Senders, M. (2008). Suction Caissons in Sand as Tripod Foundations for Offshore Wind Turbines. PhD Thesis, The University of Western Australia, School of Civil and Resource Engineering.

Smith IM and Griffiths DV. (1998) Programming the Finite Element Method (3rd. ed.). John Wiley & Sons, Inc., USA

Stutz, Hans & Wuttke, Frank. (2018). Hypoplastic modeling of soil-structure interfaces in offshore applications. Journal of Zhejiang University SCIENCE A. 19. 10.1631/jzus.A1700469.

Terzaghi, K. (1925). Principles of Soil Mechanics. Engineering News-Record, 95(19-27)

Thieken, Klaus & Achmus, Martin & Schröder, Christian. (2014). On the behavior of suction buckets in sand under tensile loads. Computers and Geotechnics. 60. 88–100. 10.1016/j.compgeo.2014.04.004.

tom Wörden F. (2010) Untersuchungen zum räumlichen aktiven Erddruck auf starre vertikale Bauteile im nichtbindigen Boden. Ph.D. Thesis, Leibniz University of Hannover, Germany.

Universal Foundation.

Vaitkunaite, E., Nielsen, B. N., & Ibsen, L. B. (2016). Bucket Foundation Response Under Various Displacement Rates. International Journal of Offshore and Polar Engineering, Vol. 26, No. 2, 116-124.

Van der Tempel, J., & Molenaar, D. (2002). Wind Turbine Structural Dynamics – A Review of the Principles for Modern Power Generation Onshore and Offshore. Wind Engineering 26.

von Wolffersdorff, P.-A. (1996), A hypoplastic relation for granular materials with a predefined limit state surface. Mech. Cohes.-Frict. Mater., 1: 251-271.

Whyte S, Burd HJ, Martin CM, Randolph MF, Bienen B, Rattley M, Roy A, Stapelfeldt M. Comparison of numerical simulations using a bounding surface model to centrifuge tests of axial loaded suction buckets in dense sand. (Un-published)

Wood, D. (2009). Soil Mechanics: A One-Dimensional Introduction. Cambridge: Cambridge University Press. doi:10.1017/CBO9780511815553

Wu, W. and E. Bauer (1994). A simple hypoplastic constitutive model for sand. International Journal for Numerical and Analytical Methods in Geomechanics 18 (12), 833-862.